FEDERAL UNIVERSITY OF ITAJUBÁ – UNIFEI
MECHANICAL ENGINEERING INSTITUTE
POSTGRADUATE PROGRAM IN MECHANICAL ENGINEERING

Eduardo Hoisler Sallet

Numerical-Experimental Correlation of Rifle Firing Loads: Integrating High-Speed DIC with Explicit Dynamics

Itajubá/MG

2026

FEDERAL UNIVERSITY OF ITAJUBÁ – UNIFEI
MECHANICAL ENGINEERING INSTITUTE
POSTGRADUATE PROGRAM IN MECHANICAL ENGINEERING

Eduardo Hoisler Sallet

Numerical-Experimental Correlation of Rifle Firing Loads: Integrating High-Speed DIC with Explicit Dynamics

Dissertation submitted to the Postgraduate Program in Mechanical Engineering, from Mechanical Engineering Institute of the Federal University of Itajubá, as a requirement to obtain the title of Master of Science in Mechanical Engineering.

Concentration area: Design, Materials and Processes.

Supervisor: Prof. Dr. Guilherme Ferreira Gomes

Itajubá/MG
2026

FEDERAL UNIVERSITY OF ITAJUBÁ – UNIFEI
MECHANICAL ENGINEERING INSTITUTE
POSTGRADUATE PROGRAM IN MECHANICAL ENGINEERING

Eduardo Hoisler Sallet

Numerical-Experimental Correlation of Rifle Firing Loads: Integrating High-Speed DIC with Explicit Dynamics

Dissertation approved by the examining board on February 2nd, 2026, awarding the author the title of **Master of Science in Mechanical Engineering.**

Dissertation Committee
Prof. Dr. Guilherme Ferreira Gomes (UNIFEI)
Prof. Dr. Antonio Carlos Ancelotti Júnior (UNIFEI)
Prof. Dr. Andersan dos Santos Paula (IME)

Itajubá
2026

I dedicate this work to Jesus Christ, the expression of the Father's love for humanity, and to my family, Daniele and José, a piece of heaven on Earth.

ACKNOWLEDGEMENTS

To my family, Daniele and José, who stood by my side throughout the entire process of preparing this dissertation, understanding my absences, offering support, and being a constant source of encouragement and joy that motivated me to achieve this milestone.

To my parents, Moacir and Ironda, who have always valued education and encouraged me to follow the paths of knowledge, and to my sister Bruna, my lifelong companion, who has always supported and encouraged my academic journey.

To my advisor, Prof. Dr. Guilherme Ferreira Gomes, for his trust in my work, his availability, his continuous academic support, and his valuable guidance, which made the development of this research possible. I also extend my gratitude to the professors at UNIFEI, from whom I learned profoundly and who contributed decisively to the professional I am today.

I also extend my thanks to all colleagues from GEMEC (Research Group on Numerical Methods and Optimization), with whom I had the opportunity to learn intensively through research activities, technical discussions, and the preparation of scientific articles.

I further thank my colleagues at IMBEL, especially Col. Omar Tumas, head of the Fábrica de Itajubá - FI, for encouraging me to pursue this master's degree, as well as all those who directly contributed to making the practical part of this work possible through modeling, prototyping, and the execution of the necessary experimental tests.

Finally, I thank the Brazilian Army for making this course possible, which significantly contributed to my professional development and to the acquisition of new technical and scientific capabilities applicable to the Fábrica de Itajubá - FI.

"Love has clarified everything,
Love has resolved everything,
Therefore, I glorify Love, wherever it may be.

Saint John Paul II

RESUMO

Este trabalho propõe e implementa um arcabouço metodológico para a caracterização mecânica de um chassi de fuzil de precisão submetido a condições de carregamento altamente transitórias decorrentes do evento de disparo. A abordagem combina medições experimentais em alta velocidade por meio da técnica de Correlação Digital de Imagens (Digital Image Correlation – DIC) com modelagem numérica baseada em Análise por Elementos Finitos (FEA) em regime de dinâmica explícita, visando à obtenção de uma descrição experimental–numérica consistente da resposta estrutural do sistema. Do ponto de vista experimental, a técnica DIC permitiu a aquisição de campos completos de deslocamento e deformação sob condições dinâmicas, fornecendo uma base robusta para a identificação de regiões estruturalmente críticas e para a validação dos modelos numéricos. No âmbito computacional, adotou-se uma formulação explícita de elementos finitos, adequada à representação de fenômenos caracterizados por curtas escalas de tempo, elevadas taxas de deformação e efeitos inerciais relevantes. A estratégia de validação, fundamentada na comparação direta entre campos experimentais obtidos por HS-DIC (Correlação de Imagens Digitais de Alta Velocidade) e resultados numéricos, mostrou-se eficaz na avaliação da adequação das hipóteses de modelagem, das condições de contorno e da descrição dos carregamentos. Adicionalmente, o trabalho discute a importância da modelagem constitutiva de materiais poliméricos sob carregamentos dinâmicos, destacando as limitações de formulações simplificadas e a necessidade de modelos sensíveis à taxa de deformação para a obtenção de previsões fisicamente consistentes. Nesse contexto, é apresentada uma estrutura constitutiva dependente da taxa de deformação, construída a partir de uma formulação fenomenológica orientada à modelagem computacional, com parâmetros extraídos e sistematizados a partir de dados da literatura, visando à representação adequada do comportamento mecânico do material em regimes de alta taxa de deformação.

Palavras-chaves: Correlação Digital de Imagens (DIC); DIC em alta velocidade; Dinâmica explícita; Análise por Elementos Finitos; Modelagem constitutiva; Taxa de deformação; Materiais poliméricos; Chassi de fuzil de precisão.

ABSTRACT

This work proposes and implements a methodological framework for the mechanical characterization of a precision rifle chassis subjected to highly transient loading conditions induced by the firing event. The proposed approach combines high-speed experimental measurements using the Digital Image Correlation (DIC) technique with numerical modeling based on Finite Element Analysis (FEA) in an explicit dynamics framework, aiming at obtaining a consistent experimental–numerical description of the structural response of the system. From an experimental standpoint, the DIC technique enabled the acquisition of full-field displacement and strain measurements under dynamic conditions, providing a robust basis for the identification of structurally critical regions and for the validation of the numerical models. From a computational perspective, an explicit finite element formulation was adopted, which is well suited for representing phenomena characterized by short time scales, high strain rates, and significant inertial effects. The validation strategy, based on the direct comparison between experimental fields obtained via High-speed DIC (HS-DIC) and numerical results, proved to be effective in assessing the adequacy of the modeling assumptions, boundary conditions, and load descriptions. Additionally, this work discusses the importance of constitutive modeling of polymeric materials under dynamic loading, highlighting the limitations of simplified formulations and the need for strain-rate-sensitive models in order to obtain physically consistent predictions. In this context, a strain-rate-dependent constitutive framework is presented, built upon a phenomenological formulation oriented toward computational modeling, with parameters extracted and systematized from data available in the literature, aiming at an adequate representation of the mechanical behavior of the material under high strain-rate regimes.

Key-words: Digital Image Correlation (DIC); High-speed DIC; Explicit dynamics; Finite Element Analysis; Constitutive modeling; Strain-rate effects; Polymeric materials; Precision rifle chassis.

LIST OF FIGURES

LIST OF TABLES

ABBREVIATIONS AND ACRONYMS

DIC	Digital Image Correlation
FEA	Finite Element Analysis
HS	High-Speed
UHS	Ultra High-Speed
FPS	Frames per second
ZC	Zero-mean Cross-Correlation
$ZNCC$	Zero-mean Normalized Cross-Correlation
$ZNSSD$	Zero-mean Normalized Sum of Squared Differences
ε	Strain (dimensionless)
$\dot{\varepsilon}$	Strain rate (s^{-1})
u	Displacement in the x direction (mm)
v	Displacement in the y direction (mm)
u_{max}	Maximum displacement (mm)
θ	Angle of deformation (degrees)
σ	Stress (MPa)
τ	Shear stress (MPa)
σ_{xy}	Shear stress in the x-y plane (MPa)
σ_{eq}	Equivalent (von Mises) stress (MPa)
σ_y	Yield stress (MPa)
σ_{y0}	Quasi-static reference yield stress (MPa)
$\varepsilon_{xx}, \varepsilon_{yy}$	Normal strains in x and y directions
ε_{xy}	Shear strain in the x-y plane (dimensionless)
ε_{11}	Longitudinal strain (dimensionless)
ε_{22}	Transverse strain (dimensionless)
E	Young's modulus (MPa)
ν	Poisson's ratio (dimensionless)
ρ	Density (g/cm^3)
ROI	Region of Interest
S	Subset (region of analysis)
Δx	Displacement in the x direction within subsets (mm)
Δy	Displacement in the y direction within subsets (mm)
F_x	Force in the x direction (N)
F_y	Force in the y direction (N)
F_{peak}	Peak force (N)

F_{mean}	Mean force (N)
F_{max}	Maximum force (N)
V_i	Volume of the specimen (cm^3)
$\mathbf{A}, \mathbf{B}$	Time evolution matrices (Explicit integration)
$\mathbf{C}$	Damping matrix
$\mathbf{K}$	Stiffness matrix
$\mathbf{M}$	Mass matrix
$\mathbf{R}$	Vector of nonlinear effects
$\mathbf{f}_{\text{ext}}$	External force vector
f_i	Body forces per unit mass
t_i	Surface traction vector
t	Time
x_i	Current spatial coordinates
X_α	Material coordinates
n_j	Unit normal vector
δx_i	Virtual displacement field
$\mathbf{u}$	Nodal displacement vector
$\dot{\mathbf{u}}$	Nodal velocity vector
$\ddot{\mathbf{u}}$	Nodal acceleration vector
Ω	Current domain volume
σ_{ij}	Cauchy stress tensor
A, B, n, m	Johnson–Cook constitutive parameters
C_{CS}	Cowper–Symonds strain-rate parameter
P_{CS}	Cowper–Symonds exponent parameter
T	Current temperature
T_m	Melting temperature
T_{ref}	Reference temperature
$\dot{\varepsilon}_0$	Reference strain rate
ε_{eng}	Engineering strain
ε_{true}	True strain
ε_p	Equivalent plastic strain
σ_{eng}	Engineering stress
σ_{true}	True stress

CONTENTS

1 INTRODUCTION

High-precision firearms, in their operational context, are employed in tactical situations in which the shooter is positioned at a relatively large distance from the target, requiring the ability to occupy a concealed position, prepare the weapon, perform ballistic calculations, execute the necessary shots, and withdraw safely [1]. In the sporting context, precision shooting aims to hit small targets placed at long distances, highlighting the shooter's skill as well as the quality of the ammunition and the firearm system employed.

In Brazil, high-precision firearms are predominantly used by special operations units and by a restricted group of competitors dedicated to precision shooting sports. Civilian access to firearm acquisition is regulated by a restrictive and frequently changing legal framework, which tends to discourage the practice of this sporting modality [2]. In contrast, in the North American market, in addition to its operational use, civilian access to firearm ownership is a constitutional right [3], which results in a strongly consolidated culture surrounding shooting sports, of which precision shooting is one of its most technical and specialized branches. According to the Small Arms Survey, the United States represented approximately 4% of the world's population, but held about 46% of the estimated 857 million civilian-owned firearms by the end of 2017 [4].

This extensive consumer market is one of the main drivers behind the existence of a highly developed industrial ecosystem, composed of companies offering products aimed at shooting sports and, in particular, at precision shooting. This segment is characterized by high added value and intense competitiveness, in which technological differentiation and continuous innovation are essential factors for maintaining market share.

In this context, starting in the 1970s, with the popularization of composite materials, companies such as McMillan®began to develop rifle stocks for precision firearms using fiberglass or carbon fiber reinforced epoxy matrices [5], replacing the traditional wooden structures. In addition to mass reduction and increased specific stiffness, these new solutions enabled the introduction of ergonomic adjustment mechanisms, such as adjustable butt pads and cheek rests, allowing for more stable shooting positions adaptable to shooters of different statures, as illustrated in Figure 1.1.

Figure 1.1 – Precision rifle mounted on a composite chassis manufactured by McMillan®.

The national defense industry, represented by Indústrioa de Material Bélico do Brasil (IMBEL), includes in its product portfolio the AGLC high-precision rifle (Figure 1.2), widely employed by Military Police units and the Armed Forces. Although this system is recognized for its accuracy, its chassis is still manufactured from wood and does not feature ergonomic adjustments. This limitation compromises operational performance by failing to adequately accommodate shooters with anthropometric characteristics different from those considered in the original design.

Figure 1.2 – AGLC precision rifle mounted on a wooden chassis.

Therefore, with the aim of modernizing defense equipment produced domestically, a strategic need arises to master the development and manufacturing of composite material chassis. Such expertise would reduce dependence on imports and enable the adaptation of solutions to the specific operational requirements of the armed and auxiliary forces.

However, the first step in the design of a composite chassis consists of the proper characterization of the mechanical loads to which the structure is subjected during firing. This is the central objective of the present work: to perform the numerical modeling of the

loading experienced by the chassis of a 7.62 mm sniper-type firearm, in order to quantify the associated mechanical demands. This modeling will be validated through experimental results obtained using the *Digital Image Correlation* (DIC) technique.

This full-field, non-contact technique offers significant advantages over conventional measurement methods, as the instrumentation does not physically interact with the specimen, thereby avoiding measurement interference, mass-loading effects, and stress perturbations. Furthermore, it allows relatively simple implementation and flexible experimental configuration.

This study thus presents a clear industrial motivation, by systematizing information relevant to the development of composite rifle stocks. Nevertheless, achieving this objective requires extensive academic development, particularly with regard to experimental characterization, numerical modeling, and constitutive material description.

In this sense, the first conceptual axis of this work consists of understanding the Digital Image Correlation technique, initially in its classical formulation and subsequently in its extensions to high- and ultra-high-speed regimes, as well as its integration with numerical tools. In the chapter entitled *Fundamentals of High-Speed Digital Image Correlation and Finite Element Integration*, a critical review of the DIC technique is presented, with emphasis on its applications to highly transient phenomena, discussing its theoretical foundations, experimental limitations, and challenges associated with data acquisition and processing at high strain rates. This background provides the necessary support for the subsequent description of the mechanical behavior of the chassis under dynamic loading.

Once this experimental and conceptual basis is established, the second axis of the work consists of enhancing the predictive capability of the numerical framework through the selection and calibration of an appropriate constitutive model. Polymeric and composite materials exhibit strong strain-rate dependency. Therefore, in the chapter *Rate-Dependent Constitutive Framework for Polymers*, a strain-rate-sensitive formulation suitable for explicit dynamic analyses is presented, enabling a refined description of the mechanical behavior of the chassis under high-rate loading conditions.

Finally, the third axis of the work consists of constructing and validating a numerical model capable of representing the structural response of the system under dynamic conditions. The firing event involves high strain rates, short time scales, and significant inertial effects, making the explicit dynamics formulation particularly suitable. In the chapter *Explicit Finite Element Modeling and DIC-Based Validation*, a validation methodology is proposed based on the direct comparison between strain fields obtained by HS-DIC and results from explicit finite element simulations. This approach enables the assessment of initial and boundary conditions, as well as the applied loads, ensuring that the model realistically represents the structural response of the chassis during firing

The experimental characterization using Digital Image Correlation (DIC) for the

validation of explicit numerical Finite Element Analysis (FEA), combined with the refinement of the constitutive model, establishes a robust methodological framework for the structural design of composite chassis. From this approach, it becomes possible to identify structurally critical regions, guide the rational distribution of reinforcements, and define mass reliefs where appropriate, resulting in lighter, more ergonomic, and mechanically efficient structures. Thus, the present work not only contributes to the advancement of academic knowledge in experimental and computational mechanics but also provides direct support for the technological and industrial development of high-precision firearm systems.

2 RESEARCH OBJECTIVES

The main objective of this work is to contribute to the development of a composite rifle stock by describing the mechanical loads induced by the firing of a 7.62 mm ammunition in a precision rifle, through a numerically based approach validated by experimental measurements using Digital Image Correlation (DIC).

The specific objectives of this research are:

- To review the state of the art on Digital Image Correlation (DIC), with emphasis on its high-speed (HS-DIC) and ultra-high-speed (UHS-DIC) implementations, as well as its integration with finite element analysis for experimental-numerical validation.
- To develop a numerical model capable of describing the mechanical loads induced by the firing of a 7.62 mm ammunition and the corresponding load transfer to the chassis.
- To perform an experimental characterization of the strain and displacement fields developed in the rifle chassis during firing using the DIC technique.
- To establish and apply a validation methodology based on the direct comparison between experimental DIC measurements and results obtained from explicit finite element simulations.
- To refine the numerical model by incorporating a strain-rate-sensitive constitutive formulation appropriate for materials, improving the predictive capability of the simulations under dynamic loading conditions.

3 FUNDAMENTALS OF HIGH-SPEED DIGITAL IMAGE CORRELATION AND FINITE ELEMENT INTEGRATION

3.1 Chapter Introduction

Digital Image Correlation (DIC) is a widely applied technique in experimental mechanics that enables full-field measurement of displacements and strains in specimens under loading. The method relies on comparing digital images of an object before and after deformation using a computationally implemented algorithm [6, 7]. DIC is a non-contact and non-destructive method that allows precise measurements without compromising the integrity of the tested specimen and is straightforward to implement in practice. Owing to this flexibility, it has been extensively applied in a wide range of loading scenarios, involving specimens of different materials and scales, and can be employed both in laboratory environments and under extreme conditions [6, 8].

The application of DIC has been transformative, particularly in fields where traditional measurement techniques, such as strain gauges, face significant limitations. Strain gauges, while useful, offer only localized measurements, which can miss critical information regarding the overall behavior of the specimen. In contrast, DIC provides a comprehensive, full-field assessment, offering detailed displacement and strain maps across the entire surface of the specimen. This feature allows for a deeper understanding of complex phenomena such as localized plasticity, crack initiation, and material failure under various loading conditions. Furthermore, DIC's ability to work under both quasi-static and dynamic loading scenarios has made it a critical tool in fields ranging from aerospace and automotive engineering to materials science and biomechanics.

While DIC is well established for quasi-static and low strain-rate measurements, its application in high-speed and ultra high-speed regimes introduces specific challenges. The demand for extremely high image acquisition rates, intense illumination, and precise synchronization between cameras and the physical event imposes both instrumental and computational constraints. The need for high-speed cameras capable of capturing thousands, or even millions, of frames per second, combined with advanced image processing algorithms, has expanded the boundaries of what can be measured in real-time. Nevertheless, combining DIC with high-speed and ultra high-speed cameras enables the acquisition of full-field displacement and strain maps under extreme loading conditions, supporting the investigation of impact and energy absorption phenomena [8, 9].

Recent advancements in DIC technology have addressed some of these challenges,

enabling the technique to be applied successfully in high-speed regimes that were previously inaccessible. For example, ultra high-speed DIC systems now allow researchers to capture deformation and strain during impact events, such as those occurring in crash testing or material fracture experiments, at a level of detail that traditional methods cannot achieve. This capability has led to more accurate assessments of material behavior under dynamic loading, improving our understanding of complex phenomena such as fracture mechanics, energy dissipation, and structural integrity under impact loading.

Unlike traditional strain gauges, which provide only localized measurements, DIC offers a global assessment of the specimen. This comprehensive measurement enables validation and refinement of numerical models, such as Finite Element Analysis (FEA), by allowing comparison of experimental results with simulation outputs, verification and adjustment of boundary conditions, refinement of material models, and enhancement of predictive capabilities in dynamic testing scenarios [10, 11, 12, 13].

This chapter aims to assist researchers in solid mechanics who investigate complex loading conditions and high strain-rate regimes. The DIC technique is presented with emphasis on high-speed and ultra high-speed implementations as a means to obtain displacement and strain fields under dynamic loading. This approach enables a more rigorous understanding of structural response and supports the validation and improvement of numerical models to accurately represent the observed mechanical behavior. By highlighting the integration of DIC with high-speed imaging technology, this review provides a unique perspective on the frontier of experimental mechanics.

Notably, this work introduces novel contributions to the application of DIC in dynamic testing, particularly in the context of extreme loading conditions, offering new insights into the evaluation and optimization of numerical models. Building upon these aspects, representative applications of DIC in experimental mechanics are discussed, providing references across various domains where the technique has proven relevant. Finally, the review outlines recent developments and research trends in DIC, defining the current frontiers of knowledge and identifying opportunities for future studies in experimental mechanics.

3.2 Digital Image Correlation (DIC)

3.2.1 Fundamentals of Digital Image Correlation (DIC)

Digital Image Correlation (DIC) is a non-contact optical technique that compares digital images of a specimen before and after loading, using a computational algorithm to measure the full-field displacement and strain across the specimen surface [14, 15, 16, 17].

Initially, a black-and-white speckle pattern is applied to the surface to be analyzed.

This pattern creates a random distribution of light and dark regions, acting as a carrier of information, since each pixel can be converted into a grayscale value (0–255), enabling computational processing. Due to the random nature of the speckle pattern, the neighborhood of each pixel has a unique configuration of grayscale levels, allowing the pre-deformation surface image to be subdivided into small, unique regions called subsets, each associated with a specific location. These subsets are then "tracked" by the DIC algorithm in the post-deformation image, assuming displacement continuity, determining the displacement of the subset, as can be seen in Figure 3.2 [6, 7, 17, 18].

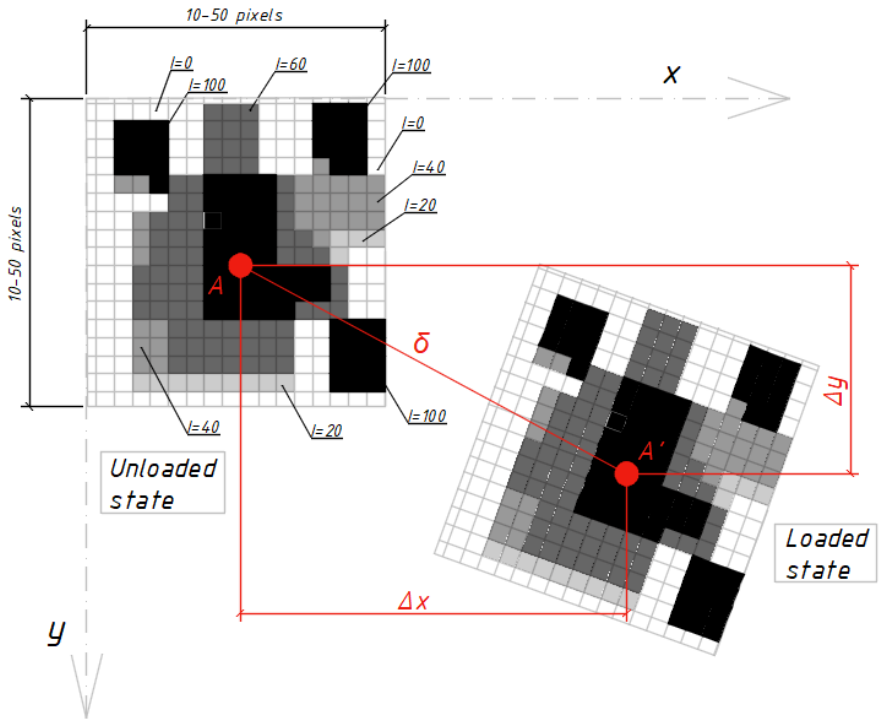

Figure 3.1 – Location of a typical subset, with its random speckle pattern ensuring uniqueness in the grayscale distribution, before and after loading [18].

Similarity between subsets is evaluated using correlation criteria, such as ZNCC (Zero-mean Normalized Cross Correlation) and ZNSSD (Zero-mean Normalized Sum of Squared Differences). Thus, the displacement is obtained from the positional difference of each subset before and after deformation, which in turn allows computation of the strain field [14, 15, 17, 19].

Up to this point, only the discrete grayscale data provided by the image pixels are considered. However, evaluating displacements and strains often requires accuracy beyond the pixel resolution, making subpixel analysis necessary. Interpolation functions are employed to ensure a continuous representation of the intensity field and to allow estimates at intermediate positions [14, 15, 19].

3.2.2 DIC Classifications

A research group at the University of South Carolina first proposed the DIC technique in the early 1980s, a period when digital image processing and numerical computing were still in their early stages of development . Since then, the technique has evolved continuously, driven by technological advances in hardware, improvements in computational algorithms, and the expansion of its applications. In this context, different DIC modalities have been developed, the main ones of which will be discussed below [15].

3.2.2.1 2D Digital Image Correlation (2D DIC)

2D DIC, also known as Bidimensional DIC, is designed for detecting deformations on two-dimensional surfaces. For this reason, when the fundamentals of the technique are presented, the description generally refers to 2D DIC, since it was the first to be proposed and is conceptually more straightforward.

Its setup is relatively simple, consisting mainly of a camera with proper lighting, positioned with its optical axis perpendicular to the analyzed surface, which must be properly prepared with a speckle pattern, as illustrated in Figure 3.2. The 2D DIC technique exhibits remarkable versatility, being applicable across a wide range of scales: from the microscale, using magnification systems coupled to the camera as in conventional optical microscopy, to advanced modalities such as Atomic Force Microscopy (AFM) and Scanning Electron Microscopy (SEM). It can also be employed at the macroscale, enabling the analysis of large structures in civil engineering, up to the field-of-view limit of the DIC system [9, 17].

The main limitation of this method lies in its inability to capture deformations out-of-plane, in addition to the requirement that the analyzed region must be essentially flat. Nevertheless, due to its low cost and ease of implementation, it remains the most widespread variation of the DIC technique. Several authors have proposed solutions to minimize and compensate for the errors arising from these limitations, as well as to enhance measurement accuracy, thereby expanding its scope of application [20].

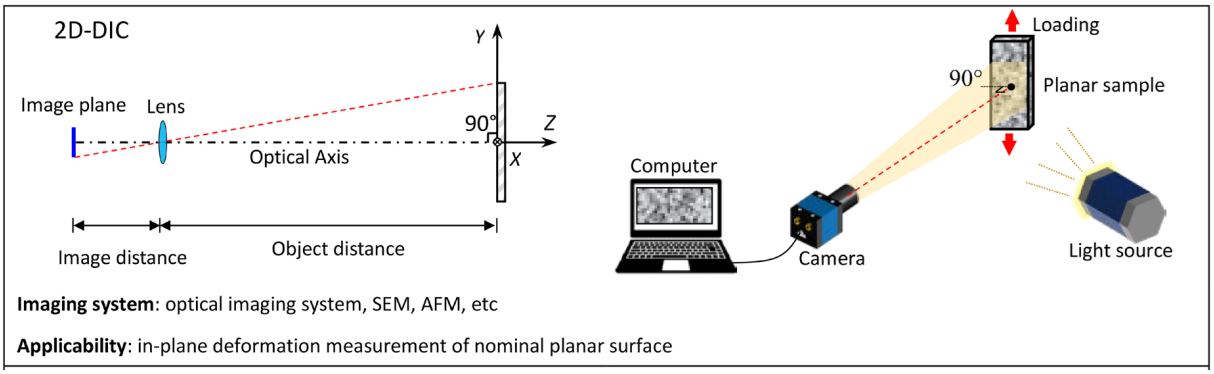

Figure 3.2 – Setup and hardware employed in 2D DIC, presenting different imaging system options and their applicability, inherently limited by the design of the technique (adapted from [6]).

3.2.2.2 3D Digital Image Correlation (Stereo DIC)

To overcome the intrinsic limitations of 2D DIC, Stereo DIC (3D DIC) was developed, based on the principle of binocular stereoscopic vision. The technique employs a light source and two cameras positioned obliquely relative to the analyzed surface, as shown in Figure 3.3.

This configuration allows depth reconstruction, enabling the detection of displacements and deformations on curved surfaces, as well as out-of-plane displacements. Consequently, imaging techniques based on binocular stereoscopic vision, such as light microscope stereo vision, can be employed to determine displacement and strain fields at the microscale [21].

Additionally, Stereo DIC can be implemented with a single camera, provided that its setup includes distinct optical paths, achieved via beam-splitting elements, allowing simultaneous capture of two views of the specimen surface projected onto the left and right halves of the camera sensor [6].

However, the Stereo DIC technique requires a calibration step to determine the cameras intrinsic and extrinsic parameters, which must be strictly synchronized to capture images simultaneously; otherwise, significant errors may occur, especially in high-speed measurements. Moreover, using two cameras positioned at an angle imposes spatial constraints in setups requiring high magnification, and the system cost is considerably higher than that of 2D DIC, particularly in high acquisition rate applications [6, 20].

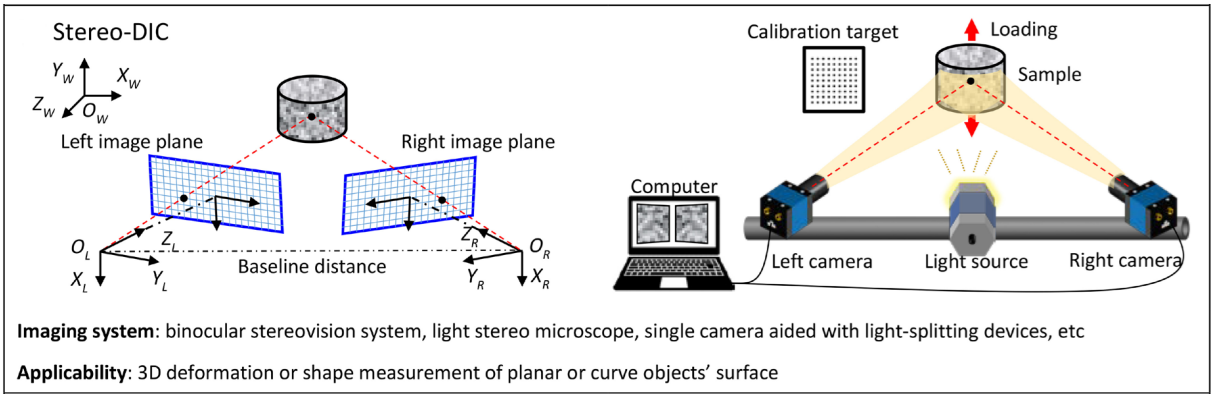

Figure 3.3 – Setup and hardware employed in Stereo DIC (3D DIC), highlighting the need for calibration and oblique camera positioning, as well as its applicability to curved surfaces (adapted from [6]).

3.2.2.3 Digital Volume Correlation (DVC)

Digital Volume Correlation (DVC) differs from Stereo DIC (3D DIC) in that it aims to determine deformations occurring within the bulk of the material. Since it now involves a volume, the methodology uses the material's internal heterogeneities as a natural reference pattern, rather than applying a surface speckle pattern.

For this purpose, techniques such as X-ray tomography are used, scanning the object before deformation to generate two-dimensional slices. Each point in the slice is assigned an intensity reflecting its local heterogeneity. These slices are then reconstructed to form a three-dimensional model of the object, as shown in Figure 3.4 [6, 22, 23].

Analogous to the subsets in 2D DIC, small volumes with unique features are defined in the pre-deformation state. The same process is performed in the deformed state, after which an algorithm correlates the two volumes, allowing the determination of internal displacements and strains [6, 22].

Many materials, such as certain composites, foams, and biological tissues, naturally exhibit internal heterogeneity. This variability often complicates the modeling and prediction of their mechanical behavior. However, the same internal heterogeneity that makes mechanical behavior less predictable also enables the use of Digital Volume Correlation (DVC). These natural variations serve as an intrinsic speckle pattern, providing the necessary reference features for volumetric mapping and serving as input data for the correlation process [23].

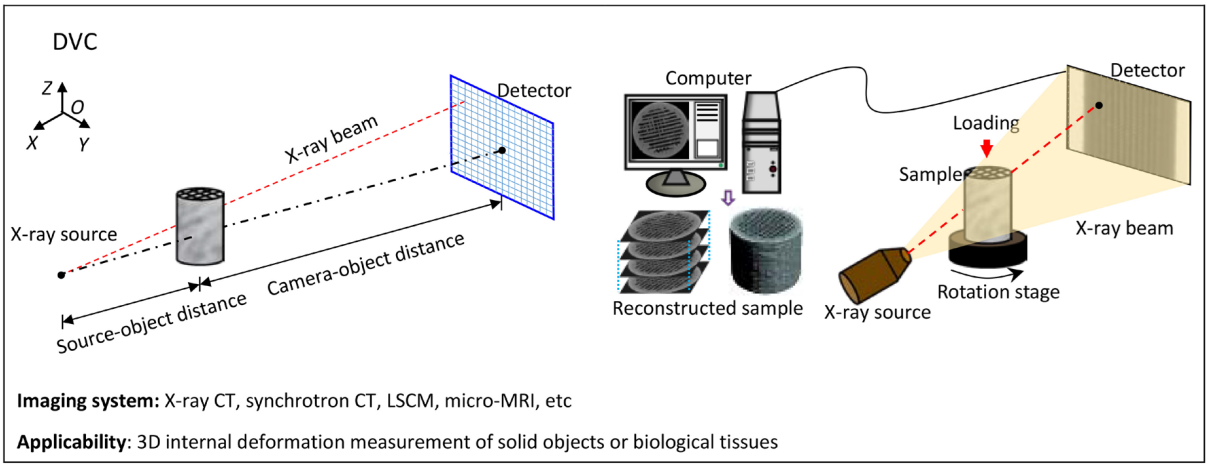

Figure 3.4 – The imaging systems used enable the mapping of the material's internal heterogeneities, which are methodologically exploited as a reference for DVC, defining its applicability (adapted from [6]).

3.2.2.4 Methodological Classifications

Regarding the correlation methodology, the fundamental goal is to identify corresponding regions between a reference image and its deformed image in order to determine the displacement field. Traditionally, this search is performed using the local subset method, in which the image is divided into small windows (subsets) whose deformations are approximated by shape functions, as detailed in the section 3.2.4 *DIC: Experimental Setup and Correlation Methodology.* Each subset is treated independently, without enforcing continuity between adjacent regions, which provides the method with high flexibility, low memory consumption, and good adaptability to complex deformation fields [24]

However, considering that the deformation field is physically continuous, formulations have been developed that enforce continuity between subsets across the region of interest, giving rise to the so-called global DIC. In this approach, the displacement field is described over a continuous domain (see Figure 3.5), which ensures compatibility between regions and results in smoother and more robust strain fields against noise. In contrast, this global coherence involves higher computational cost and increased implementation complexity [6, 24].

Global DIC exhibits greater conceptual consistency with finite element analysis (FEA) formulations. When measurements are performed using a mesh compatible with the FEA model, it becomes possible to directly link the experimental and numerical domains, allowing the comparison of measured and simulated displacements over the same discretization basis. This approach minimizes discretization error and enables a more consistent evaluation of displacement fields [6, 25].

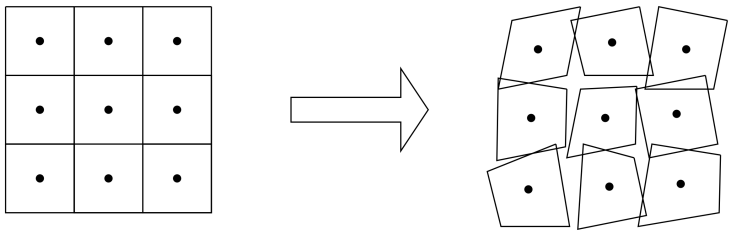

(a) Local DIC

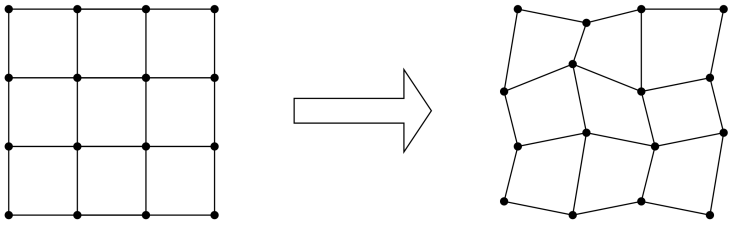

(b) Global DIC

Figure 3.5 – In Local DIC (a), each original subset is tracked independently in the post-deformation image, following a shape function. In Global DIC (b), the deformed subsets share common boundaries, maintaining continuity of the displacement field across the domain [24].

3.2.2.5 Integration with Finite Element Analysis

The integration of DIC and FEA can be realized in a more intrinsic manner than a simple comparison between experimental and numerical results. Various approaches exist for combining DIC and FEA; in this section, we focus on methods such as Finite Element Model Updating (FEMU) and Integrated Digital Image Correlation (IDIC), which represent different levels of fusion between the two techniques.

In FEMU, the displacement or strain fields obtained from DIC are used to iteratively update the numerical model, adjusting material parameters or boundary conditions until the simulated results reproduce the experimental data. Extending this integration, IDIC achieves a deeper coupling between correlation and finite element analysis, where both are solved simultaneously. In this framework, the experimental images themselves serve as input data, and the numerical model directly provides mechanically admissible displacement fields during the correlation procedure [26].

3.2.3 Advantages and Limitations

One of the main advantages of the DIC technique is its non-contact nature, allowing remote displacement measurements. Since it does not require the attachment of sensors or other physical devices to the specimen, the method provides high flexibility for analyzing complex phenomena, including cases with high strain rates such as explosions and impacts, or severe conditions like elevated temperatures, covering a wide range of scales from large structures to the micrometric level [9]. Moreover, DIC provides full-field measurements, enabling the characterization of material and structural behavior in scenarios where de-

formation is non-uniform, ensuring a comprehensive view of the mechanical response of the speciment.

The technique exhibits high versatility, as it requires only conventional illumination conditions, such as artificial white light or natural lighting, and minimal surface preparation of the specimen. In its most basic configuration, 2D DIC requires only a single camera equipped with a CCD sensor, ensuring a low-cost and relatively simple data acquisition setup [7]. The availability of open-source software for image processing and correlation has promoted widespread adoption and consolidation of the technique within the scientific community.

DIC exhibits a wide range of applicability, encompassing both large deformations, such as those observed in crashworthiness studies, and small deformations under service conditions. It is characterized by its robustness under severe deformation conditions and its ability to achieve high measurement precision at the subpixel level through advanced interpolation algorithms applied to the recorded pixel intensities [6, 7, 9, 27].

The technique is applicable into broader engineering frameworks, interacting with other methodologies to complement or enhance their performance. For instance, in structural health monitoring systems applied to bridges, buildings, aircraft, and other large-scale structures, DIC enables continuous tracking of displacements and strains, supporting the assessment of structural integrity and operational safety [6].

On the other hand, the DIC technique exhibits measurement errors associated with intrinsic factors of the technique, related to the correlation algorithm and image acquisition, as well as extrinsic factors, linked to the specific type of application, which can present challenges and require adaptations of the technique to ensure accurate results.

Regarding intrinsic factors, errors related to the correlation algorithm may originate from the shape function, correlation criterion, interpolation scheme, and subset size. The shape function determines how displacements within the subset are modeled, and inappropriate choices may induce systematic errors, particularly in regions with nonlinear deformations. The correlation criterion affects image matching, while the interpolation scheme influences subpixel measurement resolution. The subset size must balance noise sensitivity and the ability to capture local details, as overly small subsets increase noise susceptibility, and overly large subsets may smooth out critical deformations [7, 17].

In the image acquisition process, even under laboratory conditions, errors may arise due to speckle pattern quality, lens distortions, environmental noise, out-of-plane motions, and calibration imperfections. Speckle pattern quality is critical for the technique's fidelity, as poorly defined patterns compromise image matching.

Beyond intrinsic limitations, there are application-dependent challenges. Due to the wide range of DIC applications, errors may manifest differently, requiring adjustments to the image acquisition process or even the algorithm to better suit the specific application. In extreme scenarios, such as high temperatures, underwater environments, high-speed

measurements, or microscopic scales, external factors require continuous refinement of the technique to achieve accurate results [9].

Figure 3.6 illustrates the challenges that must be addressed for different applications of the technique. In high-temperature environments, thermal radiation, heat, and speckle pattern degradation can cause image distortions and noise, even leading to decorrelation. In underwater contexts, light refraction at water-window and window-air interfaces introduces additional distortions. For high-speed measurements, the synchronization and calibration of complex cameras, coupled with persistent background noise during vibrations, can reduce accuracy. At micro- and macro-scales, captured images present more complex structures, requiring specific considerations during analysis [9].

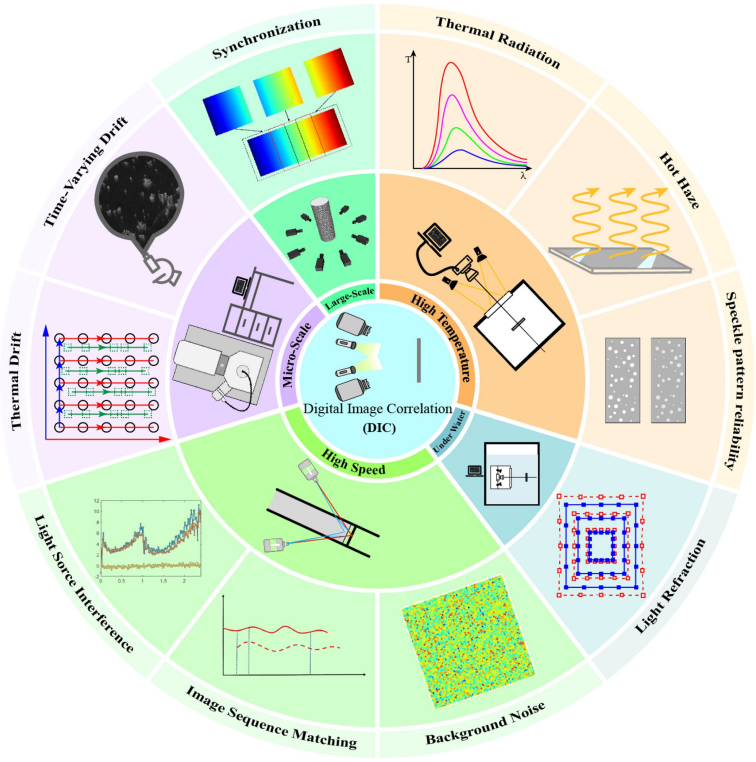

Figure 3.6 – The inner circle illustrates the different applications of the technique, while the outer circle highlights the extrinsic challenges associated with each application [9].

3.2.4 DIC: Experimental Setup and Correlation Methodology

There are several approaches for implementing digital image correlation, a field that is continuously evolving. For didactic purposes, this section provides a concise description of the Local DIC methodology, without delving into variations of the technique or the specific parameters used. The aim is to present the technique in a simple manner, following a basic workflow for conceptual understanding.

The NSSD algorithm (Normalized Sum of Squared Differences) will be employed, optimized using the Newton-Raphson method with partial differential corrections [14].

As mentioned previously, the treatment of input parameters will not be addressed in this section; however, it is worth noting that the selection of subset size, interpolation type, speckle pattern, convergence criterion, and other image parameters directly affects the accuracy of the results.

3.2.4.1 Surface Preparation

The specimen to be subjected to loading must have its surface prepared with a random black-and-white speckle pattern, as shown in Figure 3.7.

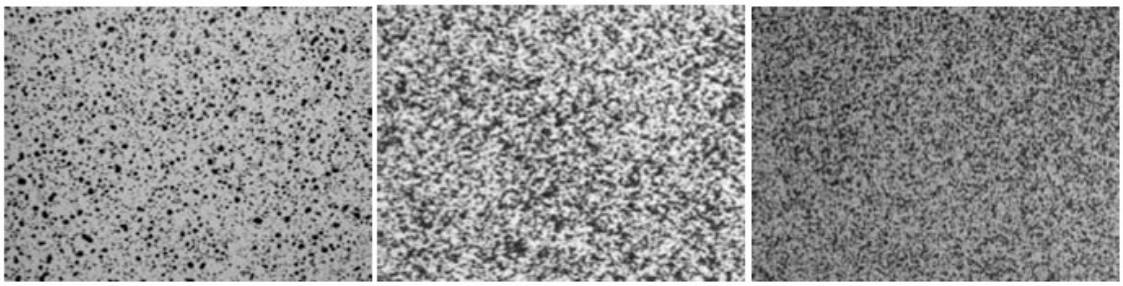

Figure 3.7 – Examples of speckle pattern [28].

Thus, after digital processing, the images before and after loading can be represented as pixel matrices, where each pixel value corresponds to a grayscale level ranging from 0 (black) to 255 (white). Figures 3.8a and 3.8b illustrate how the digital images before and after deformation are converted into discrete data. In the example below, the theoretical deformation resulted in the displacement of one pixel of the central black stripe to the right.

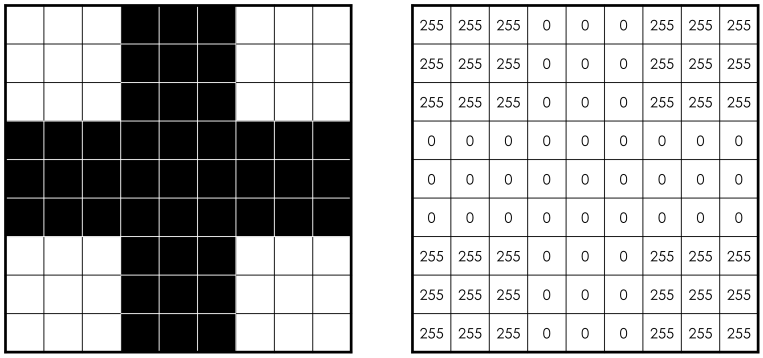

255	255	255	0	0	0	255	255	255
255	255	255	0	0	0	255	255	255
255	255	255	0	0	0	255	255	255
0	0	0	0	0	0	0	0	0
0	0	0	0	0	0	0	0	0
0	0	0	0	0	0	0	0	0
255	255	255	0	0	0	255	255	255
255	255	255	0	0	0	255	255	255
255	255	255	0	0	0	255	255	255

(a)

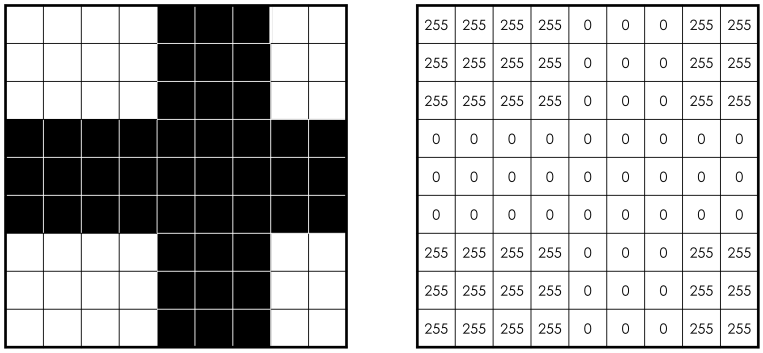

255	255	255	255	0	0	0	255	255
255	255	255	255	0	0	0	255	255
255	255	255	255	0	0	0	255	255
0	0	0	0	0	0	0	0	0
0	0	0	0	0	0	0	0	0
0	0	0	0	0	0	0	0	0
255	255	255	255	0	0	0	255	255
255	255	255	255	0	0	0	255	255
255	255	255	255	0	0	0	255	255

(b)

Figure 3.8 – Image before displacement and its conversion into discrete data, based on the grey level of the pixels composing the image (a) and after the displacement of one pixel of the central black stripe to the right and its conversion into discrete data (b).

3.2.4.2 Region of Interest (ROI) Selection and Subset Definition

In the image of the specimen before loading, it is necessary to define the surface to be analyzed, i.e., the Region of Interest (ROI) within the rest of the image. This procedure is performed manually by the user in the DIC software. For example, in a tensile test of a specimen whose surface has been prepared with a speckle pattern, the user selects the specimen surface in the image and separates it from the rest (grips of the testing machine, image background, etc.).

The ROI is then subdivided into square subsets. These subsets will be located in the post-loading image during processing, and once matched, will allow the calculation of displacements and strains experienced, as illustrated in Figure 3.9.

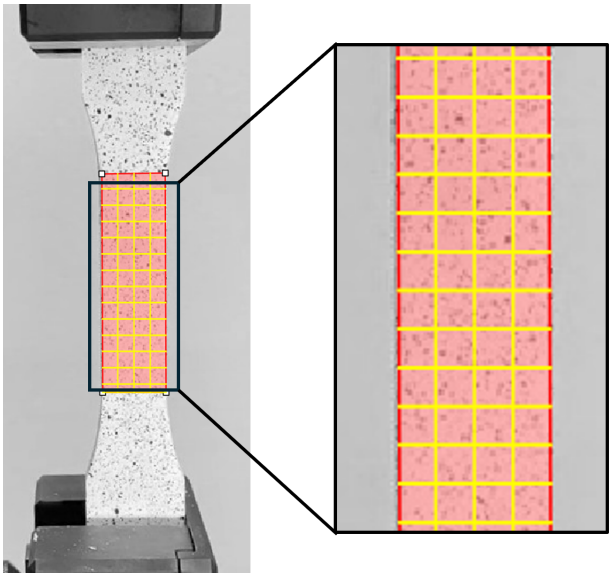

Figure 3.9 – Region of Interest (ROI), prepared with a speckle pattern and overlaid with the indicated positions of the subsets.

3.2.4.3 Processing

Methodology

Since images can be represented as pixel matrices, with each pixel assigned a value between 0 and 255, the pixel intensity and its location in the matrix are related through a function.

In the reference (undeformed) image, let this discrete function be given by Equation 3.1.

$$f(x, y) \tag{3.1}$$

In the image after deformation, it is given by Equation 3.2.

$$g(x', y') \tag{3.2}$$

In general, each position in the image after deformation (x', y') is associated with a corresponding position in the original image (x, y). This displacement can be estimated through a Taylor series expansion around the original position, as presented in Equations 3.3 and 3.4, with respect to the x and y directions, respectively.

$$x' = x + u + \frac{\partial u}{\partial x}\Delta x + \frac{\partial u}{\partial y}\Delta y \tag{3.3}$$

$$y' = y + v + \frac{\partial v}{\partial x}\Delta x + \frac{\partial v}{\partial y}\Delta y \tag{3.4}$$

- u is the displacement in the x direction,
- v is the displacement in the y direction,

- $\frac{\partial u}{\partial x}, \frac{\partial u}{\partial y}, \frac{\partial v}{\partial x}, \frac{\partial v}{\partial y}$ are the partial derivatives of the displacements,
- Δx and Δy represent the displacements within each subset relative to its center.

The DIC technique builds on this concept and applies it to subsets. Each subset of the image before deformation has dimensions $(2M + 1) \times (2M + 1)$ pixels and a center denoted as C. Through the correlation process between the images, the values of u, v, $\frac{\partial u}{\partial x}$, $\frac{\partial u}{\partial y}$, $\frac{\partial v}{\partial x}$, and $\frac{\partial v}{\partial y}$ are obtained, which best describe the new position of the subset in the deformed image, as illustrated in Figure 3.10. Obtaining these six variables allows for the calculation of translation, rotation, shear, normal strains, and their combinations to which the subset has been subjected.

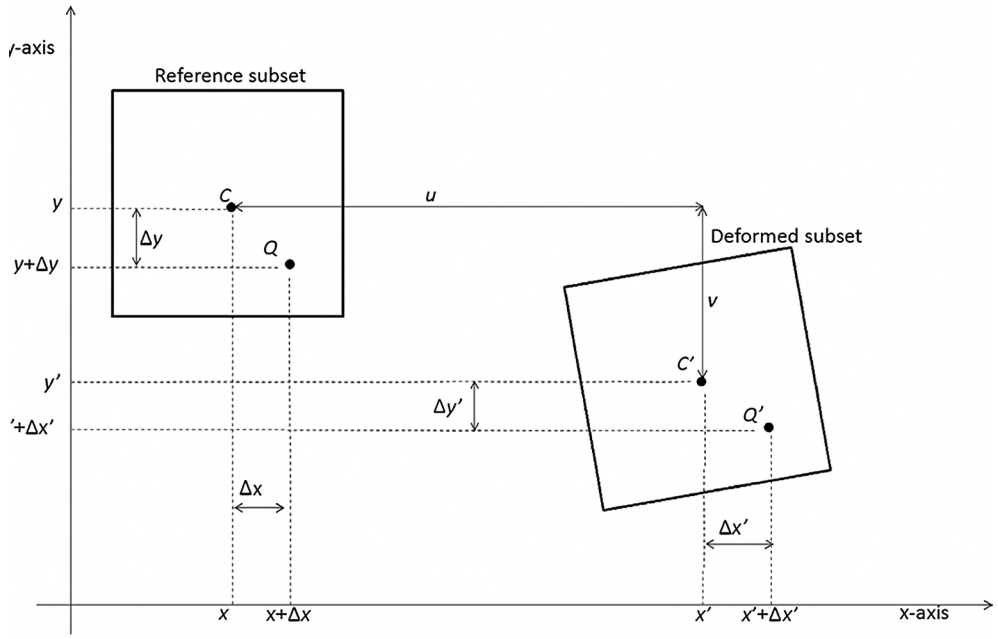

Figure 3.10 – Subset, before and after deformation [7].

Image Correlation

In summary, at the end of the image correlation process, the optimal values of the six variables mentioned previously are obtained, indicating the best match between the subsets before and after deformation. To achieve this, the six variables are organized into a vector, denoted P, as shown in Equation 3.5.

$$P = \begin{bmatrix} u & v & \frac{\partial u}{\partial x} & \frac{\partial u}{\partial y} & \frac{\partial v}{\partial x} & \frac{\partial v}{\partial y} \end{bmatrix} \tag{3.5}$$

The vector P serves as input for the calculation of the Correlation Coefficient $C(P)$, given by Equation 3.6.

$$C(P) = \frac{\sum_{i,j} \left(f(x,y) - g(\overline{x},\overline{y})\right)^2}{\sum_{i,j} f(x,y)^2} \tag{3.6}$$

This function $C(P)$ can be expanded in a Taylor series around P_0, as expressed in Equation 3.7.

$$C(P) = C(P_0) + \nabla C(P_0) \cdot (P - P_0) + \frac{1}{2}(P - P_0)^T \cdot \nabla^2 C(P_0) \cdot (P - P_0) \tag{3.7}$$

Here, the gradient is represented by the vector in Equation 3.8.

$$\nabla C(P_0) = \left[\frac{\partial C}{\partial u} \quad \frac{\partial C}{\partial v} \quad \frac{\partial C}{\partial \left(\frac{\partial u}{\partial x}\right)} \quad \frac{\partial C}{\partial \left(\frac{\partial u}{\partial y}\right)} \quad \frac{\partial C}{\partial \left(\frac{\partial v}{\partial x}\right)} \quad \frac{\partial C}{\partial \left(\frac{\partial v}{\partial y}\right)} \right] \tag{3.8}$$

and the Hessian matrix is described in Equation 3.9.

$$\nabla^2 C(P_0) = \begin{bmatrix} \frac{\partial^2 C}{\partial u^2} & \frac{\partial^2 C}{\partial u \partial v} & \frac{\partial^2 C}{\partial u \partial \left(\frac{\partial u}{\partial x}\right)} & \frac{\partial^2 C}{\partial u \partial \left(\frac{\partial u}{\partial y}\right)} & \frac{\partial^2 C}{\partial u \partial \left(\frac{\partial v}{\partial x}\right)} & \frac{\partial^2 C}{\partial u \partial \left(\frac{\partial v}{\partial y}\right)} \\ \frac{\partial^2 C}{\partial v \partial u} & \frac{\partial^2 C}{\partial v^2} & \frac{\partial^2 C}{\partial v \partial \left(\frac{\partial u}{\partial x}\right)} & \frac{\partial^2 C}{\partial v \partial \left(\frac{\partial u}{\partial y}\right)} & \frac{\partial^2 C}{\partial v \partial \left(\frac{\partial v}{\partial x}\right)} & \frac{\partial^2 C}{\partial v \partial \left(\frac{\partial v}{\partial y}\right)} \\ \frac{\partial^2 C}{\partial \left(\frac{\partial u}{\partial x}\right) \partial u} & \cdots & \cdots & \cdots & \cdots & \cdots \\ \vdots & \vdots & \vdots & \ddots & \vdots & \vdots \\ \cdots & \cdots & \cdots & \cdots & \cdots & \cdots \\ \frac{\partial^2 C}{\partial \left(\frac{\partial v}{\partial y}\right) \partial u} & \cdots & \cdots & \cdots & \cdots & \frac{\partial^2 C}{\partial \left(\frac{\partial v}{\partial y}\right)^2} \end{bmatrix} \tag{3.9}$$

The smaller the value of the correlation coefficient $C(P)$, the better the match between the subsets. To find the optimal combination of vector P values that minimizes $C(P)$, the function $C(P)$, expressed through its Taylor series expansion around P_0, is differentiated and set to zero. After algebraic manipulation, Equation 3.10 is obtained:

$$\nabla C(P) = \nabla C(P_0) + \nabla^2 C(P_0) \cdot (P - P_0)$$

$$\Rightarrow P = P_0 - \nabla^2 C(P_0)^{-1} \nabla C(P_0) \tag{3.10}$$

The above expression is then applied iteratively, as described in Equation 3.11, representing the Newton-Raphson method.

$$P^{(i+1)} = P^{(i)} - (\nabla^2 C(P^{(i)}))^{-1} \cdot \nabla C(P^{(i)}) \tag{3.11}$$

until convergence is reached for a given tolerance, as indicated in Equation 3.12.

$$\|P^{(i+1)} - P^{(i)}\| < \epsilon \tag{3.12}$$

Input of Image Data into the Correlation Framework

To determine the initial vector P_0 associated with each *subset*, a pre-processing step is performed based exclusively on the discrete data extracted from the digital images. In

this procedure, the correlation coefficient $C(P)$ is minimized in the discrete domain to obtain initial estimates for u and v at the center of the *subset*, while the four variables corresponding to the partial derivatives are set to zero (since continuous curves are not being considered). This initial vector provides a suitable starting point for the subsequent iterative application of the Newton–Raphson method [29].

Once the initial vector P_0 is determined, the pixel intensities around the estimated center of the *subset* are interpolated to form a continuous function. This step is essential because the iterative process relies on computing the gradient and Hessian matrix, which can only be obtained from a continuous representation of the intensity field [14].

Figure 3.11 shows the grayscale intensity as a function of the x and y positions, corresponding to the image displayed in Figure 3.8 (b). The upper plot represents the intensity in discrete form, as recorded by the pixels, which serves as the basis for the initial estimation of the point P_0. The lower plot shows the intensity as a continuous function obtained via bicubic (spline) interpolation, a method widely used in DIC software. This continuous representation enables the computation of the gradient and Hessian, allowing iterative refinement of the P_0 position and ensuring subpixel-level accuracy.

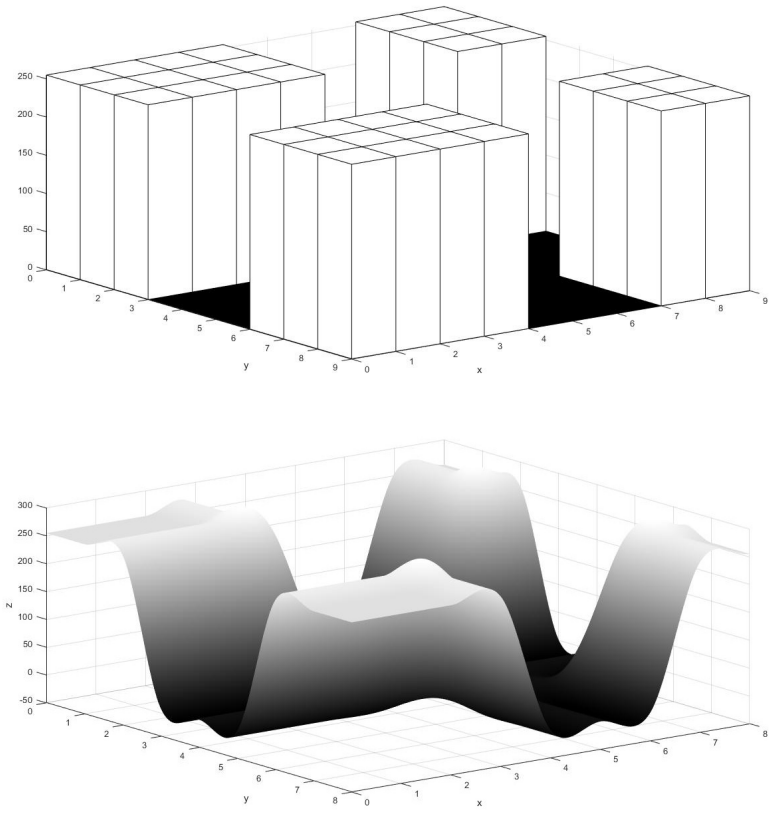

Figure 3.11 – Grayscale intensity as a function of the x and y positions. The upper plot represents the intensity in discrete form, while the lower one shows it as a continuous function.

3.3 High-Speed Digital Image Correlation

The understanding of mechanical phenomena associated with high strain-rate loading is essential in fields such as aerospace, automotive, and defense, where a detailed knowledge of the behavior of materials and structures under extreme conditions is crucial. In this context, the Digital Image Correlation (DIC) technique, combined with the use of high-speed (HS) and ultra-high-speed (UHS) digital cameras, stands out as a powerful tool for the accurate determination of displacement and strain fields in specimens subjected to such loading conditions [8, 9, 30, 31].

3.3.1 High-Speed (HS) and Ultra-High-Speed (UHS) Imaging Technology

High-speed imaging technology began to be developed even before the advent of digital image acquisition. Using arrangements with rotating prisms and photographic film, it was possible to achieve capture rates on the order of hundreds of thousands of frames per second. The transition to digital imaging only became viable with the advent of solid-state sensors, such as Charge-Coupled Devices (CCD) and Complementary Metal-Oxide-Semiconductor (CMOS) [8].

Solid-state sensors are composed of hundreds of thousands or even millions of individual detectors, each corresponding to a pixel in the final image. When these detectors are exposed to light, they produce an electric current proportional to the incident light intensity. The image is reconstructed by aggregating the intensities obtained from the detectors. The key to high-speed capture is to perform the detection, readout, and sensor reset cycle extremely quickly, minimizing the time interval between successive frames [9].

In this context, HS and UHS systems adopt distinct operational strategies. In HS systems, the goal is to optimize the readout cycle of a single sensor, increasing sensitivity and, most importantly, the data transfer rate, which is the most critical factor. CMOS-type sensors are generally used, allowing rates of up to approximately 100,000 fps. The typical arrangement of an HS system can be seen in Figure 3.12 (a) [8, 9].

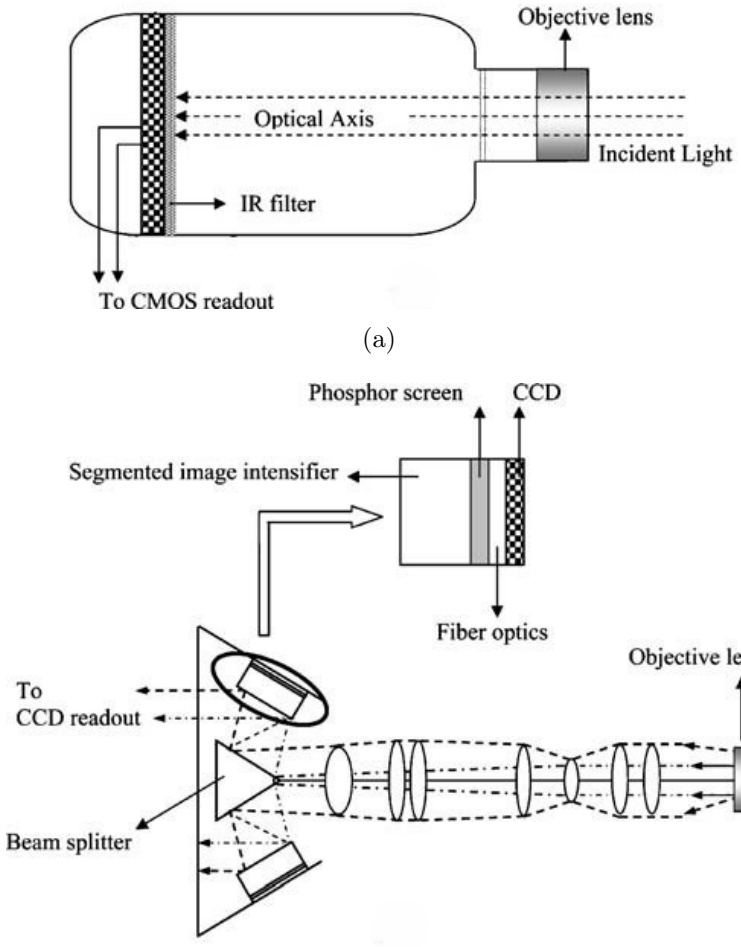

Figure 3.12 – Optical setup and detector of a HS imaging system (a) and Optical setup and detectors of an UHS imaging system (b) (adapted from [30]).

UHS systems, on the other hand, rely on the use of rotating prisms, similar to the old film-based analog cameras, along with combinations of special lenses, optical fibers, and even image intensifiers. In this configuration, the scene is split and projected onto multiple Charge-Coupled Device (CCD) sensors, as illustrated in Figure 3.12 (b). By aggregating the images recorded by each detector, UHS cameras can achieve extremely high frame rates, ranging from several hundred thousand to millions of frames per second [8, 9, 30].

3.3.2 High-Speed DIC Applications

High-speed DIC combines the strengths of two fields that have evolved considerably in recent years: on one hand, DIC provides a non-destructive nature and the ability to deliver full-field measurements without compromising specimen integrity; on the other hand, high-speed photometry enables the capture of transient, short-duration phenomena that were previously difficult to characterize [8, 9].

This combination makes the technique particularly suitable for studying designs involving dynamic events such as high rotations, vibrations, explosions, and impacts. Furthermore, high-speed DIC allows for *in situ* analysis of material mechanical behavior, i.e., directly during loading, providing insights in areas such as fatigue mechanics and high strain-rate phenomena in materials [9].

The work by Pazur et al. [32] clearly demonstrates how integrating Digital Image Correlation (DIC) with high-speed camera technology enables the analysis of mechanically challenging behaviors. As an optical and non-intrusive technique, DIC is particularly advantageous for studying rotating components, where traditional methods such as extensometers encounter significant limitations. These limitations include physical interference with the system, difficulties in sensor connections, and restricted measurement points, all of which may compromise the representativeness of the results [32].

Rotating elements, in turn, impose additional challenges for image capture, requiring the use of cameras with high acquisition rates capable of "freezing" motion and providing images suitable for digital correlation. By combining these two capabilities, the authors demonstrate the application of the technique to obtain the full-field deformation of an aircraft propeller blade, as illustrated in Figure 3.13 [32].

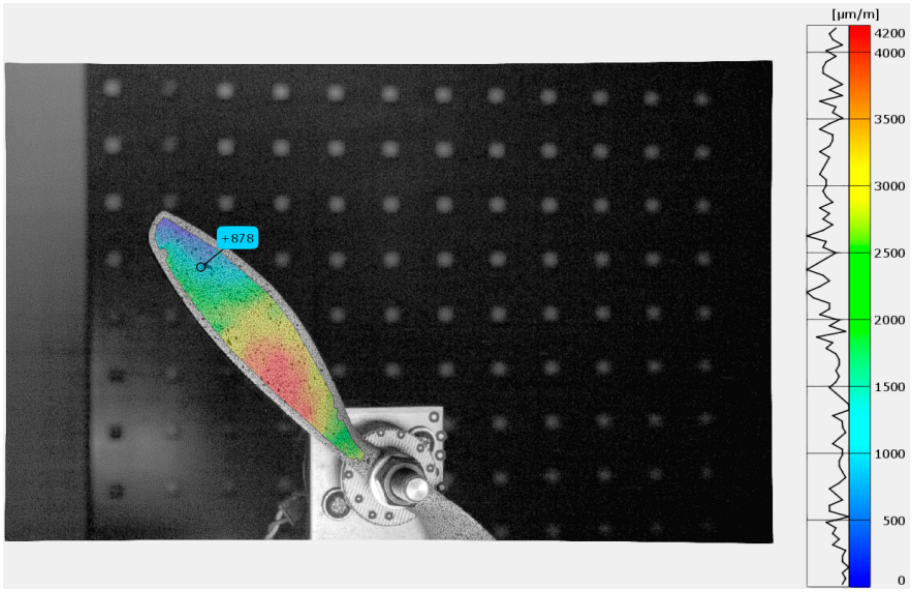

Figure 3.13 – Application of the DIC technique combined with a high-speed (HS) image acquisition system for the characterization of deformations in an aircraft propeller blade [32].

In vibration studies, optical methods offer an intrinsic advantage over mechanical techniques, as they do not impose additional loading on the structure during measurement, thereby avoiding the introduction of noise. Furthermore, when compared with results obtained from the 3D Scanning Laser Vibrometer (SLV) technique, DIC shows strong potential for full-field vibration measurements [9].

The advancement of high-speed photometry has been largely driven by the need to observe explosive events, with integration of DIC widely employed in monitoring structures subjected to pulses resulting from these events. Moreover, the significant relevance of combining DIC with high-speed imaging in impact testing is emphasized, showing great applicability in the development phase of new products, particularly in the aerospace and automotive sectors, where assessing impact-induced damage is crucial [8, 9].

In the study of material mechanical behavior, HS and UHS DIC enables full-field capture of transient phenomena during dynamic tests, complementing classical experiments. For instance, in Taylor Impact Testing, traditional methods typically compare only the initial and final states of the specimen to determine material response at high strains and strain rates. In contrast, DIC allows continuous recording of the entire deformation history throughout the transient phase. Similarly, in Hopkinson bar tests, rather than being limited to local measurements from strain gauges, full-field deformation data can be obtained, providing a more comprehensive view of the specimen's behavior [33, 34].

Another area where High-Speed DIC has contributed to investigating material behavior is fracture mechanics. Applying the technique to measure real-time deformations during crack initiation and propagation shows good agreement with results obtained through simulations or strain gauges [35, 36].

3.3.3 High-Speed DIC Challenges

There are several challenges in applying high-speed DIC, mainly arising from the photometric requirements of this type of measurement. When studying a dynamic phenomenon, it is necessary to define an appropriate frame rate and exposure time. Once these parameters are established, equipment is selected to achieve the best contrast with the lowest noise.

In high-speed photometry, achieving high-contrast, low-noise images is particularly challenging due to the physical limitations of the sensors. The frame acquisition cycle essentially works as follows: the sensors must be sufficiently exposed to light to generate an electric charge via the photoelectric effect, which is then converted into digital information and stored, and finally reset to capture the next frame. Thus, the exposure time and the storage cycle are the main factors limiting the reduction of the interval between frames, with the latter being the most critical [9].

At first glance, it may seem appropriate to select an imaging system with the highest possible frame rate, as this would "guarantee" capturing the dynamic phenomenon. However, to obtain sharp images in high-speed analyses, it is not sufficient to consider only the frame acquisition capability. The system must allow an exposure time short enough to produce a "frozen" image of the desired instant. For most current DIC applications, subpixel accuracy is desired; therefore, the exposure time must be such that the

displacement due to deformation during this period remains below the desired precision level, avoiding motion blur. Since reducing exposure time decreases sensor light intensity, special illumination conditions are required to compensate for the short exposure time [8].

In single-optical-path systems, such as High-Speed (HS) systems with CCD detectors, as illustrated in Figure 3.12 (a), image distortions originate from the camera model and are parametric in nature. Calibration and correction methods estimate these parameters and correct the image, ensuring the accuracy of the obtained information.

In contrast, in Ultra High-Speed (UHS) systems, multiple optical paths exist, as illustrated in Figure 3.12 (b), with each path directed to a separate CCD detector. This introduces misalignment errors between images, since light is not always projected onto the same relative position on each detector. Furthermore, due to intensity losses from the more complex optical path, light intensifiers are required to achieve higher contrast. However, this approach introduces non-parametric distortions; therefore, traditional calibration and correction models are not effective [8, 30].

High-speed photometry equipment is intrinsically expensive, and for three-dimensional applications these costs at least double due to the need for two cameras, as well as precise calibration and synchronization requirements. In these high-speed contexts (HS and UHS), a major difficulty lies in ensuring that the acquisition start of both cameras occurs simultaneously. Small temporal deviations between frames that should be concurrent can introduce significant measurement errors. To mitigate this issue, Tiwari et al.[30] proposed a correction method capable of compensating synchronization differences of up to ± 2.5 ns [30, 37].

A key difficulty in advancing High-Speed and Ultra High-Speed techniques is the ability to transfer and store the enormous data flow generated by the sensors. Strategies to mitigate this bottleneck include in-situ storage (memory integrated into the sensor) and optimizations of data transfer to memory units. A well-known solution is the ISIS-CCD sensor (In-Situ Storage Image Sensor), which integrates memory into the pixel array and enables acquisition rates on the order of 1 million frames per second using a single detector and optical path, helping to reduce noise and increase acquisition fidelity [8].

Another relevant factor is the large volume of data generated: given the limited storage and processing capacity of available computers, the use of triggers and careful experimental planning becomes essential to capture only the instants of interest, thereby reducing the volume of data to be processed and managed.

3.4 Integration of DIC with Finite Element Analysis (FEA)

The use of numerical modeling in solid mechanics to predict the behavior of bodies under loading is well established, primarily through the Finite Element Analysis (FEA)

method. Proper definition and computational implementation of a numerical model are essential to ensure that it adequately represents the governing equations. Validation of the model through comparison with experimental data is particularly important in cases where no prior results of analogous phenomena are available to serve as a reference for assessing the reliability of the obtained results.

In the context of experimental validation, agreement between the reaction forces predicted by the numerical model and the experimentally obtained data is not sufficient to confirm the model's validity due to the problem of non-uniqueness [10]. In other words, different models, or even the same model with different parameter combinations, may produce similar global reactions. Therefore, in addition to compatibility of global forces, it is essential to verify whether the displacement and strain fields throughout the analyzed body show good agreement between the experiment and the numerical simulation.

There are several ways to integrate results from Finite Element Analysis (FEA) with full-field experimental measurements obtained through Digital Image Correlation (DIC). This is a constantly evolving field, given its ability to enhance the physical representativeness and reliability of numerical models, particularly in describing complex phenomena.

In this work, the integration between FEA and DIC is classified by the author into two main approaches. The first, using DIC as an experimental validation technique for FEA modeling, consists of independently obtaining numerical and experimental results, followed by comparison of displacement or strain fields as a means of validating the numerical simulation. The second involves using DIC data to obtain or optimize parameters that serve as inputs for an FEA simulation, characterizing the so-called Inverse Method.

3.4.1 Using DIC for Experimental Validation of FEA

3.4.1.1 Direct Comparison of DIC-FEA Results

Through direct comparison between DIC and FEA results, it is possible to verify whether the strain field of the model is globally consistent with the experimental data, ensuring a more accurate numerical description of the phenomenon under study. Visualization of full-field strains obtained experimentally provides insights that allow model adjustments, enabling a more faithful representation of the phenomenon [8, 10, 38].

At first glance, it may seem that direct comparison between fields measured by DIC and predicted by FEA is sufficient to validate a model; however, this is not entirely correct. There is an essential methodological difference: FEA generates fields by solving the constitutive equations over a mesh, while DIC obtains the fields experimentally via optical methods.

Thus, a direct comparison, without proper data processing or specific experimental procedures, tends to be qualitative and insufficient for rigorous quantitative validation or parameter identification. Nevertheless, direct comparison is quick and practical: it serves

as a useful screening tool to detect major discrepancies, check whether the regions of highest demand coincide, and guide decisions for more detailed investigations.

Several recent studies have employed Digital Image Correlation (DIC) as a tool for experimental validation of Finite Element Analysis (FEA), based on direct comparison of the obtained displacement and/or strain fields. Generally, the results do not show rigorous quantitative agreement, as differences may arise from inherent limitations of direct comparison between the two techniques, as previously mentioned, or from aspects related to the material constitutive model or boundary conditions. Nonetheless, good qualitative agreement is generally observed, indicating the overall consistency of the adopted modeling approach

Spranghers et al. [39] performed Finite Element Analysis (FEA) simulations to study the mechanical behavior of aluminum plates subjected to open-air explosions. In the stage where the strain field in the plate plane obtained by FEA was compared with that measured experimentally via HS DIC, the results were found to be qualitatively adequate, particularly regarding the location of strains, as illustrated in Figure 3.14.

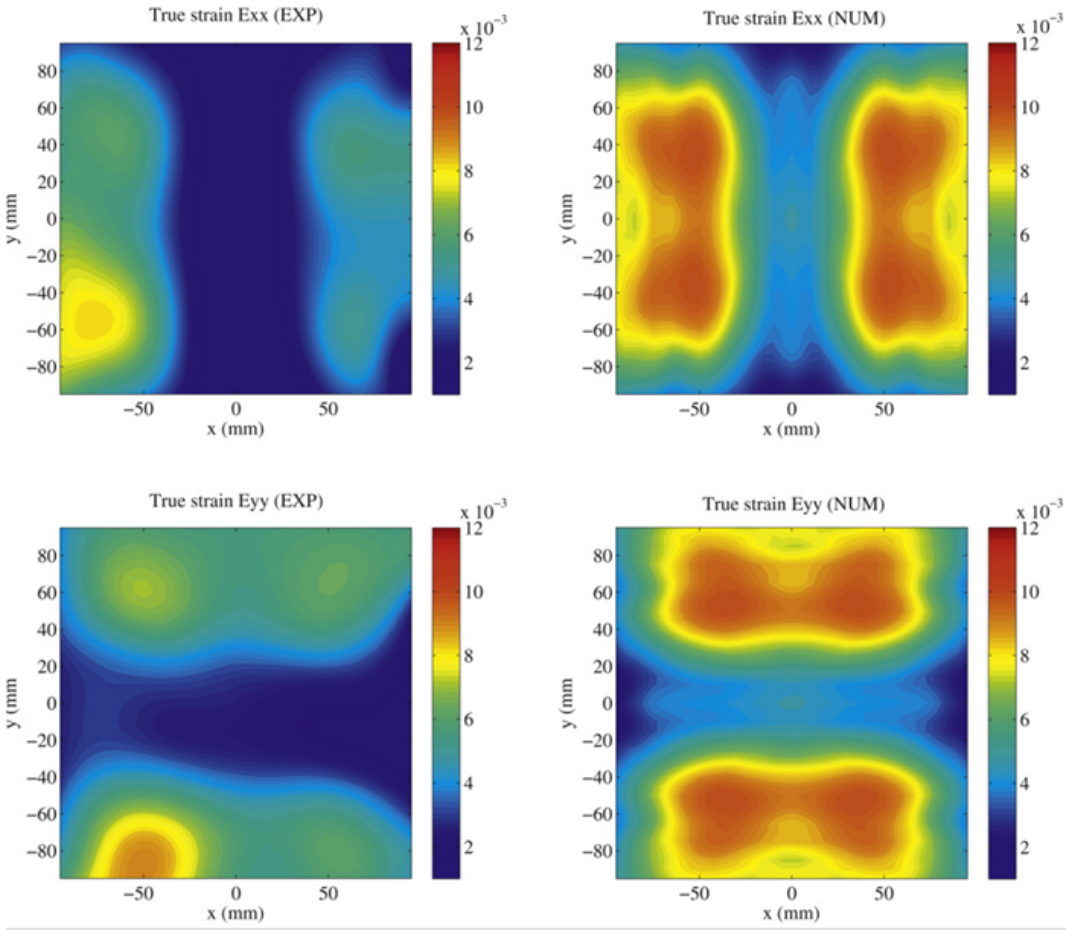

Figure 3.14 – Comparison of the strain fields E_{xx} and E_{yy} obtained from FEA simulation (NUM) and HS DIC measurement (EXP) in an aluminum plate subjected to a shock wave from an explosion, recorded 0.48 ms after trigger activation (adapted from [39]).

Similarly, Oka et al. [40] applied DIC as a technique for validating finite element results in the simulation of drop tests of nuclear material container boxes. In Figure 3.15, the top-left corner shows the delineation of the Region of Interest (ROI), located at the container edge, indicated by a trace. This region is also represented in red on the mesh defined in the FEA model, as shown in the bottom-left corner of the image. The strain results E_{xx} and E_{yy} between two spatial points located within this region, caused by a 4.3 m container drop, are compared in the top-right and bottom-right figures, respectively. Good qualitative agreement between FEA and DIC results can be observed, although there is a slight quantitative difference.

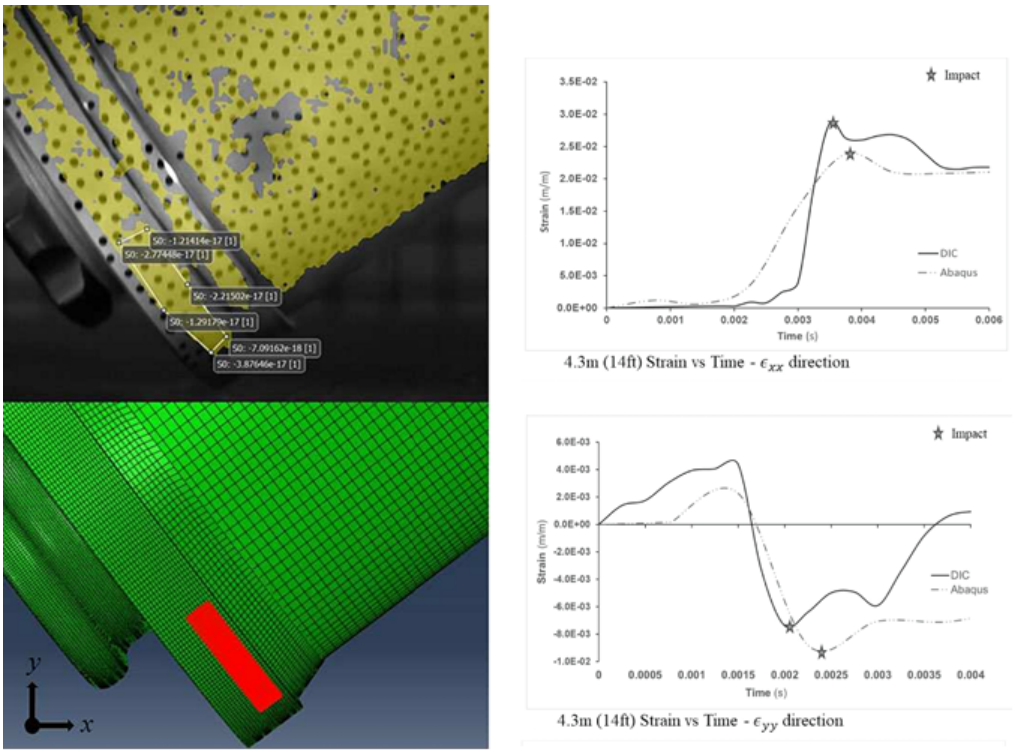

Figure 3.15 – Comparison of the strain fields ε_{xx} and ε_{yy} obtained from FEA simulation and DIC measurement of a nuclear material storage container subjected to a 4.3 m drop test (adapted from [40]).

Finally, in the work by Lopes et al. [27], DIC was applied to a bus chassis with the objective of mapping displacements and strains resulting from a frontal collision, simulated through pendulum impact. The technique was used as a tool to assess the performance of the crashworthiness model developed in FEA software. In Figure 3.16, the mapping of the chassis displacement u_{yy} shows good agreement with the observed phenomenon, although quantitative differences are present.

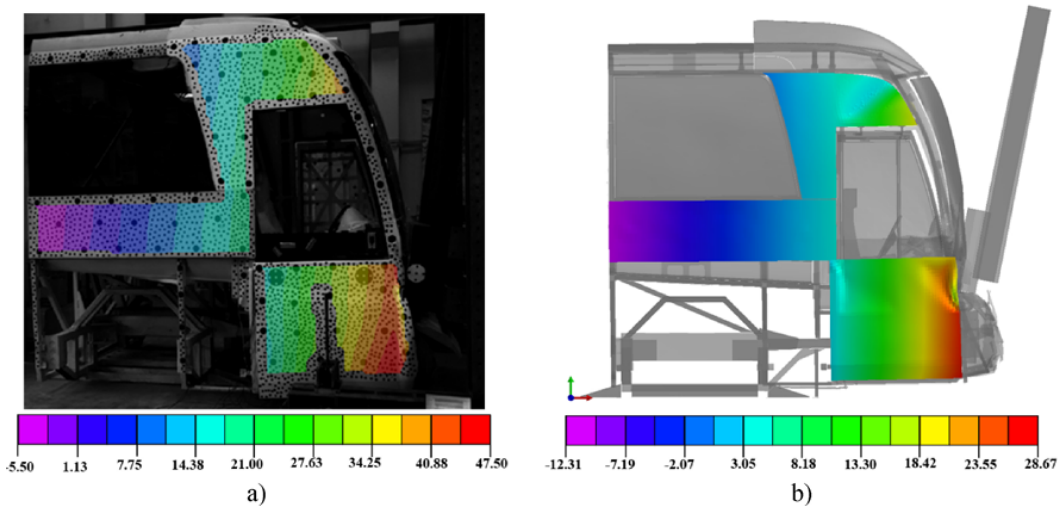

Figure 3.16 – Comparison of the displacement fields u_{yy} obtained from DIC measurement (a) and FEA simulation (b) of a bus chassis under pendulum impact (adapted from [27]).

3.4.1.2 DIC-FEA Comparison After Data Treatment

Lava et al. [10] list six intrinsic inconsistencies between DIC data and FEA results that can lead to discrepancies in quantitative comparison: strain formulations, coordinate systems, data locations, strain computation algorithms, spatial resolutions, and filtering procedures. These differences stem from the distinct nature of the techniques and can cause deviations even when the constitutive model is appropriate.

In their study, Lava et al. [10] showed this effect by eliminating any modeling error: the "experimental" DIC data were generated from the exact FEA displacements, with artificial addition of typical DIC noise. Therefore, any errors observed from the direct subtraction between the FEA fields and the "experimental" data result solely from differences between the techniques, not from errors in the numerical model design.

The first approach to mitigate the error associated with comparing the two techniques was to perform an interpolation scheme for each of the strain fields obtained via FEA and DIC, and then compare these interpolated fields, ensuring the alignment of coordinate systems and smoothing of data locations. Additionally, coincidence in strain formulations was ensured, which, although it may seem trivial, is common for each software package to adopt its own default formulation, which does not always match [10].

This approach can eliminate part of the discrepancies. However, such alignment does not fully resolve the differences associated with strain computation algorithms, spatial resolution, and filtering procedures, which remain as sources of bias. In Figure 3.17, the persistence of absolute error in the strain field between FEA and DIC after field interpolation and subtraction can be observed, precisely illustrating the limitation of direct comparison, even when an interpolation scheme is adopted to aid positional alignment of the data

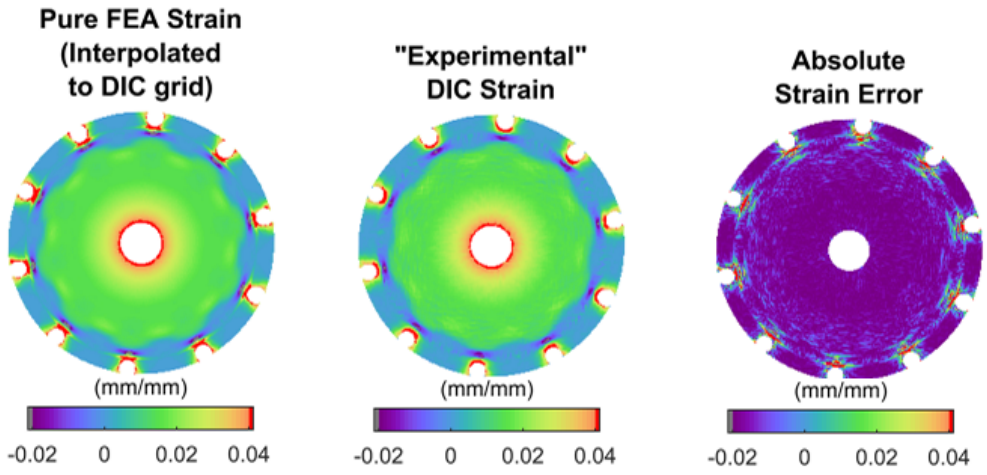

Figure 3.17 – Absolute error resulting from the subtraction of the interpolated FEA and "experimental" DIC strain fields (adapted from [10]).

The second approach consisted in "levelling" the FEA results by means of a DIC engine: a random *speckle* pattern was applied to the surface of the solid model, and that pattern was deformed according to the new nodal positions predicted by the FEA simulation, generating synthetic images that were processed by the same correlation algorithm employed in the experimental data.

In this way, the FEA results are converted into the "DIC format", enabling direct comparison with the "experimental" data under identical *strain*-calculation algorithms, spatial resolutions, and filtering procedures. As shown in Figure 3.18, this procedure substantially mitigates discrepancies associated with such differences.

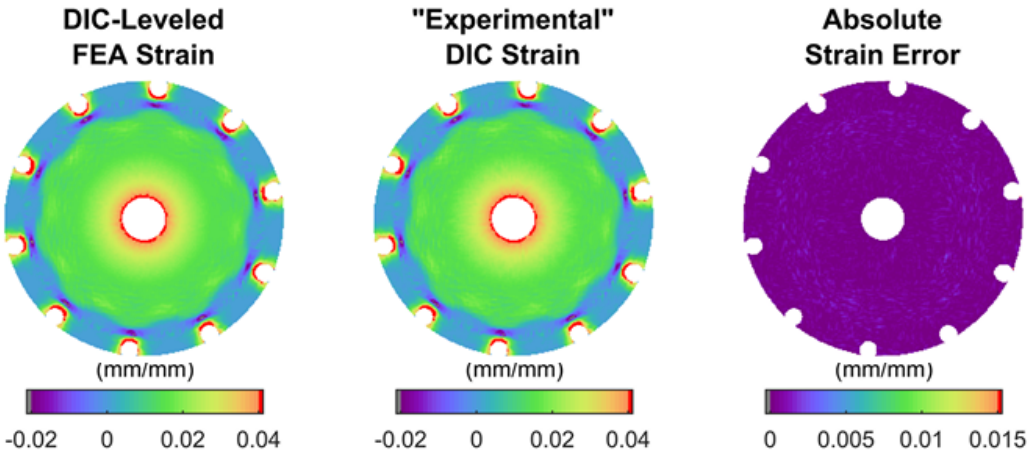

Figure 3.18 – Absolute error resulting from the subtraction of the FEA and "experimental" DIC strain fields using DIC-*levelling* (adapted from [10]).

3.4.2 DIC for Inverse Method Applications in FEA

When performing numerical modeling in the field of structural mechanics, the conventional procedure consists in providing the model with input data such as initial conditions, load cases, boundary conditions (e.g., constraints, joints, and contacts), and material properties. Based on these inputs, the numerical model solves the equilibrium equations, yielding as output the displacement and strain fields of the analyzed body.

For relatively simple phenomena, where the input data are well known, a close correspondence between simulation results and experimental observations can be expected. However, for phenomena that are highly sensitive to boundary conditions and material parameters, such as modal analyses, impact tests, and fatigue studies, small inaccuracies in defining the input parameters may lead to significant discrepancies between the numerical model and the experimental test [41].

A widely employed approach for determining appropriate input conditions in finite element models is the inverse method. In this technique, the model's inputs are adjusted so that its outputs converge toward the experimental results. The inverse method can be formulated as an optimization problem, in which the input parameters are tuned until the discrepancy between numerical and experimental results is minimized and remains below an acceptable error threshold.

Experimental validation through the inverse method enables a more accurate understanding of the boundary conditions and material properties in a given case study [42]. Consequently, when a similar structural problem arises, where experimental testing is not feasible, the previously obtained and validated information provides a reliable basis for defining the input conditions. Thus, numerical modeling of new cases becomes more robust and closer to the actual structural behavior.

3.4.2.1 Inverse Method for the Identification of Material Properties

The proper definition of the material constitutive model and its corresponding parameters is fundamental to ensure that a numerical model is consistent with experimental results. As the phenomena to be simulated become more complex, the constitutive model of the employed materials is generally more sophisticated.

For example, in a static analysis of an isotropic material under linear elastic behavior, where gravity effects are negligible, the material's constitutive model can be defined solely by Young's modulus (E) and Poisson's ratio (ν), obtained from a single tensile test with extensometers. However, when the investigated phenomenon involves loading beyond the linear elastic regime or more complex material behaviors, the constitutive model of the employed materials is more sophisticated, requiring the determination of a larger set of constitutive parameters and, consequently, multiple experimental tests.

With the advancement of non-conventional testing, such as full-field displacement

tests, where strains and displacements can be used as inputs for the inverse method, it has become possible to reduce significantly the number of laboratory tests required to define a material's constitutive model. More complex tests stimulate different modes of material response, and through optimization techniques, it is possible to estimate the values of a larger number of constitutive parameters.

In Figure 3.19, adapted from Chen et al. [43], the aforementioned evolution can be observed, following the nomenclature adopted by Pierron and Grédiac [44]. To determine the parameters of material's constitutive models used in complex phenomena, i.e., materials subjected to multiple loading modes, a large number of conventional tests, referred to as Materials Testing 1.0, was required. These tests are statically determined, provide limited aggregated data, generally relate to only a single loading mode.

With the adoption of non-conventional tests, referred to as Materials Testing 2.0, different loading modes are combined within a single test (thus reducing the total number of tests required). These tests explore heterogeneous strain fields and make use of inverse techniques to extract the constitutive parameters. In this context, the identification is performed through an iterative process: by updating/optimizing the parameters of the numerical model (e.g., via FEMU – Finite Element Model Updating, VFM – Virtual Fields Method, or Integrated Digital Image Correlation (IDIC)), convergence is sought toward the material's constitutive parameters that best reproduce the experimental results obtained.

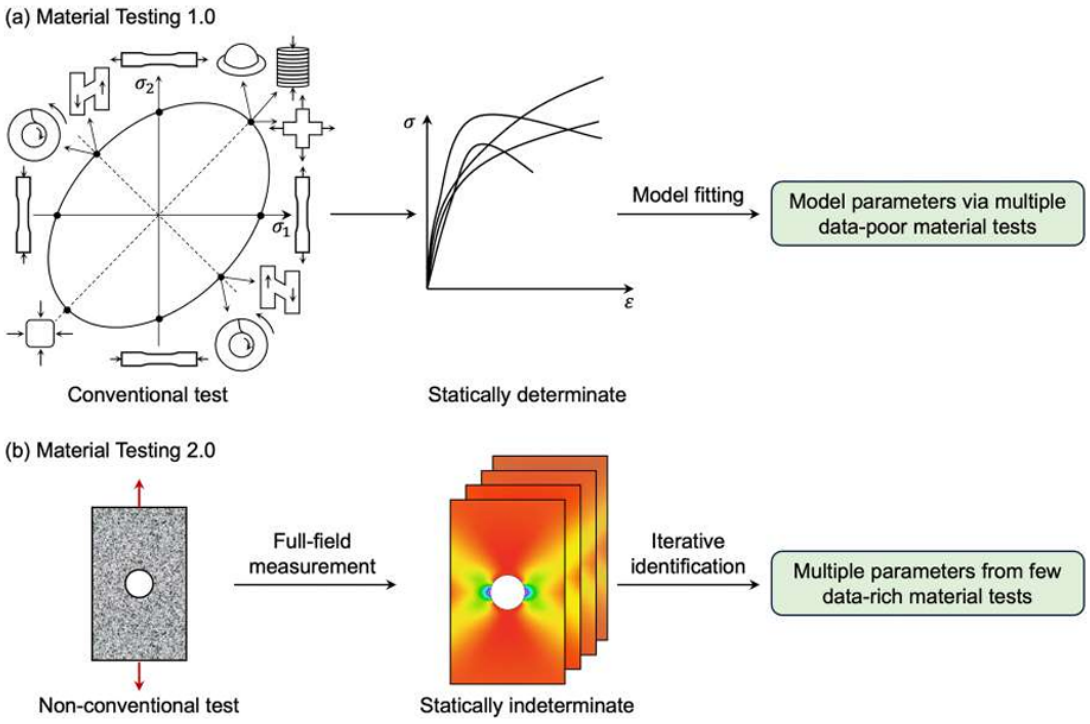

Figure 3.19 – While Materials Testing 1.0 requires multiple tests to determine the constitutive model of a material, Materials Testing 2.0 allows the constitutive model to be obtained with fewer tests through the use of the inverse method [43].

One of the methodologies that has been widely adopted in the context of Materials Testing 2.0 for identifying material constitutive parameters is FEMU-DIC (Finite Element Model Updating combined with Digital Image Correlation). In Figure 3.20, Chen et al. [43] present a representative flowchart of this approach.

In this methodology, the strain field is initially obtained experimentally using DIC applied to a complex mechanical test. In parallel, numerical modeling is performed via FEA, considering an assumed constitutive model and initial values for the material parameters.

The numerical and experimental fields are then compared through a cost function. If the criterion of this function is not satisfied, the vector of constitutive parameters is iteratively adjusted until convergence between the numerical and experimental results is achieved [43].

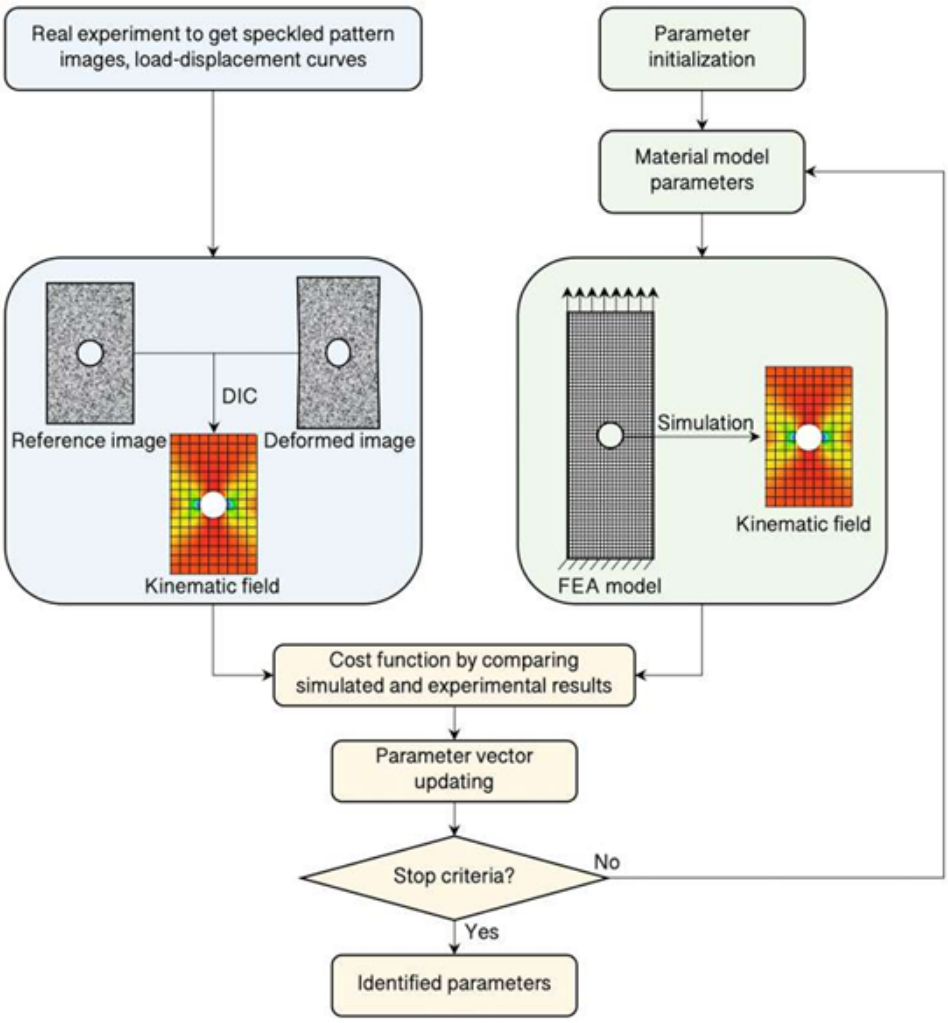

Figure 3.20 – Optimization workflow of FEMU-DIC: iterative adjustment of constitutive parameters to minimize a cost function between FEA predictions and displacement/strain fields measured by DIC [43].

3.4.2.2 Inverse Method for the Identification of Boundary Conditions

The DIC technique provides displacement fields that can be used as input data in the inverse method, enabling not only the identification of material constitutive model parameters but also the updating of boundary conditions in the numerical model, thereby improving its agreement with experimental results.

This is crucial when boundary condition simplifications adopted in the modeling are far from reality in complex cases: for instance, contacts treated as rigid in the model may exhibit local deformations in the experimental test, altering the equilibrium equations and, consequently, the predicted results. Lovejoy et al. [11] demonstrated that employing DIC to measure the actual response of support and contact regions enables correction of boundary condition data in the numerical model, improving significantly the correlation between numerical and experimental results.

DIC analysis was also employed by Turón et al. [12] to more accurately describe boundary condition behavior. The authors reported the challenges of properly modeling the actual boundary conditions of a reinforced concrete beam subjected to torsion and used DIC to enhance boundary representation within their finite element analysis (FEA).

The work of Fedele [13] about the mechanical behavior of adhesive joints properly employs the inverse method using DIC-derived data, in which the cohesive parameters of the adhesive and the boundary displacements of the region of interest are simultaneously estimated and updated. To this end, the author formulates a cost function that combines the errors between measured and numerical fields and applies an iterative optimization scheme until parameter convergence is achieved. This example demonstrates that the inverse method can go beyond the simple identification of material parameters, it also corrects boundary conditions, making the numerical model more consistent with the experimentally observed behavior.

3.5 Applications of DIC in Experimental Mechanics

3.5.1 Material Testing and Characterization

Digital Image Correlation (DIC) has become a valuable tool in material testing, as it enables the detailed observation of strain distribution across a specimen during loading. It is widely applied in uniaxial, biaxial, and multiaxial tests to evaluate the deformation behavior of metals, polymers, composites, and ceramics. The full-field strain data obtained from DIC allow the identification of key mechanical properties such as Young's modulus, yield strength, and Poisson's ratio. Moreover, DIC is particularly useful for studying localized deformation and fracture initiation in heterogeneous materials, including composites and structures with defects.

Regarding metallic materials, Hedayati et al. [45] determined the strain and plastic anisotropy coefficient of aluminum 1050 specimens using DIC. Following the ASTM E8 tensile testing standard, the authors recorded the experiment with a Sony camcorder and processed the images in MATLAB. The strain data obtained from DIC were compared with extensometer measurements, showing that when the experimental setup is properly configured, the error can be kept below 2%. Similarly, Kato [46] measured the strain distribution in metals under tensile loading using DIC to analyze the stress–strain relationship. The Stress-strain relation for aluminum was compared with the result for steel which the author already published. It was found that we have to measure strain distribution and consider local maximum strain to evaluate stress-strain relation accurately. Schwindt et al. [47] employed DIC to evaluate the forming limit curve (FLC) of a 1.1 mm thick DP-780 steel sheet, as shown in Figure 3.21(a). Tensile and Nakajima tests with reduced tool dimensions were conducted, revealing that a smaller 40 mm punch tends to overestimate the limit strains due to strain gradients through the sheet thickness indicating that this configuration is unsuitable for steels thicker than 1 mm.

Moving to composite materials, Bogusz [48] investigated the in-plane shear behavior of glass fiber laminates using a $\pm 45^{\circ}$ off-axis tension test. The results indicated that strain localization followed the fabric texture and intensified with increasing deformation. The shear stress–strain response was found to depend strongly on strain distribution and strain gauge placement, while the appearance of microcracks in the resin contributed to nonlinear shear behavior. Likewise, Kashfuddoja et al. [49] characterized polymer–matrix and carbon fiber–reinforced composites through a full-field, non-contact DIC technique, as shown in Figure 3.21 (b). Mechanical properties obtained via DIC closely matched those from conventional and analytical approaches. The study also demonstrated that subset size significantly influences the accuracy of material property estimation, while step size mainly affects the resolution of the strain field near geometric discontinuities. These findings were validated through finite element analysis (FEA), confirming that optimized DIC parameters can yield highly accurate strain predictions.

DIC has also proven effective for analyzing natural and bio-based composites. For instance, von Boyneburgk et al. [50] examined the mechanical behavior of Wood Textile Composites (WTC) composed of willow wood fabrics and polypropylene through tensile and three-point bending tests. The material exhibited direction-dependent strength and elongation due to its heterogeneous microstructure, displaying typical fiber composite behavior. DIC was employed to map strain distributions in the elastic range, as shown in Figure 3.21 (c), and the results were validated using finite element simulations based on an orthotropic constitutive model. Chen et al. [51] investigated the tensile behavior of all-cellulose composites prepared from filter paper via partial dissolution in 1-ethyl-3-methylimidazolium acetate. The authors compared results obtained directly from a tensile testing machine with those from a two camera DIC system. Using virtual extensometers

and surface-averaged strain data, they constructed nominal and true stress–strain curves to determine Young's modulus, tensile strength, elongation, and toughness (Figure 3.21 (d)). The study showed that DIC-based stress–strain curves differed notably from those measured by the testing machine, significantly influencing the calculated Young's modulus and elongation at break.

Finally, DIC has also been applied to soft materials. Zeng and Bailly [52] investigated the dynamic response of gelatin-based soft materials under impact loading using a modified Split Hopkinson Pressure Bar (SHPB) equipped with PVDF sensors to capture low-magnitude forces, as presented in Figure 3.21 (e). High-speed imaging combined with DIC enabled the measurement of non-homogeneous displacement and strain fields, allowing for the determination of transient stress distributions. The stresses obtained via DIC showed strong agreement with PVDF measurements, confirming strain-rate sensitivity between 81 s^{-1} and 269 s^{-1} and verifying a uniaxial compression state in the specimen's central region.

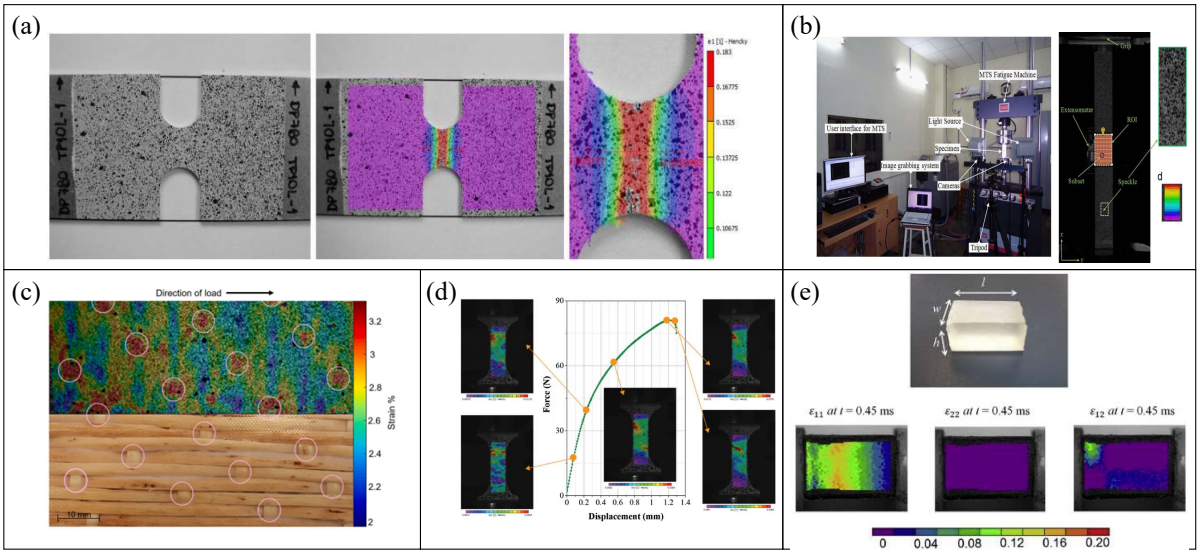

Figure 3.21 – Material testing and characterization using DIC: (a) Technique applied on tensile specimens [47]; (b) Experimental setup and post-processing of polymer–matrix and carbon fiber–reinforced samples [49]; (c) Strain in the specimen under tensile load compared to the specimen without load [50]; (d) True strain field in the longitudinal direction obtained by DIC as function of displacement [51] and (e) Axial strain, lateral strain and distorsion strain on the lateral face of the speciment [52].

3.5.2 Impact and Dynamic Testing:

One of the most significant applications of DIC is in dynamic testing, where it is used to measure the deformation of materials and structures under high strain rates, such as impact, explosion, and crash tests. In these tests, materials often undergo rapid and large deformations that are difficult to capture using traditional strain gauges or other

point measurement techniques. DIC, particularly high-speed DIC, provides full-field strain maps that can capture the dynamic response of materials in real-time. This capability is essential in fields such as aerospace, automotive, and defense, where understanding the behavior of materials under dynamic loading is critical for safety and performance.

To validate the numerical analysis under impact and dynamic conditions the DIC methodology has been used in different engineering fields like, in automotive where Jonsson and Kajberg [53] proposed an approach to address the crash performance of vehicle crashbox axially and dynamically compressed through high-speed imaging combined with 3D digital image correlation (3D-DIC) as presented in Figure 3.22 (a). Where according to the authors findings the high-speed imaging and 3D-DIC could effectively be used to evaluate the crashworthiness of components by allowing a detailed tracking of crack initiation, crack propagation, and the evolution of damage. Also analysing a crashworthiness of the frontal crashworthiness of M3 Class III coaches , Lopes et al. [27] performed experimental and numerical analyses to enhance driver safety during frontal impacts. The experimental setup involved a 2500 kg pendulum impact test releasing 55 kJ of energy against the vehicle structure, following adaptations of the ECE R29 regulation. Advanced monitoring techniques, including Digital Image Correlation (DIC), strain gauges, and accelerometers, were employed to track strain evolution and structural deformation. The DIC system provided full-field strain measurements, enabling detailed assessment of local damage and validation of the numerical model.

In the aerospace industry, DIC provides similar high-fidelity data for structural validation, Gardner et al. [54] implemented three-dimensional Digital Image Correlation (DIC) during NASA's Shell Buckling Knockdown Factor (SBKF) project to characterize the full-field displacement and strain behavior of cylindrical shell structures (Figure 3.22 (b)). The DIC data provided high-fidelity validation for finite element buckling simulations and revealed that the anomalous response of the linear variable displacement transducers (LVDTs) was caused by a local settling of the test article into the potted attachment rings, approximately 0.0015 inch. In larger scale tests, Littell [55] employed Digital Image Correlation (DIC) to measure strain and deformation during full-scale aircraft crash tests conducted at NASA's Langley Research Center as presented in Figure 3.22 (c). The experiments involved three Cessna 172 general aviation aircraft, where DIC enabled real-time mapping of strain and deformation across the airframe immediately after impact. This approach provided valuable insights into crash severity and facilitated the identification of localized damage regions.

From dynamic analysis, DIC has also been applied in Experimental Modal Analysis (EMA) to extract natural frequencies and mode shapes [56]. Figure 3.22 (d) illustrates the setup and the first two modal shapes from Mastrodicasa et al. [57], who proposed a DIC-based EMA approach to overcome the limitations of traditional point-wise sensors in large or lightweight structures. Their method reconstructs high-frequency vibration

responses beyond the Nyquist–Shannon limit using low-speed cameras, validated both numerically and experimentally on an aircraft mock-up, showing strong agreement with accelerometer data. Similarly, Poozesh et al. [58] employed a multi-camera DIC system to assess the displacement and modal behavior of a wind turbine blade shown in Figure 3.22 (e), detecting in-plane displacements as small as 0.2 mm with less than 3% error compared to strain gauges, and estimating the first five natural frequencies with errors below 2% relative to conventional accelerometer measurements.

Also from the DIC, is possible to evaluate in explosion conditions. Guildenbecher et al. [59] employed high-speed optical imaging and DIC for three-dimensional quantification of explosively driven metal fragmentation. The DIC technique provided non-contact measurements of case velocities, strains, and strain rates immediately after detonation, while stereo imaging was used to track fragment masses and velocities at later times. The experimental data, obtained using RP-80 detonators, were compared with 3D simulations, showing good agreement and demonstrating the potential of DIC for validating high-strain-rate and fragmentation models as presented in Figure 3.22 (f).

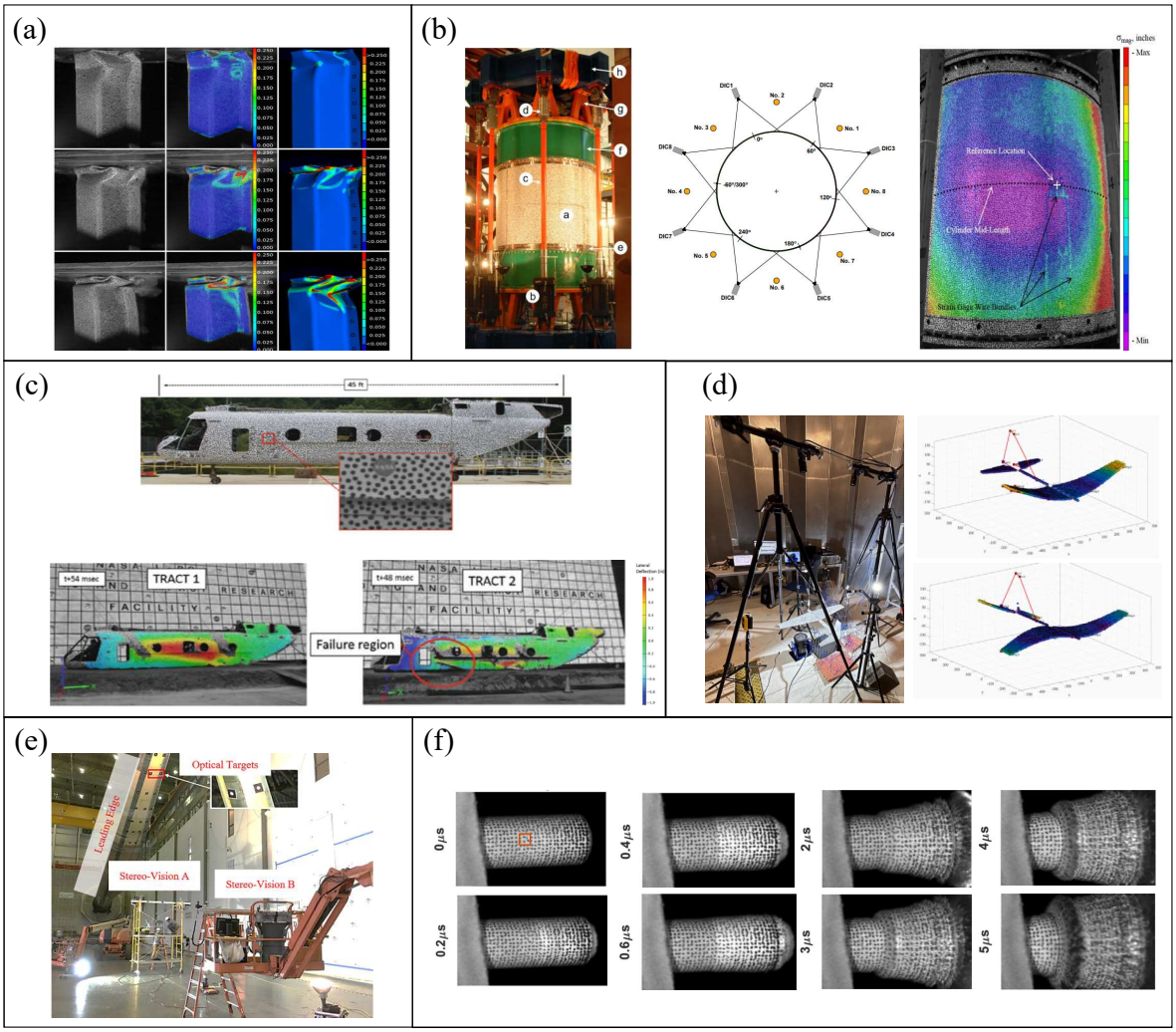

Figure 3.22 – Applications of DIC in impact and dynamic testing: (a) Comparison between, 3D digital image correlation, and FE simulation results [53]; (b) Shell Buckling Knockdown Factor Project (SBKF) [54]; (c) Deflection measurements of CH-46E "Sea Knight" airframes as part of the transport rotorcraft airframe crash testbed (TRACT) project random speckle pattern on the fuselage; and lateral deformation due to crash [55]; (d) Experimental Modal Analysis (EMA) setup and modal shapes of demo airplane [57]; (e) Experimental setup of modal analysis of a wind turbine blade [58]; and (f) DIC in an explosive event [59].

3.5.3 Structural Health Monitoring and Damage Assessment

DIC is also increasingly used in structural health monitoring (SHM) to assess the integrity of materials and structures over time. By comparing strain fields from DIC measurements taken at different stages of loading or during service, researchers can detect changes in the material behavior that indicate damage, such as crack propagation, delamination, or plastic deformation. DIC can be particularly useful in assessing structures subjected to cyclic loading, where it helps track the development of fatigue damage and

predict failure modes. The ability to measure strain over the entire surface of a structure allows for more comprehensive monitoring compared to traditional methods that only measure at specific points. Monitoring the structural health of infrastructure is essential for preventing catastrophic failure, enhancing its safety, and reducing repair costs and downtime.

These technic has been extensivelly applied in the construction fiel, to monitoring the complex structure such as bridges and towers [60, 61, 62, 63]. Where Reagan et al. [60], performed the feasibility of the use digital image correlation composed of UAV equipped with a 3D-DIC sensor package to be used for monitoring of bridges for unmanned aerial vehicle structural health monitoring of bridges. The authors conductes a laboratory tests and a long-term monitoring campaign on two in-service concrete bridges demonstrated the accuracy of this system in detecting structural changes as presented in Figure 3.23 (a), where is possible to note the bridge monitoring setup and the vertical crack monitored are full-field X-displacement extensometer locations and averaged virtual optical extensometers displacement noise floor results under various measurement conditions. From the results, was presented that this system is able to detect changes to the bridge geometry with an uncertainty on the order of 1025 m while improving accessibility. Also, analysing a reinforced concret beam as presented in Figure 3.23 (b), Mousa et al. [61] employed the DIC, where the total actual size and number of cracks could be identified, inside the speckled zone, from a single captured photograph before cracking emerged and another captured afterwards. This technique provides advantages in detecting cracks, which may develop in a non-contact manner. Furthermore, it offers valuable data about where crack propagation detectors can be attached and proffer precise calculations of cracks, including instances where crack edges are poorly defined.

The DIC technique has also been proposed for use in structural health monitoring of wind turbine blades. Wu et al. [64] developed a novel and cost-effective optical approach based on three-dimensional digital image correlation (3D-DIC) to monitor the condition of wind turbine blades, as illustrated in Figure 3.23 (c). Their fault detection strategy relied on evaluating the relative deformation of the blades during operation. To validate the proposed method, a 5 kW wind turbine with a 4 m diameter was tested using 3D-DIC. The results demonstrated that this technique provides an efficient and non-contact solution for real-time health monitoring of wind turbine blades. Chen et al. [65] investigated damage growth in a full-scale composite wind turbine blade under fatigue loading using Infrared (IR) thermography, Acoustic Emission (AE), and Digital Image Correlation (DIC). Since the focus of the present work is on DIC, only the results obtained from this technique are discussed here, where the DIC measurements enabled the monitoring of the trailing edge region of the blade during cyclic loading, revealing, for the first time, the occurrence of cyclic buckling associated with adhesive joint debonding. This observation highlights the importance of accounting for geometric and contact nonlinearities in fatigue damage

modeling of the trailing edge bondline.

This focus on composite integrity is also critical for general damage assessment. The DIC technique has thus been employed for damage assessment in repaired laminates. Kashfuddoja and Ramji [66] conducted an experimental investigation using Digital Image Correlation (DIC) to analyze the tensile behavior of adhesively bonded patch repairs in carbon/epoxy unidirectional composite laminates. The damaged panels were repaired with both single- and double-sided circular patches made from the same parent material. Using 3D-DIC, the authors successfully monitored damage initiation and propagation in the notched and repaired regions, as well as patch debonding. Additionally, a 3D finite element analysis was performed, and the numerically obtained strain fields showed good agreement with the experimental DIC measurements. Laurin et al. [67] conducted a study to determine the mechanical properties of composite materials using Digital Image Correlation (DIC). As shown in Figure 3.23 (d), the DIC measurements were qualitatively compared with the predicted matrix damage patterns (denoted as d2) on the upper 0° ply of $[0_2/90/0_2]$ perforated plates containing two or four holes. The comparison revealed that the proposed damage and failure model accurately predicted the initiation, location, orientation, and progression of splitting cracks up to final failure.

Building on these material assessment techniques, the aeronautical engineering field, Jamshed et al.[68] developed a deep learning-enhanced DIC framework (CMAD) for automated crack monitoring in aircraft structures. The model accurately detected crack initiation, localized crack tips, and predicted crack propagation with high precision achieving displacement field prediction with SSIM > 0.96 and crack length error < 0.1 mm. Compared to traditional DIC and strain-gauge methods, the proposed approach identified cracks earlier and provided more comprehensive full-field strain and displacement data.

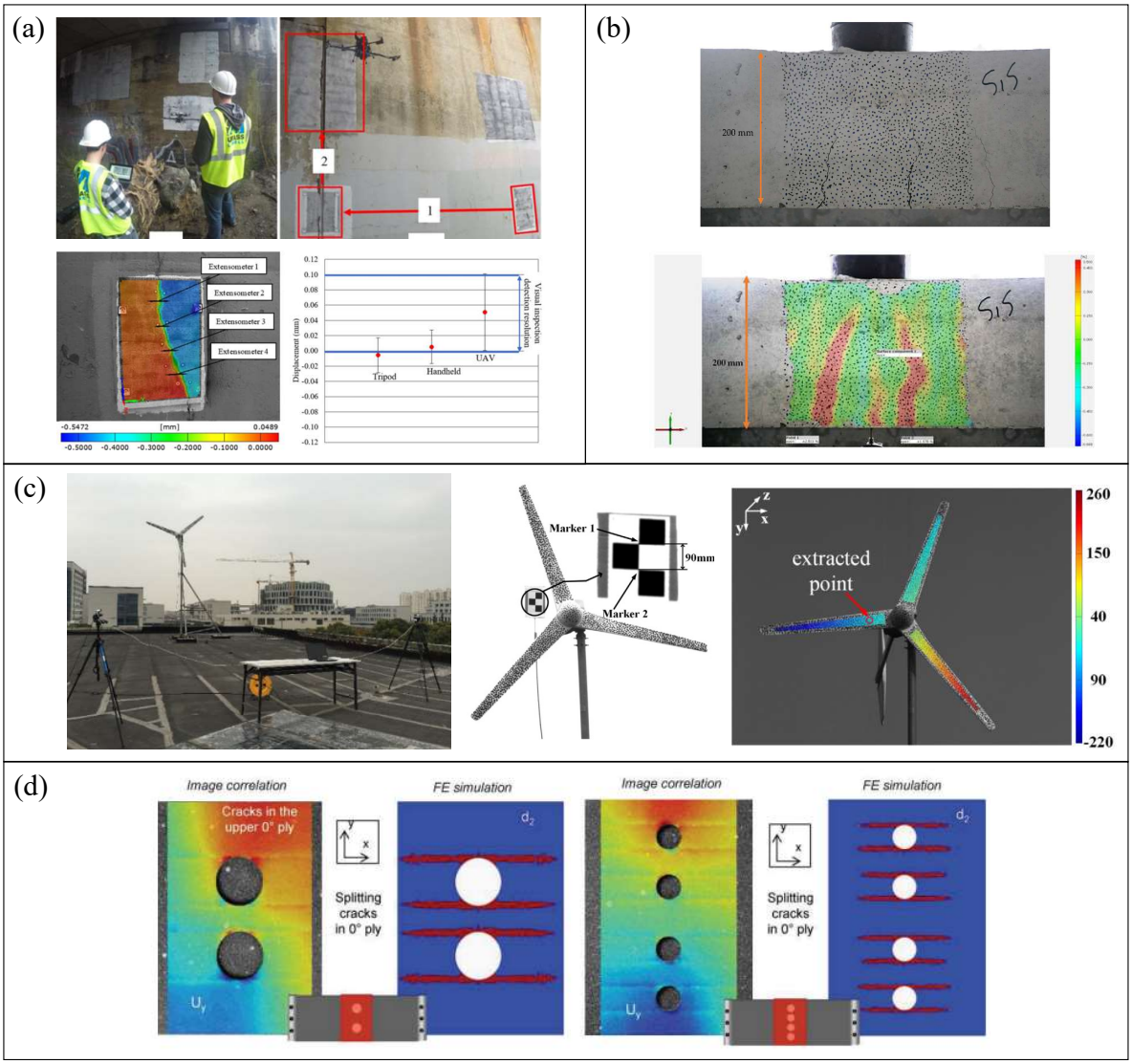

Figure 3.23 – Applications of DIC in structural health monitoring and damage assessment: (a) UAV-based inspection setup [60]; (b) DIC deformation map of a reinforced concrete beam [61]; (c) Full-field displacement of wind turbine blades [64]; and (d) Damage detection in composite plates [67].

3.5.4 Fatigue and Fracture Mechanics

DIC has proven to be an invaluable tool in fatigue and fracture mechanics, where it is used to measure strain localization and crack propagation during cyclic loading or fracture tests. By providing full-field strain data, DIC allows for a more detailed understanding of how cracks initiate and grow under loading conditions, which is crucial for improving material design and predicting failure. The technique has been applied in studies of fatigue crack growth, delamination in composites, and fracture toughness testing, where it can capture strain concentration near the crack tip and help evaluate the material's resistance to crack propagation.

Yusof and Withers [69] performed a real-time acquisition of fatigue crack images

monitoring crack-tip stress intensity variations within fatigue cycles of a pre-cracked aluminium 2024-T3 sample. The digital images of fatigue crack behaviour was acquired in real time at high cycle fatigue rates (77 Hz) using a high-speed camera at 1000 frames/s. According to the auhtors, the analyzing displacement fields of an aluminum CT specimen, accurate stress intensity factors (KI and KII) were obtained, showing good agreement with nominal ΔK and enabling in-situ identification of crack closure and growth under cyclic loading. Also analyzing the efects of fatigue in aluminium, Breitbarth et al. [70] evaluated the evolution of dislocation patterns inside the plastic zone introduced by fatigue in an aged aluminium alloy AA2024-T3 of the Figure 3.24 (a) present a study a strain map in the vicinity of the crack tip in the unloaded specimen after 30 load cycle which was used the commercial system ARAMIS 12M, GOM GmbH, where the regions selected for ECCI investigations are marked as P1 to P4. According to the authors findings, the DIC's results provided information about the distribution of plastic strain, which this strain was caused by mobile dislocations travelling through the material.

Analyzing fracture mechanics under fatigue conditions, the DIC methodology enables the evaluation of crack propagation. Stewart et al. [71] investigated the fatigue crack growth behavior of hot mix asphalt using digital image correlation. Their results demonstrated that the technique successfully captured crack propagation, crack-tip evolution, the fatigue process zone, and the surface strain distribution of the specimens. As illustrated in the Figure 3.24 (b), the crack length was measured and the von Mises strain contours were mapped over the specimen surface. Correlation loss in areas of large displacement indicated the location of the fatigue process zone. Using ImageJ, several points were plotted within this region, allowing the identification of primary, branching, and secondary cracks, all contributing to the overall crack length measurements. Also, with the goal to evaluate the crack growth, Blug et al. [72] A high-performance 2D DIC system combining a GPU and a CoaXPress 2.0 camera was developed to enable real-time strain-controlled testing and fatigue crack growth characterization under biaxial experiments as presented in Figure 3.24 (c). The method allowed simultaneous full-field displacement measurement and FEM comparison, simplifying experiments while providing detailed fracture mechanical data.

It is widely recognized that fatigue crack growth tends to decelerate following an overload, a phenomenon commonly attributed to plasticity-induced crack closure or near-tip residual stresses. In this context, Qiang et al. [73] investigated the evolution of crack-tip strain and the occurrence of crack closure during the overload phase of a propagating fatigue crack. The study employed a material with a low work-hardening coefficient, using in-situ SEM observations combined with digital image correlation to analyze the influence of overload on crack-tip strain behavior and closure mechanisms. As results presented in Figure 3.24 (d), the crack growth morphology during the overload process and the corresponding strain distribution obtained by DIC. Before the overload cycle, the fatigue crack

is located at a grain boundary; during overload, it crosses the boundary and branches, and after the cycle, these branched cracks extend further. The strain maps show clear variations near the crack tip, with changes in the plastic zone shape and size. Strain localization occurs mainly around the grain boundaries, suggesting potential sites for subsequent cracking under constant amplitude loading.

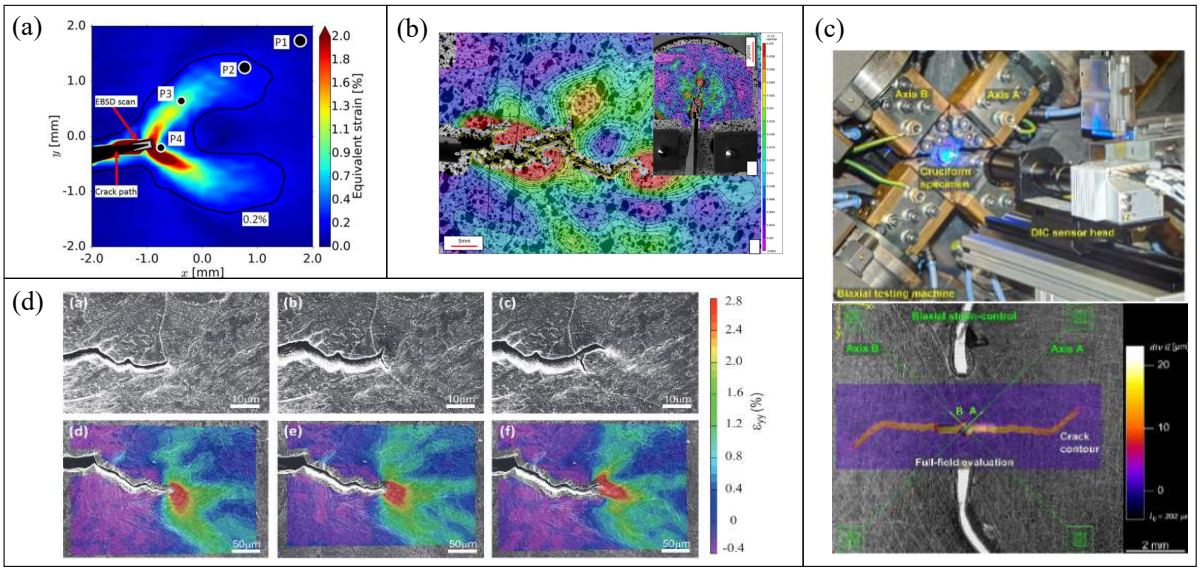

Figure 3.24 – Fatigue and fracture mechanics tests using DIC: (a) strain distribution near the crack tip after 30 load cycles [70]; (b) crack length and von Mises strain contours on the specimen surface [71]; (c) DIC setup with a biaxial testing machine and cruciform specimen [72]; and (d) crack growth morphology during overload [73].

As the studies presented demonstrate, the application of DIC in fracture and fatigue mechanics is important and have been used for complex analysis. Where these technique goes beyond simply measuring crack propagation, providing full-field data essential for determining fracture parameters, analyzing microscale phenomena such as dislocation accumulation in the plastic zone, and understanding complex mechanisms such as overload-induced crack closure. This ability to provide high-fidelity quantitative data, from the sample to the grain scale, under dynamic and high-speed conditions, present the DIC as an indispensable tool for model validation and fundamental understanding of damage mechanisms in materials.

3.5.5 Non-Destructive Testing (NDT)

As a non-contact measurement technique, DIC is often used in non-destructive testing (NDT) of materials and structures. It allows for the measurement of surface strains without altering or damaging the specimen, making it ideal for inspecting critical components in industries such as aerospace, automotive, and civil engineering. DIC can be used to detect hidden defects, such as voids, delaminations, or material heterogeneity, by

identifying areas of strain concentration that may indicate the presence of defects. This application is particularly beneficial for inspecting large or complex components that are difficult to assess using traditional NDT methods.

Expanding on this application, Malesa et al. [74] performed non-destructive testing on industrial structures using a multi-camera DIC system, proposing two spatial data merging strategies: one for cases with overlapping fields of view and another for distributed systems without overlap. The first was applied to the measurement of a metal plate, allowing the generation of displacement maps and the updating of numerical models of a real structure (Figure 3.25 (a)). The second, which used geodetic surveying to reference the DIC data to the global system, proved suitable for older industrial installations (Figure 3.25 (b)). In both cases, the results were used to validate and calibrate numerical models, aiding in failure analysis and structural evaluation.

Following a similar non-contact and field-deployable concept, Kadhaka et al. [75] proposed a non-contact, three-dimensional full-field DIC technique for nondestructive evaluation of wind turbine structures. This approach quantifies strains and loading conditions in operating turbines without affecting their functionality. The integration of UAVs allows for remote and periodic inspections as presented in Figure 3.25 (c). Indoor tests under controlled lighting were first performed to calibrate the DIC-UAV system, followed by outdoor measurements capturing the dynamic behavior of the blades. Comparison with strain gauge data showed strong agreement, confirming that the method provides reliable strain measurements in rotating structures.

Complementing these developments, vibration-based DIC has also been explored as an NDT tool for damage assessment. Seguel and Meruane [76] investigated the application of full-field vibration measurements in the debonding assessment of an aluminium honeycomb sandwich panel. The authors performed experimental data from an aluminium honeycomb panel containing different damage scenarios was acquired by a high-speed 3-D DIC system as presented in Figure 3.25 (d). The results showed that the high-speed 3D system can be used to successfully identify debonding in composite panels. Similarly, Sun et al. [77] proposed a baseline-free damage detection approach that combines three-dimensional Digital Image Correlation (3D DIC) with two-dimensional continuous wavelet transform (2D CWT) for identifying and characterizing damage in carbon fiber reinforced polymer (CFRP) composite plates containing artificial defects, such as notches and local cracks. The mode shapes of the damaged plates were extracted through singular value decomposition (SVD) of the frequency response function (FRF) matrix. The study showed that damage detection accuracy in vibration based DIC measurements is influenced by the size and type of defect, as smaller damages (such as local cracks) are more challenging to identify and that the optimal number and placement of measurement points are strongly dependent on the damage characteristics.

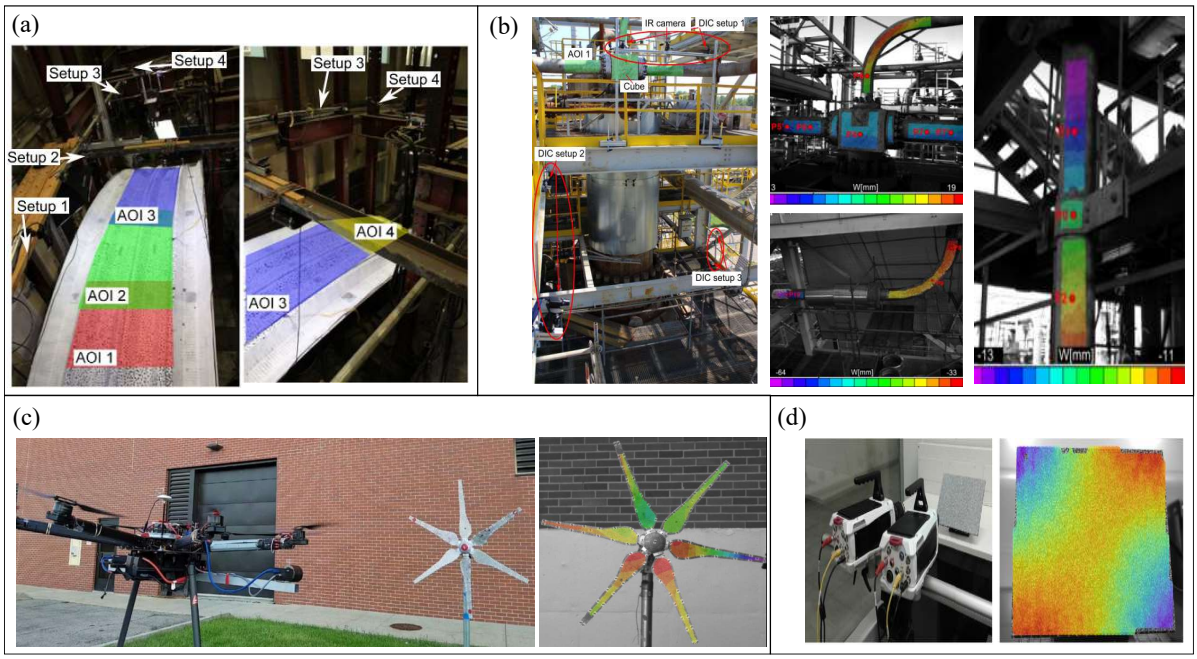

Figure 3.25 – Non-Destructive Testing using DIC: (a) Experimental setup showing metal plate configuration and camera arrangement [74]; (b) Monitoring of a nitrogen installation with three DIC setups and displacement maps referenced to the global coordinate system [74]; (c) UAV-based image acquisition and strain computation for wind turbine blades under outdoor conditions [75]; and (d) Vibration measurements obtained with a high-speed 3D-DIC system [76].

3.5.6 Military and Defense

The military and defense sector presents some of the most challenging scenarios for experimental mechanics, which involve blast loading, ballistic impacts, and high velocity events. As detailed previously (Section 3.5.2), these tests are characterized by high strain rates and rapid, large-scale deformations. Consequently, High-Speed (HS) and Ultra-High-Speed (UHS) DIC techniques are indispensable tools in this field, which enable the capture of transient phenomena that are impossible to measure with traditional sensors. Applications in this area focus on understanding the response of materials and structures to these extreme loads such as armors, helmets [78], projectiles, with the goal of validating high-fidelity numerical models and developing more effective protective systems.

The ability of military helmets to prevent ballistic threats' penetration capabilities is one of their most crucial features. Soldiers may sustain head injuries as a result of blunt trauma brought on by helmet back face deformation (BFD) [78]. Where, Hisley et al. [78] developed an experimental methodology to evaluate ballistic helmet performance using Digital Image Correlation (DIC) as presented in Figure 3.26 (a), which shown the noise floor measurement and the DIC deformation contours for 9 mm impact at helmet standoff and at maximum deformation. The technique enabled dynamic measurement of

helmet back face deformation (BFD), providing full-field displacement, velocity, and acceleration data. From DIC measurements, the authors derived an energy-based metric to assess the likelihood of blunt trauma injuries, such as skull fracture or concussion, and demonstrated that DIC can accurately capture BFD behavior and support quantitative helmet performance evaluation. To accurately model the transient mechanical behavior of a bulletproof helmet under ballistic impact, Zhouyu et al. [79] performed a numerical simulation of bullet penetration using a composite multiscale analysis approach. The stress–strain response of UHMWPE fiber bundles was experimentally obtained, and the homogenized material properties of the unidirectional UHMWPE layer were determined through progressive multiscale analysis. A 3D Hashin progressive damage model was developed to simulate the mechanical response of UHMWPE helmets. The numerical model was validated against 3D-DIC experimental data (Figure 3.26(b)), showing that the multiscale-derived parameters can accurately reproduce the deformation and failure behavior of the helmet under pistol bullet impact.

An essential piece of equipment in the military field is body armor, which protects soldiers and police officers from projectiles. Understanding its fundamental behavior is therefore crucial. Wang et al. [80] analyzed the dynamic behavior of SiC/UHMWPE ballistic plates under high-velocity projectile impact using a mirrored 3D-DIC high-speed imaging system. The method, validated with 7.62 mm API projectile tests, showed a maximum measurement error of 1.71% compared to side-view footage. Results revealed a maximum bulge of 36.2 mm at 1100 μ_s and an L-shaped strain distribution with a peak strain of 0.273 at the plate corners, demonstrating the system's accuracy and safety for high-speed deformation measurements. Also with goal to evaluate the body armor performance, Wen et al. [81] employed three-dimensional Digital Image Correlation (3D DIC) to capture the dynamic back-face deformation (BFD) of a ceramic/UHMWPE composite armor impacted by 7.63×39 mm rifle bullets as presented in Figure 3.26 (c). The technique enabled the measurement of BFD evolution over time, as well as the deformation velocity, acceleration, and surface profile along selected line sections on the rear face of the armor. Results showed that the maximum BFD reached 34.3 mm within approximately 1.2 ms, gradually decreasing to a residual deformation height of about 24 mm at an impact velocity of 675.4 m/s. The peak deformation velocity and acceleration were 129.9 m/s and 1.2910^6 m/s^2, respectively.

Therefore, DIC also proved effective for analysing projectile behaviour under firing conditions. Iqbal and Tiwari [82] investigated the influence of projectile geometry on the transient and post impact behavior of thin steel plates subjected to moderate-velocity impacts (100-250 m/s). By combining 3D-DIC experiments with numerical simulations, they demonstrated the capability of this approach to capture full-field deformation and validate numerical predictions (Figure 3.26 (d)). Their results showed that projectile shape, velocity, and target thickness significantly affect the perforation mechanism and out-of-

plane displacement, confirming 3D-DIC as a robust and reliable technique for dynamic impact analysis. Cheng et al. [83] evaluated the ballistic resistance of high-strength armor steel against ogive-nosed projectile impact. Where the study investigated the ballistic performance of two high-strength armor steels using 15 mm projectile perforation tests (164–428 m/s). High-speed 3D Digital Image Correlation (DIC) captured the out-of-plane displacement (OPD) and failure modes of the target plates as presented in Figure 3.26 (e). Experimental DIC data were used to validate numerical simulations via finite element (FE) and Smoothed Particle Galerkin (SPG) methods, showing that FE best reproduces failure patterns while SPG efficiently predicts projectile residual velocity.

Another relevant dynamic condition in military applications is blast loading. Yao et al. [84] conducted experimental and numerical investigations on the dynamic response of steel chambers subjected to internal explosions. In the experiments, the 3D-DIC technique was used to capture the full-field displacement and deformation process. Several chamber specimens of different sizes were tested, and corresponding numerical models were developed in ANSYS/LS-DYNA. The results revealed that the side plate response occurred in two stages: a global plastic deformation phase followed by central region oscillation. As shown in Figure 3.26 (f), DIC proved capable of accurately measuring structural responses under blast loading, and the numerical model effectively reproduced the observed dynamic behavior.

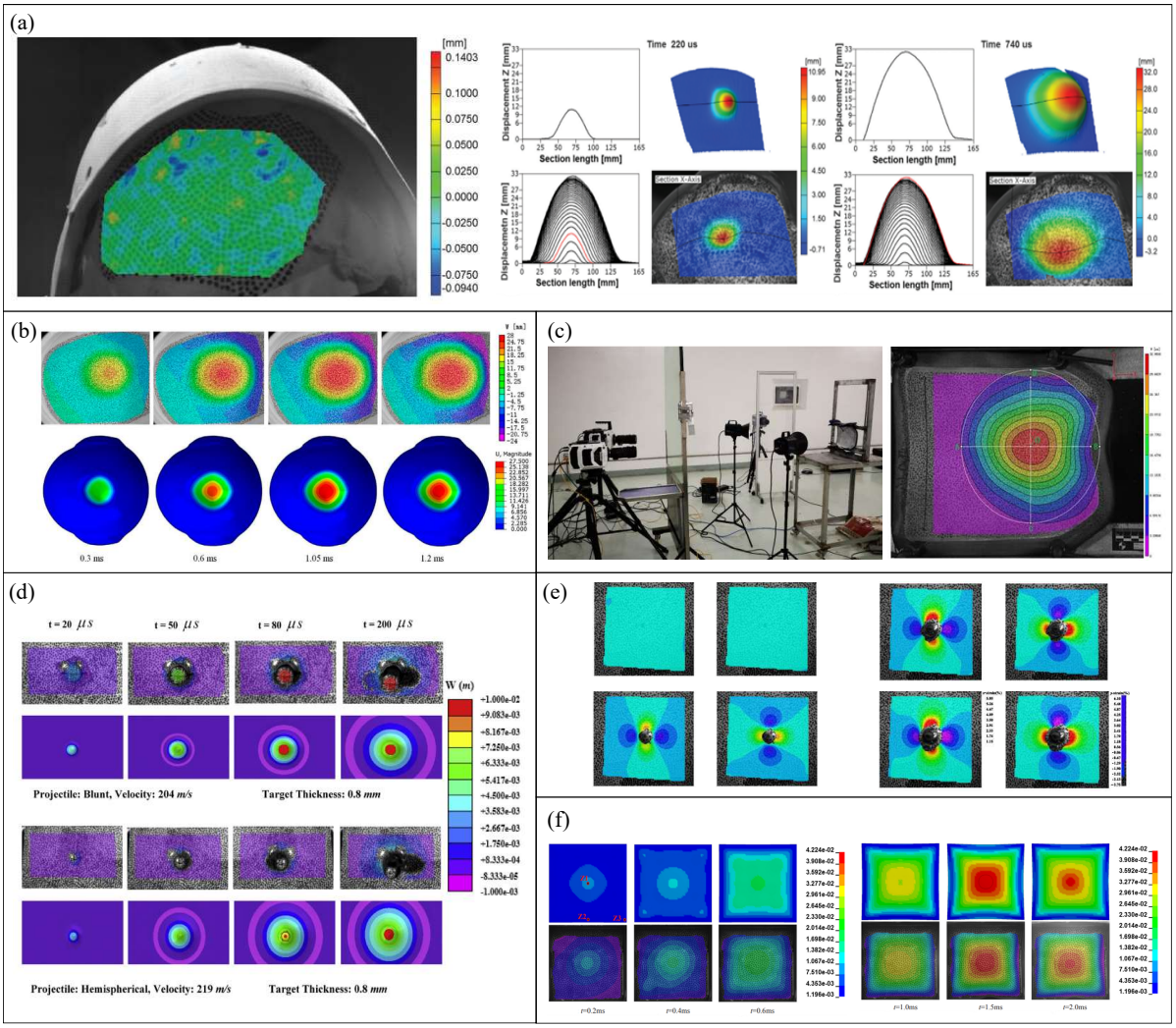

Figure 3.26 – Military applications using DIC: (a) Noise floor measurement and deformation contours for a 9 mm helmet impact [78]; (b) Comparison of helmet shape change between experiments and simulations of bulletproof helmet bulges [74]; (c) Body armor ballistic test DIC setup and schematic of line-slice positions [75]; (d) Comparison of experimental and numerical full-field out-of-plane transient displacement profiles of a 0.8 mm plate impacted by projectiles of different shapes [82]; (e) Horizontal and vertical strain fields at 0, 90.3, 194.4, and 333.3 μ_s during impact [82]; (f) Side plate dynamic blast deformation: comparison between numerical simulation and DIC measurements [84].

3.6 Emerging Trends, Future Directions, and Challenges of DIC

High-Speed Digital Image Correlation (HS-DIC) continues to evolve, driven by the increasing need for real-time, full-field strain measurements in dynamic experiments such as impact testing, crash simulations, and high-speed material testing. Recent advancements in camera technology, particularly faster frame rates and higher resolution sensors, have enabled HS-DIC to capture more complex material behaviors under extreme loading

conditions. These innovations have significantly improved the accuracy of the technique, allowing for the study of material deformation in unprecedented detail. Additionally, the integration of HS-DIC with other measurement systems, such as strain gauges, laser displacement sensors, and 3D scanning technologies, is becoming more common. This integration facilitates multi-faceted data collection, providing more comprehensive insights into the mechanical behavior of materials and structures.

One of the most promising emerging trends in HS-DIC is the development of real-time data processing and analysis. As high-speed imaging generates vast amounts of data, the computational demands for processing these images in a timely manner can be a significant bottleneck. However, advances in parallel computing and GPU-based processing are expected to overcome these limitations. These developments will allow for faster, more efficient data analysis, enabling real-time decision-making during dynamic experiments. The ability to analyze data on the fly is particularly important in high-speed experiments, where immediate feedback is crucial for adjusting testing conditions or identifying potential issues during testing. Additionally, the evolution of 3D HS-DIC systems represents a key step forward. Stereo DIC, which captures three-dimensional displacements, is being increasingly adapted for high-speed experiments. This capability offers more detailed strain measurements on complex geometries and multi-directional deformations, which are essential for understanding the behavior of materials and structures under dynamic loading conditions. The integration of 3D capabilities in high-speed setups opens up new possibilities for applications that require a comprehensive understanding of three-dimensional deformation, such as in aerospace and automotive testing.

Another exciting direction for the future of HS-DIC is the integration of machine learning (ML) and artificial intelligence (AI) into the data analysis pipeline. The combination of HS-DIC with AI-driven algorithms has the potential to automate the analysis process, identify patterns in the data, and optimize experimental conditions in real-time. Machine learning techniques could enhance the accuracy of DIC results by minimizing noise, correcting for experimental errors, and even predicting material behavior under different loading scenarios. Such advancements will streamline data processing, reducing the time required to extract meaningful insights and making HS-DIC more efficient and accessible to a wider range of researchers and engineers. Moreover, AI could also be leveraged for predictive modeling, allowing for more accurate forecasting of material behavior based on real-time experimental data. This integration could ultimately lead to smarter testing environments, where the system autonomously adjusts parameters to improve testing accuracy and reliability.

Additionally, the miniaturization of DIC technology is paving the way for wearable, portable systems that could revolutionize strain measurement in field settings. These wearable systems will enable real-time, in-situ monitoring of materials and structures in a variety of industries, including aerospace, civil engineering, and biomechanics. Portable

HS-DIC systems could be used to monitor structural health, track the behavior of materials under operational conditions, and assess the performance of components in real-time, improving safety and reducing the need for extensive post-testing analysis. This trend toward portability will significantly broaden the range of applications for DIC, extending beyond traditional laboratory settings and into real-world environments where dynamic, real-time monitoring is critical.

Despite the promising advancements, HS-DIC faces several challenges that need to be addressed to fully unlock its potential. One of the primary challenges is motion blur, which becomes more pronounced at higher frame rates. As the speed of deformation increases, motion blur can distort the captured images, making it difficult to accurately track the displacement of the speckle pattern. This issue is particularly problematic in high-velocity experiments, where deformation occurs in a fraction of a second. Additionally, the sensitivity of high-speed cameras to light is often reduced, requiring careful control of lighting conditions to maintain image quality. Strategies to improve camera sensors and optimize lighting setups are ongoing, but these issues remain significant barriers to achieving consistently accurate results.

Another challenge lies in the large volume of data generated by HS-DIC experiments, which presents substantial storage and computational hurdles. The high resolution and frame rates involved in high-speed testing can result in immense data sets that are difficult to process and analyze in real-time, especially in multi-camera configurations. To address this, researchers are exploring advanced data management techniques, such as in-situ data storage and distributed computing, to enhance the scalability of HS-DIC in large or complex setups. Furthermore, achieving and maintaining high-quality speckle patterns on complex or irregular surfaces remains a challenge. The speckle pattern may degrade or distort during testing, especially under dynamic loading conditions, leading to measurement errors. Ongoing research is focused on developing more robust speckle patterning techniques that are resistant to deformation and environmental influences, but this remains a challenging area for HS-DIC.

Lastly, the integration of HS-DIC with other experimental techniques, such as strain gauges, 3D scanning, and laser-based systems, presents its own set of challenges. The synchronization of data from multiple sources is a complex task, particularly when real-time data fusion is required. Researchers are working to improve calibration, synchronization, and data fusion methods to ensure that HS-DIC can be seamlessly integrated with other measurement systems. These efforts are crucial for advancing the field of experimental mechanics, as they will allow for more comprehensive data collection and analysis, enabling a deeper understanding of the material and structural behavior under dynamic loading conditions.

3.7 Final Remarks

In this chapter, we initially discussed the fundamental aspects of Digital Image Correlation (DIC), covering its principles, classifications, advantages, limitations, and practical implementation. The aim was to provide readers with a strong conceptual foundation for understanding High-Speed (HS) and Ultra High-Speed (UHS) DIC, as well as its integration with numerical methods such as Finite Element Analysis (FEA).

Within the high-speed context, we outlined the technological differences between HS and UHS systems, their typical applications, and the challenges associated with data acquisition, calibration, and image processing. We further explored the integration of DIC and FEA from two perspectives: (i) using DIC as a tool for experimental validation of numerical models, either through direct comparison or after signal processing, and (ii) utilizing displacement fields measured by DIC as inputs for inverse methods to identify material properties and boundary conditions.

This review also provided representative examples of DIC applications across various domains of experimental mechanics, from material characterization and impact testing to structural health monitoring, fracture studies, and nondestructive testing. In addition, we discussed the emerging trends and future directions of DIC, including advancements in real-time data processing, machine learning integration, and miniaturization for wearable systems. These innovations promise to enhance the versatility and applicability of DIC in dynamic testing environments, pushing the boundaries of what can be measured and analyzed in real time.

It is clear that DIC has a broad range of applications with increasing relevance in structural mechanics, driven by its non-contact nature, flexibility, and ability to provide rich, full-field data. As this technique continues to evolve, it is gaining traction in various fields, including aerospace, automotive engineering, and biomechanics, with new applications emerging regularly. However, the effective implementation of DIC, particularly in high-speed scenarios, requires a solid understanding of its theoretical foundations, careful calibration, and efficient data analysis methods. Researchers must navigate challenges such as motion blur, computational limitations, and the maintenance of high-quality speckle patterns under dynamic conditions.

Furthermore, the integration of DIC with numerical models, particularly FEA, remains a promising yet complex challenge. While DIC can significantly enhance model validation and refinement, achieving seamless integration between experimental measurements and computational simulations requires the development of clear and standardized protocols. This ongoing effort represents a frontier of great potential in experimental mechanics, enabling more accurate and reliable predictions of material and structural behavior under dynamic loading.

In conclusion, this chapter serves as a comprehensive guide for researchers look-

ing to implement DIC, particularly in high-speed testing or for numerical validation. It highlights both the opportunities and challenges associated with DIC and its integration with other experimental techniques. As the field progresses, the continued advancement of DIC systems, coupled with innovative approaches in data processing, AI integration, and real-time applications, will shape the future of experimental mechanics, driving new insights and discoveries across a wide array of scientific and engineering disciplines.

4 RATE-DEPENDENT CONSTITUTIVE FRAMEWORK FOR POLYMERS

4.1 Chapter Introduction

Thermoplastic polymers have been progressively employed in structural components, particularly in the aerospace, automotive, and military industries. These materials have been used both as matrices in composite systems and in situ, in the form of engineering polymers. This advancement is associated with the pursuit of mass reduction, increased geometric freedom, and functional gains, without significant compromise of structural performance [85, 86, 87].

In this context, during the design phase of such components, the use of numerical modeling tools becomes essential in order to ensure that the structure is able to adequately withstand the loads to which it will be subjected in service. One of the main inputs of numerical modeling is the material constitutive model, which is responsible for describing its mechanical response under different loading conditions [88, 89].

It is at this point that one of the main difficulties associated with the use of thermoplastic polymers arises. Unlike metallic materials and thermoset polymers, thermoplastics exhibit a more complex mechanical behavior [85, 90, 91]. In general, the typical stress–strain curve of these materials can be divided into five stages: linear viscoelastic deformation, nonlinear viscoelastic deformation, yielding, strain softening, and strain hardening [90, 92], as illustrated in Fig. 4.1.

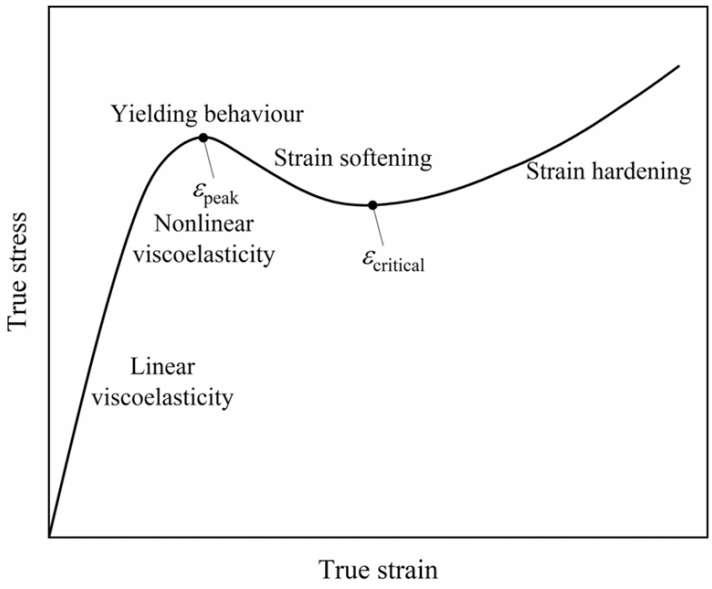

Figure 4.1 – Typical Stress–Strain Curve of Thermoplastic Polymers [93].

In addition, the stress–strain response of thermoplastic polymers is strongly influenced by factors such as strain rate, temperature, time, and pressure, which intensifies the nonlinear nature of their mechanical behavior [90]. This dependence makes the accurate constitutive representation a critical aspect for the reliability of numerical simulations, particularly under dynamic regimes.

Constitutive models capable of describing the mechanical behavior of these materials under different loading conditions can, in general, be classified into two groups: physically based constitutive models and phenomenological constitutive models. Physically based models aim to represent mechanisms associated with the polymer microstructure and composition, whereas phenomenological models are directly based on the response observed in experimental tests, adjusting parameters to reproduce the macroscopic behavior of the material. For engineering-oriented numerical simulations, phenomenological models are the most commonly employed, due to their simpler formulation and greater ease of implementation in commercial finite element codes [90].

Finite Element Analysis (FEA) applied to high strain-rate loading is commonly performed using explicit time integration (Explicit Dynamics), due to the strong nonlinearities typically involved, such as contact, large deformations, and material rate dependence [94, 95, 96]. In this context, LS-DYNA stands out as one of the most widely adopted solvers, offering a broad library of constitutive models, including strain-rate-sensitive phenomenological formulations. However, these models often require a significant number of input parameters and calibration datasets, which are not always available for engineering thermoplastics, especially when considering wide strain-rate ranges.

Among the available options, `*MAT_089` (*Plasticity Polymer*) is particularly attractive for polymers because it enables the direct use of tabulated stress–strain data and incorporates strain-rate effects with comparatively reduced calibration effort. This strategy has been adopted in prior studies, for instance in the identification of Cowper–Symonds parameters for ABS using LS-DYNA `*MAT_089` [97], and in high strain-rate investigations in which `MAT_89` is employed as a built-in reference model for polypropylene simulations [98]. Likewise, rate-dependent strengthening in semicrystalline polymers has been described using Cowper–Symonds-type relations, with the resulting parameters subsequently implemented in LS-DYNA [99].

Therefore, the present work aims to provide a practical set of input parameters for a strain-rate-sensitive constitutive description of polyoxymethylene (POM) based on literature data, including the material properties required by `*MAT_089` and the Cowper–Symonds coefficients C and P used to represent yield stress rate dependence. This approach enables a reproducible workflow for explicit simulations when experimental calibration is limited.

Polyoxymethylene (POM) was selected due to its excellent machinability and its high mechanical strength, wear resistance, and dimensional stability, which make it a

widely used material for functional polymer components and prototyping applications.

4.2 Constitutive Modeling of Polymers

Along with the advantages associated with the advent of thermoplastic polymers, particularly the possibility of obtaining materials with distinct behaviors through the control of processing conditions and, consequently, of the microstructure, the complexity of the constitutive models required to accurately predict their mechanical behavior has also increased significantly. This microstructural control involves parameters such as the degree of crystallinity, molecular orientation, and the incorporation of reinforcements, fillers, and additives, providing these materials with high versatility, but also imposing additional challenges from the standpoint of mechanical description.

Polymeric materials exhibit a significantly complex mechanical behavior due to their intrinsically viscoelastic nature, the mobility of molecular chains, and the coexistence of amorphous and crystalline phases, particularly in the case of semicrystalline polymers [85]. As a consequence of their microstructure, the mechanical response is influenced by variables such as strain rate, temperature, loading time, hydrostatic pressure, and loading history, which requires constitutive formulations capable of adequately capturing such dependencies [90, 93]. For instance, Fig. 4.2 illustrates the change in the stress–strain behavior of HDPE (high-density polyethylene) under different temperature and strain-rate conditions.

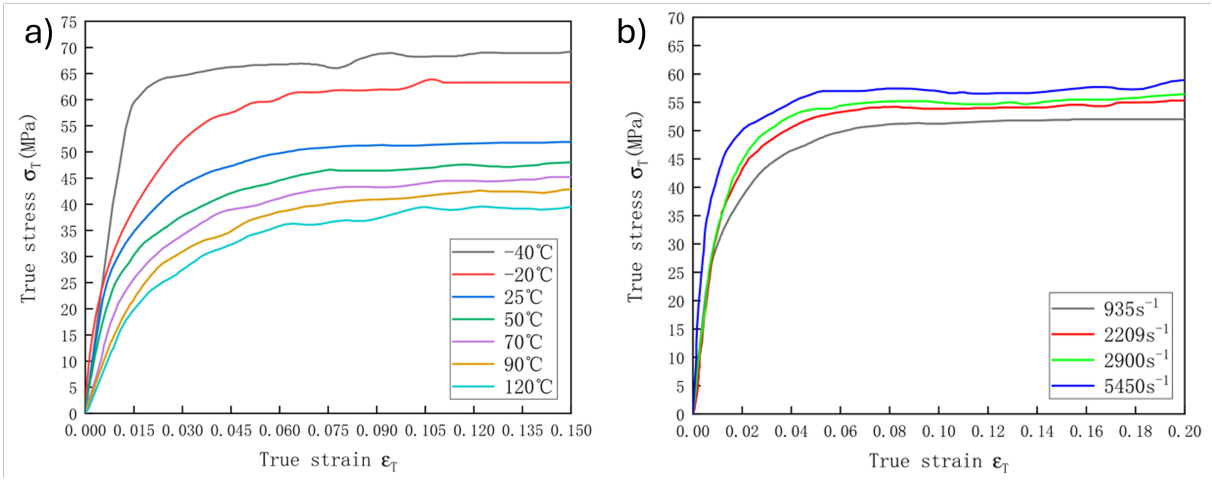

Figure 4.2 – Influence of temperature (a) and strain rate (b) on the mechanical behavior of HDPE [99].

In this context, the literature reports the proposal of a wide variety of models, each with specific features associated with the type of polymer and the physical phenomenon to be described. In general, such models can be classified into two broad categories: physically based models and phenomenological models [90], which will be addressed in the present work.

It should be noted, however, that this separation is not strictly watertight. There are physically based models that rely on experimental results to describe part of the material behavior, as well as phenomenological formulations that incorporate elements inspired by physical mechanisms. Therefore, the proposed division should be understood as a classification according to the predominance of one or the other approach, rather than as an absolute distinction.

4.2.1 Physical constitutive models

Physically based models describe the mechanical behavior of polymers in terms of their microstructural constitution and the physical mechanisms governing deformation. In this approach, the input parameters are directly associated with processing-induced features, linking the predicted response to molecular-chain behavior and microscopic interactions.

In particular, these models assume that factors such as the degree of crosslinking, molecular weight, and degree of crystallinity play a dominant role in defining the mechanical properties of the material [90]. Fig. 4.3 illustrates the micromechanical behavior of a semicrystalline polymer subjected to tensile loading. These models describe and predict the global mechanical behavior of the polymer based on the physical response of its microconstituents.

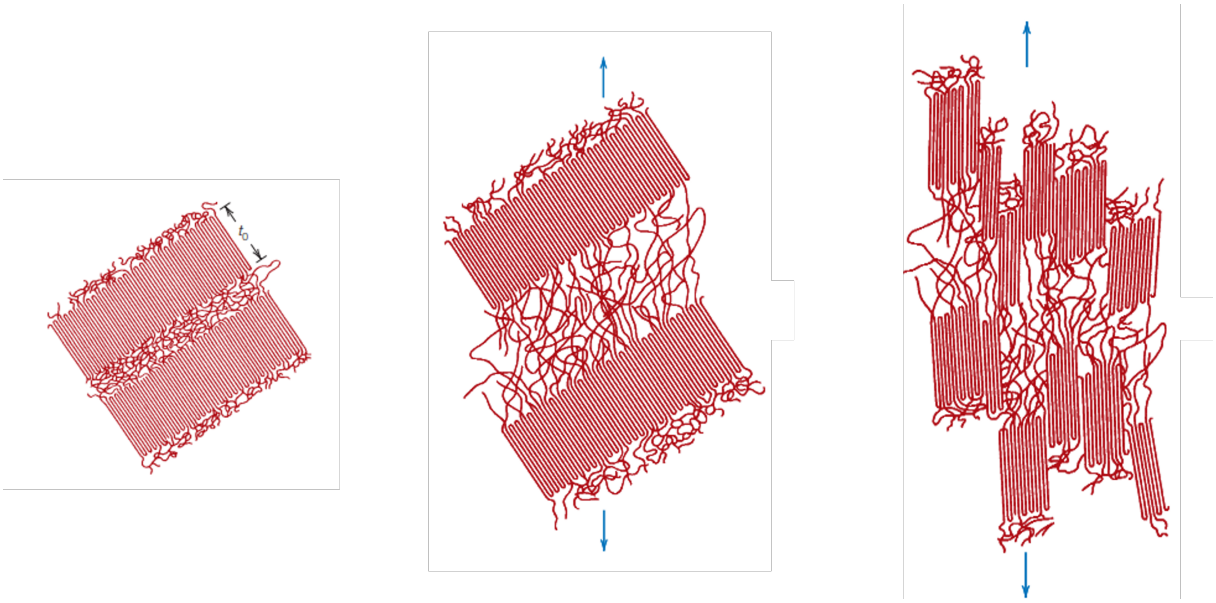

Figure 4.3 – Schematic representation of the behavior of the amorphous and crystalline phases of a semicrystalline polymer under tensile loading (adapted from [100]).

Despite their high scientific relevance, these models rely on an extensive set of experimental data for the proper identification of their parameters and require additional validation procedures. For this reason, they are particularly useful for understanding the

physical mechanisms underlying deformation and for the development of new polymers with tailored properties. However, their direct application in commercial finite element software is generally limited, since such platforms require constitutive formulations in formats compatible with the time-integration schemes and with the solver's stability and numerical-efficiency requirements.

Most studies addressing physically based constitutive models originate from the classical developments of Edwards and Vilgis, as well as of Haward and Thackray [90].

The model proposed by Edwards and Vilgis [101] belongs to the class of so-called rubber-like models and is based on the interpretation that, at small deformations, the dominant mechanism is the relative sliding of polymer chains, whereas, at large deformations, strain hardening is attributed to the inextensibility of these chains. Initially, this model was developed to describe the mechanical behavior of rubbers and was later extended and applied to amorphous glassy polymers and semicrystalline polymers.

The Haward and Thackray model [102] is composed of a Hookean spring, an Eyring-type dashpot, and a Langevin spring with a limiting network stretch, as schematically shown in Fig. 4.4. The Hookean spring represents the constant linear elastic modulus associated with the elastic deformation of the amorphous phase. The Eyring dashpot, in turn, describes the viscoplastic character of the material and is responsible for representing the macroscopic strain-rate-dependent yielding. Finally, the Langevin spring is associated with strain hardening at large deformations, resulting from the entropic limitation imposed by the inextensibility of polymer chains and by the progressive reorientation of the molecular network.

The work of Haward and Thackray served as the basis for several subsequent studies. Among them, the work of Boyce et al. [103] stands out, in which the BPA model was developed. In this model, a Langevin spring is arranged in parallel with a series assembly composed of a linear spring and a viscoplastic dashpot, as illustrated in Fig. 4.4. The formulation assumes that the deformation of an amorphous polymer can be described as a combination of mechanisms associated with intramolecular resistance to deformation and entropic resistance to deformation. The BPA model showed good agreement with experimental results for PMMA [90].

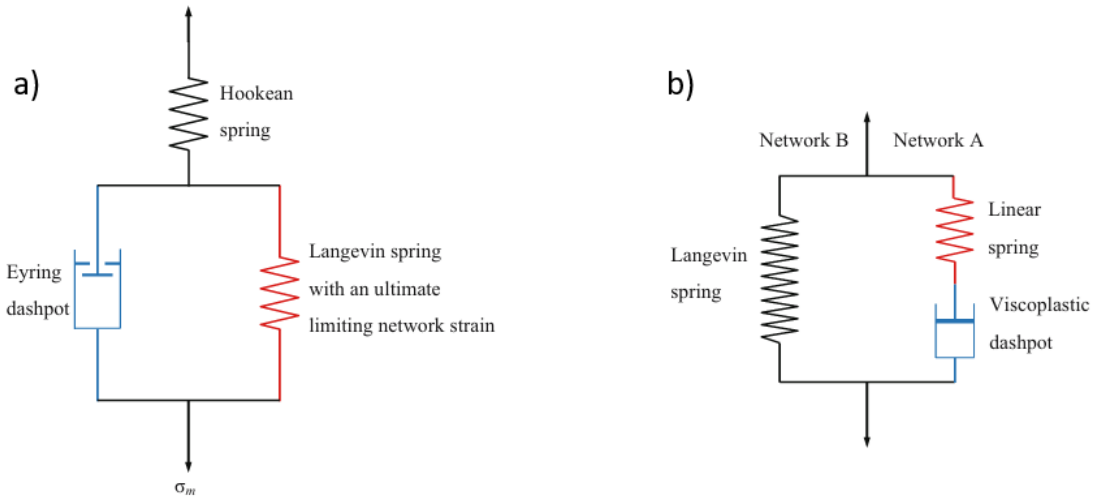

Figure 4.4 – Haward–Thackray model (a) and BPA model (b) (adapted from [90]).

4.2.2 Phenomenological constitutive models

Phenomenological constitutive models seek a mathematical description of the mechanical behavior of polymers based on the imposed loading conditions. These approaches are widely used in engineering applications, since experimental data can be directly used to fit a constitutive law capable of representing the observed behavior. The central objective of these models is to provide a mathematical formulation that describes the material response based on experimental data, allowing the interpolation or extrapolation of behavior under intermediate conditions.

Although the focus of these models is predominantly mathematical, it should be noted that, in many cases, the starting point is the underlying physics of the problem [90]. In general, an initial representation of the global material behavior is proposed based on known physical mechanisms and is subsequently refined and calibrated using experimental data in order to improve its predictive capability.

An important aspect to consider is that mechanical data reported in the literature for the same polymer may vary significantly depending on processing conditions. Parameters such as degree of crystallinity, spherulitic morphology, and molecular orientation can substantially influence the mechanical response. Therefore, caution must be exercised when developing or calibrating phenomenological constitutive models.

Among the most widely used phenomenological models, elastoplastic formulations stand out, such as the Johnson–Cook model, which was originally proposed to describe the behavior of metals subjected to high strain rates and elevated temperatures. Subsequently, several authors have observed that its formulation can also be employed, with appropriate modifications, to describe the behavior of semicrystalline polymers, particularly under dynamic loading regimes [104, 105].

The Johnson–Cook model is described by the following formulation:

$$\sigma = (A + B(\varepsilon_p)^n)\left(1 + C\ln\frac{\dot{\varepsilon_p}}{\dot{\varepsilon_0}}\right)\left[1 - \left(\frac{T - T_{\text{ref}}}{T_m - T_{\text{ref}}}\right)^m\right] \tag{4.1}$$

where σ represents the equivalent stress, ε_p the equivalent plastic strain, $\dot{\varepsilon}_p$ the plastic strain rate, $\dot{\varepsilon_0}$ the reference strain rate, T the current temperature, T_m the melting temperature, and Tref the reference temperature.

This model is widely used as a constitutive law in engineering applications, mainly due to its simplicity and the requirement of only five material parameters for its calibration (A, B, n, C, and m), which makes it particularly attractive for simulations involving high strain rates and thermal variations.

Although many of these models adequately represent the viscous, elastic, and plastic behaviors of polymers, they exhibit limitations in describing damage processes and crack nucleation. As a result, several authors have explicitly incorporated damage mechanisms into constitutive formulations. In this context, approaches based on Perzyna-type viscoplastic formulations stand out, in which the nonlinear stress–strain response is described from a non-associated viscoplastic potential, also allowing the capture of volumetric changes under tension and compression [90, 106].

Specifically, when one seeks to capture the dependence of the mechanical behavior on strain rate, a widely used strategy consists in scaling the yield stress through the Cowper–Symonds relation, as illustrated in Fig. 4.5. It can be observed that the yield stress increases as the strain rate increases. The black, blue, and orange curves represent progressively higher strain rates, respectively.

The scaling of the yield stress follows the following formulation:

$$\sigma = \sigma_0\left[1 + \left(\frac{\dot{\varepsilon}}{C}\right)^{1/p}\right], \tag{4.2}$$

where σ_0 represents the reference (quasi-static) yield stress, $\dot{\varepsilon}$ is the strain rate, and C and p are the Cowper–Symonds model parameters, determined experimentally [107].

This approach does not constitute a constitutive model in the strict sense, but rather an empirical correction to the yield stress, it is particularly valuable in impact applications, such as crashworthiness, in which the primary interest lies in the material response under high strain rates.

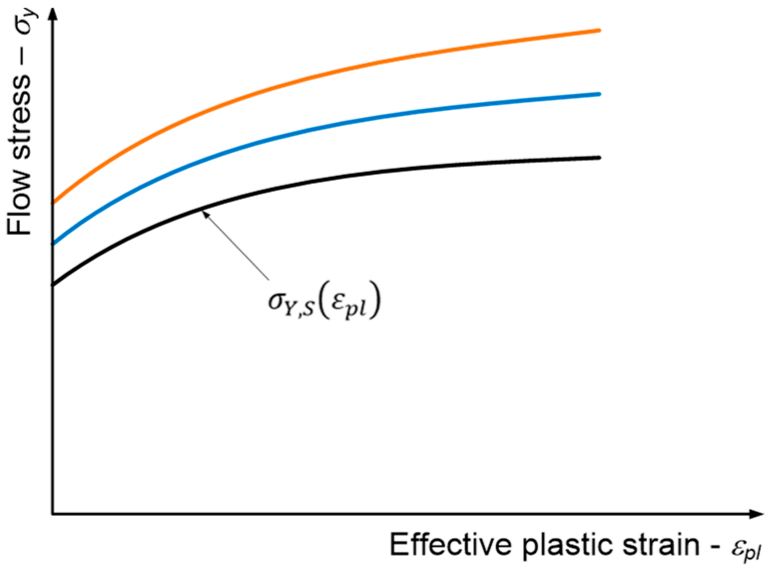

Figure 4.5 – Yield stress scaling according to the Cowper–Symonds relation [107].

4.3 Rate-Dependent Constitutive Modeling of Polymers for Computational Applications

Finite Element Analysis (FEA) constitutes the main procedure for the numerical simulation of the mechanical behavior of structural components. In physical problems characterized by high loading rates, large deformations, and complex contact interactions, the adoption of Explicit Dynamics time integration schemes becomes particularly relevant [94, 95, 96].

The LS-DYNA software stands out as one of the main tools employed in Explicit Dynamics analyses. The platform provides an extensive library of constitutive material models, allowing the adoption of different levels of complexity in the description of the mechanical behavior of the analyzed component.

The models available in the software are mostly phenomenological in nature. It is the user's responsibility to provide the parameters required for the calibration of the selected constitutive model. In events characterized by high strain rates, in which the polymer response exhibits a strong dependence on the loading velocity, it becomes essential to adopt a formulation capable of capturing this sensitivity, as well as to use appropriate experimental data for its proper calibration.

Table 4.1 presents the main LS-DYNA constitutive models (MAT) applicable to the modeling of polymers with strain-rate-sensitive behavior [88]. These models incorporate strain-rate dependency effects through different formulations, such as Cowper–Symonds-type relations, Johnson–Cook formulations, stress–strain curves defined for distinct strain-rate levels, or tabulated data explicitly describing the influence of strain rate on the yield stress.

Table 4.1 – Main constitutive material models available in LS-DYNA that incorporate strain-rate effects in polymers (adapted from Kolling et al. [88]).

MAT	Keyword	Strain-rate dependency input	Main constitutive formulation
3	MAT_PLASTIC_KINEMATIC	CS	An elastoplastic model with isotropic/kinematic hardening and optional yield stress scaling via the Cowper–Symonds law $\sigma_y = \sigma_0 \left[1 + \left(\frac{\dot{\varepsilon}}{C}\right)^{1/p}\right]$
12	MAT_ISOTROPIC_ELASTIC_PLASTIC	CS	A low-cost isotropic plasticity model for 3D solids that employs a non-iterative one-step radial return scheme for plane-stress shells, being the only LS-DYNA model for plane stress that does not default to an iterative approach.
15	MAT_JOHNSON_COOK	JC	Johnson–Cook viscoplastic model with multiplicative decomposition of strain, strain-rate and temperature effects: $\sigma = (A + B\varepsilon^n)\,[1 + C\ln(\dot{\varepsilon}^*)]\,[1 - (T^*)^m]$
18	MAT_POWER_LAW_PLASTICITY	CS	Rate-sensitive power-law plasticity combined with Cowper–Symonds dynamic amplification of flow stress
19	MAT_STRAIN_RATE_DEPENDENT_PLASTICITY	Load curves	Viscoplastic formulation defined by tabulated effective stress as a function of effective strain and strain rate
24	MAT_PIECEWISE_LINEAR_PLASTICITY	CS, tabulated	Elasto-plastic material; strain-rate dependence introduced via Cowper–Symonds scaling or tabulated stress–strain curves
81	MAT_PLASTICITY_WITH_DAMAGE	CS, tabulated	An elasto visco-plastic material with continuum damage mechanics; rate effects via Cowper–Symonds or tabulated curves
89	MAT_PLASTIC_POLYMER	CS, tabulated	An elasto-plastic material with an arbitrary stress as a function of strain curve and arbitrary strain rate dependency can be defined
98	MAT_SIMPLIFIED_JOHNSON_COOK	JC	Reduced Johnson–Cook formulation neglecting thermal softening, retaining strain and strain-rate dependence
105	MAT_DAMAGE_2 (VISCO-PLASTIC)	Perzyna	Perzyna-type viscoplastic overstress model: $\dot{\varepsilon}^p \propto \left\langle \frac{f(\sigma)}{\sigma_0} \right\rangle^m$
112	MAT_FINITE_ELASTIC_STRAIN_PLASTICITY	CS, tabulated	An elasto-plastic model with arbitrary stress–strain behavior, strain-rate-dependent yielding, and large-strain elasticity
123	MAT_MODIFIED_PIECEWISE_LINEAR_PLASTICITY	Load curve	Elasto-plastic material supporting an arbitrary stress as a function of strain curve as well as arbitrary strain rate dependency
187	MAT_SAMP_1	Load curve	Semi-analytical polymer model combining nonlinear elasticity and viscoplastic flow; rate effects defined by loaded curves

Legend: CS: Cowper–Symonds-type rate-scaling formulation; JC: Johnson–Cook constitutive model; Load curve: load-curve-based constitutive definition of effective stress; Tabulated: stress–strain curves assigned to discrete strain-rate levels; Perzyna: Perzyna-type viscoplastic overstress formulation.

Among the constitutive models most commonly employed for polymer modeling in the context of explicit simulations using LS-DYNA, the models MAT_024 (MAT_PIECEWISE_LINEAR_PLASTICITY), MAT_124 (MAT_PLASTICITY_COMPRESSION_TENSION), and MAT_187 (MAT_SAMP_1) stand out [87].

The MAT_024 model represents the standard formulation for crashworthiness applications and transient events. It is based on a phenomenological elasto-viscoplastic approach grounded in J2 plasticity theory, with a von Mises-type yield surface. The MAT_081, `MAT_089`, and MAT_123 models can be interpreted as extensions or variations of this basic formulation, incorporating different data input strategies and additional treatments.

The MAT_124 model also belongs to the elasto-viscoplastic class; however, it allows for the distinction between tensile and compressive mechanical behaviors by defining separate yield surfaces for each loading regime.

Finally, the MAT_187 model, originally proposed by Kolling et al. [88], presents a more general formulation, in which the yield surface is defined directly from stress–strain curves obtained under different loading states, such as tension, compression, shear, and biaxial tension. This enables a more realistic representation, in which the deformation response depends on the loading mode.

In the present work, the constitutive model `MAT_089` (Plasticity Polymer) is adopted. This model can be understood as an extension of MAT_024, but specifically formulated to describe the mechanical behavior of polymeric materials. Unlike classical models typically employed for metals, in which the elastic and plastic contributions to the response are clearly distinguishable, `MAT_089` is suitable for applications in which these regions cannot be easily separated, a common characteristic of many polymers [94]. Owing to this suitability, this model has been employed in several studies, such as those by Zhang et al. [99], Zhang et al. [98], and Marangoni et al. [97].

4.4 Constitutive Framework and Parameter Identification from Literature Data

In the development of new polymeric products, the laboratory conditions, time, or resources required to perform all the mechanical tests needed to calibrate more sophisticated constitutive models, such as SAMP-1, are not always available. In such cases, the use of the LS-DYNA `MAT_089` model becomes particularly attractive for explicit analyses of strain-rate-sensitive phenomena, since it requires only a limited set of input data to account for strain-rate effects, namely the true stress-strain curve, the elastic modulus E, Poisson's ratio ν, the density ρ, and the Cowper-Symonds parameters C and P.

The elastic parameters (E, ν) and the density (ρ) can be obtained directly from material datasheets. The true stress–strain curve can be constructed from data available

in the literature or provided by manufacturers. The parameters C and P, which govern the strain-rate sensitivity of yielding, will be identified in the present work based on experimental data available in the literature for POM, particularly those reported by Raisch (2010) [108], who provides yield stress values for different strain-rate regimes.

4.4.1 Extraction of POM data and identification of the Cowper-Symonds parameters C and P

The empirical Cowper-Symonds law describes the scaling of the yield stress as a function of increasing strain rate. In this formulation, the dynamic yield stress, $\sigma_y(\dot{\varepsilon})$, is expressed as a function of the strain rate based on a quasi-static reference value, σ_{y0}. The parameters C and P are material constants that control the sensitivity of the mechanical response to rate effects [109], according to:

$$\sigma_y(\dot{\varepsilon}) = \sigma_{y0}\left[1 + \left(\frac{\dot{\varepsilon}}{C}\right)^{1/P}\right]. \tag{4.3}$$

For the experimental identification of the parameters C and P, the Cowper–Symonds expression can be conveniently rewritten so as to assume a linear form on a logarithmic scale, which allows their determination through a simple linear fitting procedure:

$$\ln\left(\frac{\sigma_y}{\sigma_{y0}} - 1\right) = \frac{1}{P}\ln(\dot{\varepsilon}) - \frac{1}{P}\ln(C). \tag{4.4}$$

The Eq. (4.4) corresponds to the linearized form of the Cowper–Symonds relation. By comparing it with the general equation of a straight line,

$$y = ax + b, \tag{4.5}$$

it follows that

$$\underbrace{\ln\left(\frac{\sigma_y}{\sigma_{y0}} - 1\right)}_{y} = \underbrace{\frac{1}{P}}_{a}\underbrace{\ln(\dot{\varepsilon})}_{x} - \underbrace{\frac{1}{P}\ln(C)}_{b}. \tag{4.6}$$

The slope of the straight line provides:

$$a = \frac{1}{P} \quad \Rightarrow \quad P = \frac{1}{a}, \tag{4.7}$$

while the intercept allows the calculation of:

$$b = -\frac{1}{P}\ln(C) \quad \Rightarrow \quad C = \exp(-bP). \tag{4.8}$$

In Table 4.2, the yield stress data reported by Raisch (2010) [108] are presented. The quasi-static yield stress is taken as the value corresponding to a strain rate of 0.001 s^{-1} (σ_{y0} = 66.1 MPa). After the linear fitting procedure, a coefficient of determination of $R^2 = 0.936$ is obtained, along with the values $C = 1.29 \times 10^4$ s^{-1} and $P = 5.09$.

Table 4.2 – Yield stress data of POM at different strain rates (23 °C) (adapted from [108]).

$\dot{\varepsilon}$ (s^{-1})	σ_y (MPa)
0.001	66.1
0.01	69.5
0.1	73.4
1	78.4
10	84.3
100	86.8

4.4.2 Identification of POM parameters and construction of the true stress–strain curve

The elastic and physical parameters of POM, namely $E = 2.9$ GPa, $\nu = 0.37$, and $\rho = 1420$ kg/m^3, were obtained directly from the technical datasheets provided by the material manufacturers [110].

The quasi-static stress–strain curve required for the use of `MAT_089` must be expressed in terms of true measures. However, the data reported by Raisch [108], shown in Fig. 4.6, are originally provided in the form of engineering quantities, which requires their conversion to true measures prior to implementation in the constitutive model.

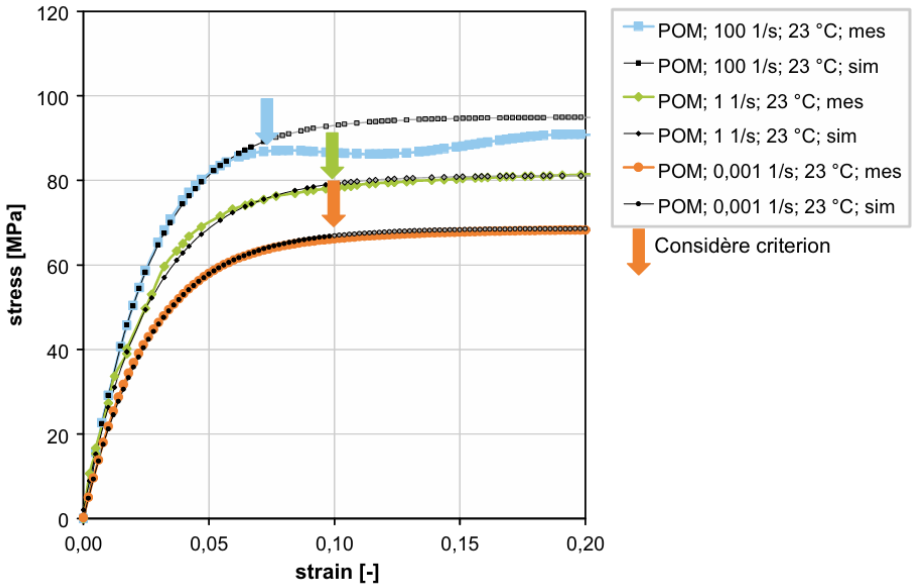

Figure 4.6 – Theoretical and experimental engineering stress–strain curves of POM for different strain rates at 23 °C[108].

With these considerations, the curve corresponding to a strain rate of 0.001 s^{-1}, adopted as the quasi-static reference, is converted to true measures by means of the standard relations between engineering and true quantities:

$$\sigma_{\text{true}} = \sigma_{\text{eng}} \left(1 + \varepsilon_{\text{eng}}\right), \tag{4.9}$$

$$\varepsilon_{\text{true}} = \ln\left(1 + \varepsilon_{\text{eng}}\right). \tag{4.10}$$

From these transformations, the true stress-strain curve of POM tested at a temperature of 23 °C and at a strain rate of 0.001 s^{-1} is obtained. The original engineering curve and the corresponding true curve are presented below. The resulting true stress-true strain pairs, to be used as input in the constitutive model, are listed in Table 4.3.

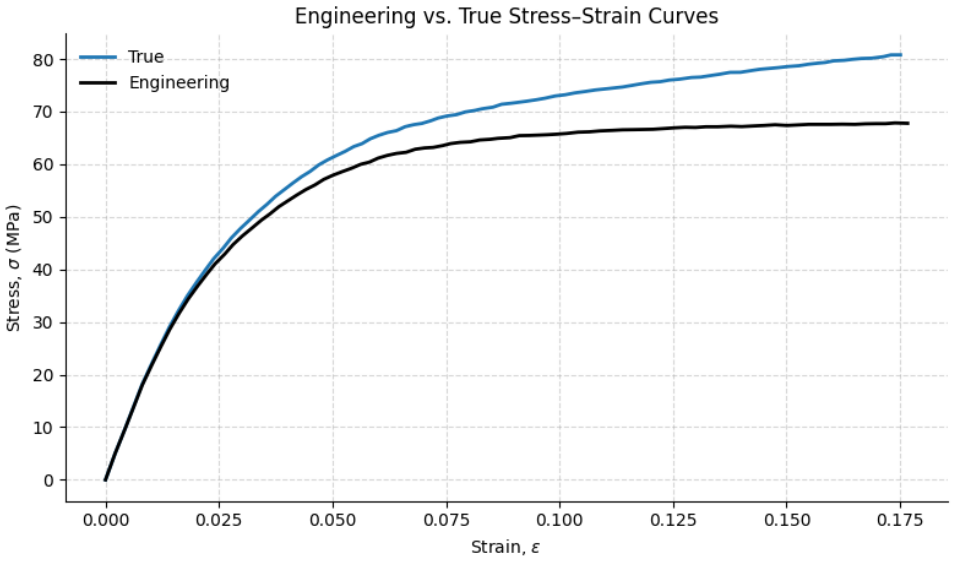

Figure 4.7 – Engineering stress data extracted from Raisch (2010) [108] and converted to true stress for implementation in the `MAT_089` material model.

Table 4.3 – Selected true stress–true strain pairs for `MAT_089` input.

True strain ε_{true} (-)	True stress σ_{true} (MPa)
0.00000	0.0000
0.01215	25.6618
0.02383	42.0378
0.03745	53.8951
0.04889	60.8186
0.06213	66.0337
0.07324	68.7759
0.08722	71.4004
0.09901	72.9708
0.11206	74.5080
0.12654	76.1816
0.13984	77.4796
0.15476	79.0069
0.16653	80.1052
0.18067	81.3698

The Table 4.4 summarizes the final set of constitutive parameters adopted for modeling the mechanical behavior of POM in LS-DYNA using the `MAT_089` model. The elastic and physical parameters were extracted directly from material datasheets, whereas the Cowper-Symonds coefficients C and P were identified from experimental data available in the literature.

The adopted strategy allows for a consistent representation of the strain-rate sensitivity of the yield stress while keeping a reduced number of parameters and ensuring numerical stability in explicit simulations. The true stress-strain curve used as model input corresponds to the quasi-static condition of 0.001 s^{-1} and serves as the reference for the dynamic scaling of yielding. It is emphasized that thermal effects, as well as damage and failure mechanisms, were not considered in the present work, since the focus lies on describing the strain-rate-dependent behavior under constant temperature.

Table 4.4 – Summary of constitutive parameters for polyoxymethylene (POM) implemented in LS-DYNA using the `MAT_089` (Plasticity Polymer) model.

Parameter	**Symbol / LS-DYNA input**	**Value**
Density	ρ	1420 kg/m^3
Young's modulus	E	2.9 GPa
Poisson's ratio	ν	0.37
Reference strain rate	$\dot{\varepsilon}_0$	0.001 s^{-1}
Reference yield stress	σ_{y0}	66.1 MPa
Cowper–Symonds parameter	C	1.29×10^4 s^{-1}
Cowper–Symonds exponent	P	5.09
Stress–strain input	$\sigma_{\text{true}}(\varepsilon_{\text{true}})$	Tabulated (Table 4.3)
Temperature effects	–	Not considered (isothermal, 23 °C)
Damage / failure	–	Not included

4.5 Final Remarks

The present work highlighted the relevance of constitutive modeling of thermoplastic polymeric materials in the context of contemporary engineering, particularly for applications in which these materials are subjected to high strain rates. Initially, a literature review was conducted, in which the main classes of constitutive models were discussed, distinguishing between physically based approaches and phenomenological formulations, while emphasizing the importance of the latter for finite element simulations, especially in explicit dynamic regimes.

It was shown that, in applications involving high strain rates, the proper representation of the strain-rate dependence of the mechanical response is an essential aspect for obtaining physically consistent results. In this context, constitutive models capable of adequately capturing this effect become indispensable.

As the main contribution, this work selected, analyzed, and implemented an appropriate constitutive model for describing the behavior of POM under high strain rates and constant temperature, based on the `MAT_089` formulation. The proposed methodology enables the identification of model parameters from data available in the literature, without the need for extensive and costly experimental campaigns. From the definition of the Cowper-Symonds parameters, it was possible to construct a complete phenomenological framework compatible with explicit dynamic simulations.

The developed approach thus establishes a reliable, systematic, and reproducible procedure for the calibration and application of strain-rate-dependent models in numerical analyses. Although exemplified for POM, the methodology is directly extensible to other semicrystalline thermoplastic polymers with similar characteristics.

As future perspectives, the incorporation of thermal effects, the consideration of damage and fracture mechanisms, as well as the direct experimental validation of the identified parameters, are highlighted. These extensions may further enhance the applicability of the proposed framework to real engineering problems.

5 EXPLICIT FINITE ELEMENT MODELING AND DIC-BASED VALIDATION

5.1 Chapter Introduction

The adoption of new materials in firearm components has become an established trend, particularly aimed at reducing mass and improving ergonomics without compromising functionality. In the case under study, this applies to the chassis of a bolt-action rifle (sniper rifle), whose architecture favors the use of polymeric or composite materials.

However, such ergonomic gains often imply the use of materials with elastic modulus and mechanical strength lower than those of the metals traditionally employed. Ashby-type material selection charts plotting density against elastic modulus clearly illustrate this intrinsic limitation: lightweight materials typically occupy regions of lower specific stiffness when compared with the alloy steels used in the firing mechanism and in the bolt–barrel assembly, as shown in Fig. 5.1.

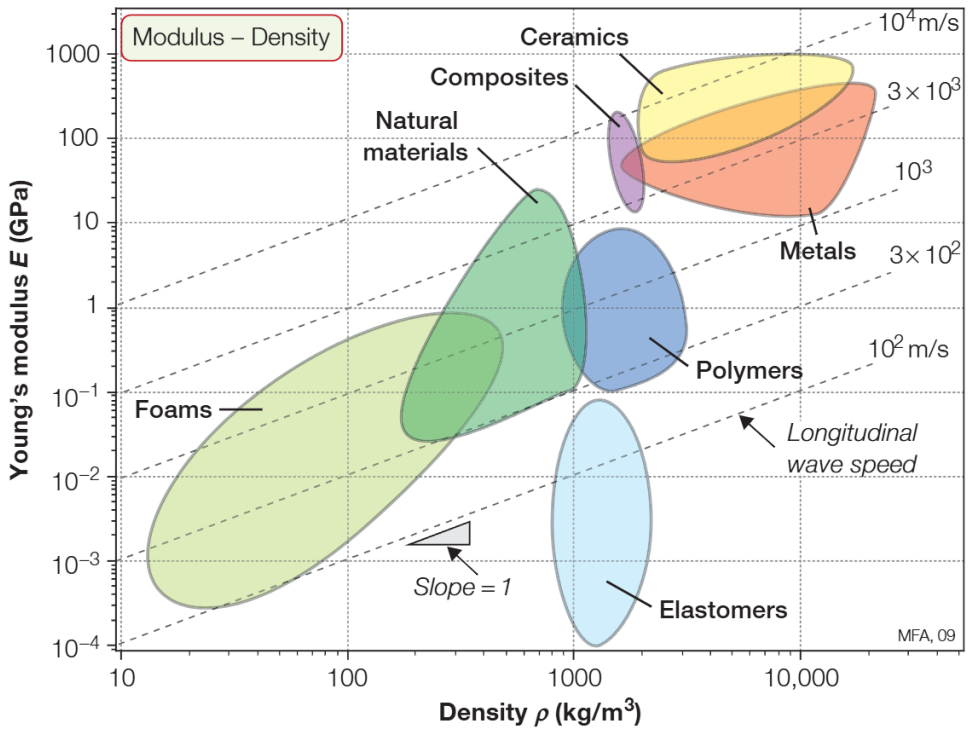

Figure 5.1 – Ashby diagram illustrating the relationship between elastic modulus and density for different classes of materials [111]

In view of this, for the proper design of a structural component, it is essential to understand both the magnitude of the applied loads and the manner in which these loads are transmitted throughout the structure. In the case under study, it is crucial to

determine the level at which the loads generated during firing are transferred from the metallic components to the chassis, in order to avoid both underdesign and overdesign of the structure. Furthermore, the accurate identification of regions subjected to the highest mechanical demands allows for a rational structural design, enabling the use of composite materials with localized reinforcements specifically placed in high-demand areas, thereby contributing to a lighter, more efficient, and appropriately dimensioned structure.

The procedure widely employed in mechanical engineering to predict structural behavior under loading is the Finite Element Analysis (FEA). Among the different available formulations, the explicit time integration approach (Explicit Dynamics) is particularly suitable for the problem under investigation, since the reaction resulting from ammunition firing occurs under transient conditions and involves high strain rates, in which inertial effects become significant, as illustrated in Fig. 5.2. The explicit method offers important advantages, as it allows the efficient modeling of highly nonlinear phenomena such as impacts, complex contact interactions, and large deformations [94, 95, 96].

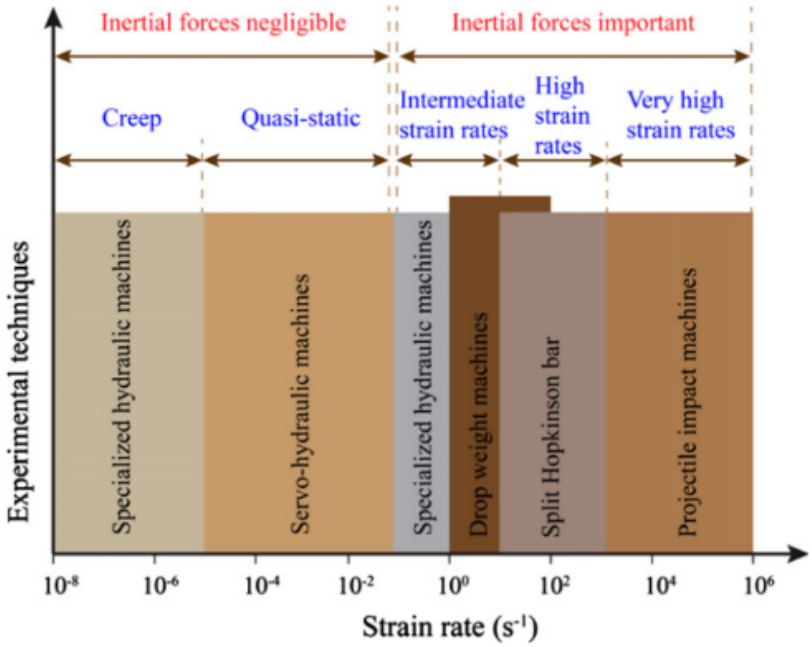

Figure 5.2 – Relationship between strain-rate ranges and the different experimental methods used for their investigation, highlighting the regimes in which inertial effects become relevant [112].

However, the fidelity of the numerical model relies on its validation, defined as the process of demonstrating that the model adequately represents the physical behavior of the system for the quantities of interest [10, 113]. In this context, the aim is to assess whether the model adopted to predict chassis deformations can consistently reproduce the experimentally observed structural behavior through a comparison between numerical and experimental results.

One of the experimental techniques widely employed for the validation of numerical models is Digital Image Correlation (DIC). It is a non-contact optical technique extensively used for measuring full-field displacement and strain fields in materials and structures. The method is based on the correlation between digital images acquired before and during specimen deformation, enabling the spatial reconstruction of displacement fields through the tracking of random patterns applied to the material surface [14, 17, 114, 15].

Due to its high spatial resolution and versatility, DIC has been widely used in the experimental characterization of materials subjected to different loading regimes, constituting a well-established tool for numerical model validation and the investigation of complex mechanical phenomena [22, 20, 16, 115].

In the context of dynamic phenomena, particularly those associated with high strain rates, the technique has evolved into what is known as High-Speed Digital Image Correlation (HS-DIC). In this approach, high frame-rate cameras are employed to capture short-duration transient events, such as impacts, stress waves, and rapid dynamic processes [8, 9, 30, 32, 33, 34]. The application of HS-DIC introduces additional challenges related to illumination, spatiotemporal resolution, and synchronization [31, 37], but enables the acquisition of time-dependent strain fields, which are essential for the analysis of inertial effects and for the validation of explicit dynamic models.

Based on the experimental fields obtained by DIC, different strategies can be adopted for comparison with numerical models. The measured fields may be used for direct validation of simulation results through the comparison of displacement fields, strain fields, or derived quantities. Alternatively, more advanced methodologies integrate the experimental data into the modeling process itself, either through the updating of constitutive parameters or through iterative correction of the numerical model, thus constituting inverse identification or model updating approaches [42, 116, 43].

A direct comparison between results obtained by Finite Element Analysis (FEA) and Digital Image Correlation (DIC) may, at first glance, appear to be an immediate solution for the validation of strain fields. However, such a comparison must be performed with caution, since the two approaches are based on distinct principles: while FEA determines displacement and strain fields through the numerical solution of constitutive and equilibrium equations, DIC obtains them experimentally by means of optical tracking of the tested specimen surface.

In this context, studies such as that of Lava et al. [10] show that, in order to achieve high quantitative compatibility between numerical and experimental results, specific data acquisition and processing procedures are required. Nevertheless, several studies in the literature demonstrate that direct comparison between FEA (Explicit Dynamics) and DIC is valid when the objective is the global assessment of structural behavior. Works such as those by Spranghers et al. [39], Oka et al. [117], and Lopes et al. [118] show that, even without the use of advanced correction techniques, it is possible to obtain consistent

results, with numerical and experimental strain fields of the same order of magnitude and capable of adequately representing the dominant mechanisms of the analyzed impact phenomenon.

Therefore, in the present study, direct comparison between experimental and numerical results is adopted as a tool for validating the deformations in a region close to the location where load transfer from the metallic components to the chassis occurs. This comparison makes it possible to assess whether the initial conditions, boundary conditions, and applied loads in the simulation were correctly represented.

Once this local behavior is validated, the numerical model is assumed to be representative of the system, allowing the identification of the most highly loaded internal regions associated with load transfer from the interface with the metallic components. In this way, it becomes possible to perform design optimizations with greater confidence, improving the structural performance of the chassis and increasing the reliability of the component throughout its service life.

The available literature review did not reveal studies directly comparable to the present work regarding firearms applications, which further reinforces its relevance. The adopted methodology is used for numerical model validation and, once its representativeness is verified, enables computational optimization of the structural design with reduced dependence on repetitive experimental tests. Such tests are costly, requiring substantial ammunition consumption and specialized shooting-range infrastructure.

5.2 Numerical Modeling

5.2.1 Theoretical Formulation of the Dynamic Problem

Initially, a concise overview of the conceptual framework adopted in the *LS-DYNA* manual [94] for the formulation of the mechanical problem is presented. The approach begins with the description of the material as a continuum, aiming to establish the fundamental equations governing the motion of the body. Subsequently, these equations are discretized using the finite element method, enabling their numerical solution.

Within the framework of continuum mechanics, the current position of a material point is described as a function of its reference configuration and time, according to

$$x_i = x_i(X_\alpha, t), \tag{5.1}$$

where X_α denote the material coordinates and x_i the current spatial coordinates. Based on this kinematic description, the displacement, velocity, and acceleration fields are defined, which form the basis of the dynamic problem formulation.

The mechanical behavior of the body is governed by the equation of conservation of linear momentum,

$$\sigma_{ij,j} + \rho f_i = \rho \ddot{x}_i, \tag{5.2}$$

where σij denotes the Cauchy stress tensor, f_i represents the body forces per unit mass, and $\ddot{x}_i$ is the material acceleration. This equation expresses the balance between internal forces, externally applied forces, and inertial effects.

The boundary conditions associated with the problem include traction conditions imposed on part of the boundary,

$$\sigma_{ij} n_j = t_i \quad \text{on } \partial b_1, \tag{5.3}$$

as well as prescribed displacement conditions,

$$x_i = D_i(t) \quad \text{on } \partial b_2. \tag{5.4}$$

Furthermore, in situations involving internal discontinuities or contact regions, continuity of tractions across the interface is imposed,

$$\sigma_{ij}^{+} n_j - \sigma_{ij}^{-} n_j = 0 \quad \text{on } \partial b_3. \tag{5.5}$$

From a complementary standpoint, the model also considers the conservation of mass and energy as fundamental principles governing mechanical behavior. The formulation accounts for effects associated with volumetric deformation and deviatoric distortion of the material. Although these aspects are essential for the physical consistency of the model, their detailed formulation is not addressed in the present work.

In light of the preceding considerations, the governing equation of motion, previously introduced in Eq. (5.2), is revisited and restated below:

$$\sigma_{ij,j} + \rho f_i = \rho \ddot{x}_i. \tag{5.6}$$

To obtain a formulation suitable for variational treatment, an admissible virtual displacement field δx_i is introduced, which satisfies the kinematic conditions imposed on the boundary where displacements are prescribed. By multiplying the equation of motion by δx_i and integrating over the current domain v, one obtains

$$\int_v \delta x_i \left(\sigma_{ij,j} + \rho f_i - \rho \ddot{x}_i \right) dv = 0. \tag{5.7}$$

The term involving the divergence of the stresses is then treated by applying the divergence theorem, which allows the volumetric integral to be rewritten as the sum of a surface contribution and an internal contribution,

$$\int_v \sigma_{ij,j}\, \delta x_i \, dv = \int_{\partial v} \sigma_{ij} n_j \, \delta x_i \, ds - \int_v \sigma_{ij} \, \delta x_{i,j} \, dv. \tag{5.8}$$

The first term on the right-hand side corresponds to the integral defined over the boundary of the domain and represents the virtual work of the tractions acting on the surface. In particular, when considering the portion of the boundary on which surface forces are prescribed, denoted by ∂b_1, the following condition holds:

$$\sigma_{ij} n_j = t_i, \tag{5.9}$$

so that this contribution can be written as

$$\int_{\partial b_1} t_i \, \delta x_i \, ds. \tag{5.10}$$

The second term corresponds to the internal work associated with the stresses within the domain and is directly related to the deformation of the continuum.

By gathering the obtained terms, the weak form of equilibrium can be written as:

$$\underbrace{\int_v \sigma_{ij} \, \delta x_{i,j} \, dv}_{\text{internal work}} - \underbrace{\int_v \rho f_i \, \delta x_i \, dv}_{\text{work of body forces}} - \underbrace{\int_{\partial b_1} t_i \, \delta x_i \, ds}_{\text{work of surface forces}} + \underbrace{\int_v \rho \ddot{x}_i \, \delta x_i \, dv}_{\text{inertial term}} = 0. \tag{5.11}$$

This expression shows that the equilibrium of the system results from the balance among four fundamental contributions: the internal work of the stresses, the work of the body forces, the work of the surface forces, and the inertial term.

From this variational formulation, the spatial discretization of the domain is carried out by means of interpolation functions, leading to the matrix form of the dynamic problem,

$$\mathbf{M}\,\ddot{\mathbf{x}}(t) + \mathbf{K}\,\mathbf{x}(t) = \mathbf{f}_{\text{ext}}(t), \tag{5.12}$$

n which $\mathbf{M}$ represents the mass matrix, $\mathbf{K}$ the structural stiffness matrix, and $\mathbf{f}_{\text{ext}}(t)$ the external force vector.

In more general situations, dissipative and nonlinear effects can be incorporated through additional terms, leading to the extended form

$$\mathbf{M}\,\ddot{\mathbf{x}}(t) + \mathbf{C}\,\dot{\mathbf{x}}(t) + \mathbf{K}\,\mathbf{x}(t) + \mathbf{R}(\mathbf{x}, \dot{\mathbf{x}}) = \mathbf{f}_{\text{ext}}(t) \tag{5.13}$$

in which $\mathbf{C}$ represents the damping matrix and $\mathbf{R}(\mathbf{x}, \dot{\mathbf{x}})$ gathers the associated nonlinear effects, such as geometric and constitutive nonlinearities, as well as contact phenomena.

5.2.2 Time integration scheme

Starting from the theoretical formulation of the dynamic problem, expressed by Eq. (5.13), the system response can be obtained by means of time integration procedures, whose choice depends on the nature of the phenomenon under analysis and on the numerical characteristics of the adopted model.

When the problem under consideration is static and within the elastic regime, it is assumed that the loading is applied sufficiently slowly so that inertia and damping effects become negligible. Under these conditions, the equation of motion given by Eq. (5.13) can

be simplified, resulting in a time-independent problem in which the structural response is obtained from the equilibrium between internal and external forces:

$$\mathbf{K}\,\mathbf{x} = \mathbf{f} \tag{5.14}$$

On the other hand, in dynamic problems, in which the loading varies significantly with time, inertial effects start to influence the structural response, making it necessary to explicitly account for time in the analysis. In such cases, the equation of motion given by Eq. (5.13) must be solved by means of time integration methods capable of describing the evolution of the system state over time.

Time integration methods differ in the way the displacements $\mathbf{x}(t_{i+1})$ and velocities $\dot{\mathbf{x}}(t_{i+1})$ are computed from the quantities known at the previous time step, such as the displacements $\mathbf{x}(t_i)$, velocities $\dot{\mathbf{x}}(t_i)$, accelerations $\ddot{\mathbf{x}}(t_i)$, and the external forces $\mathbf{f}\text{ext}(t_i)$ and $\mathbf{f}\text{ext}(t_{i+1})$. In general, time integration methods can be classified into two main categories: implicit methods and explicit methods.

In implicit methods, the displacements $\mathbf{x}(t_{i+1})$ and velocities $\dot{\mathbf{x}}(t_{i+1})$ at the future time t_{i+1} are determined so as to satisfy the global equilibrium of the structural system at that same instant. That is, they are obtained as the roots of a nonlinear equation in which these quantities appear as unknowns. As a result, iterative procedures are required to compute the solution at each time increment.

In contrast, in explicit methods, global equilibrium is not enforced at the future time step. Within this approach, the displacements and velocities at time t_{i+1} can be determined in closed form from the quantities known at the previous time t_i, namely the displacements, velocities, and accelerations at t_i, as well as the external forces applied at t_i and, potentially, at t_{i+1}. For instance, for structural systems with linear elastic stiffness and linear viscous damping, the time evolution of the system in the explicit method can be expressed by a discrete matrix relation that directly connects the state at time t_i to the state at time t_{i+1} [95]:

$$\begin{bmatrix} \mathbf{x}(t_{i+1}) \\ \dot{\mathbf{x}}(t_{i+1}) \end{bmatrix} = \mathbf{A} \begin{bmatrix} \mathbf{x}(t_i) \\ \dot{\mathbf{x}}(t_i) \end{bmatrix} + \mathbf{B}\,\mathbf{f}_{\text{ext}}(t_i). \tag{5.15}$$

The time evolution matrices $\mathbf{A}$ and $\mathbf{B}$ incorporate the dynamic properties of the structure, since they depend on the mass matrix $\mathbf{M}$, the damping matrix $\mathbf{C}$, the stiffness matrix $\mathbf{K}$, as well as on the time step h adopted in the integration scheme. In this way, the future state of the system at time t_{i+1} is obtained directly from the previously known state and from the structural characteristics of the system, without the need to solve a global algebraic equilibrium system at the considered time instant, which significantly reduces the computational cost compared to the implicit method.

Due to these numerical characteristics, explicit methods are widely employed in the simulation of transient dynamic phenomena, such as impacts and short-duration events

associated with high loading rates. In the present work, the time dependence of the problem is evident, making the adoption of an explicit dynamic finite element formulation suitable for describing the analyzed phenomenon.

5.3 Numerical and Experimental Methodology

The methodology was organized to systematically present the stages employed in the characterization of the problem under study. Initially, the analyzed phenomenon is described, including the firearm, the ammunition, the pressures generated during firing, and the boundary conditions that govern the physical behavior of the system.

Subsequently, the numerical modeling adopted to represent this phenomenon is presented, through which the loading transmitted to the chassis during the firing cycle is obtained. Next, the experimental procedures employed to determine the loads acting on the stock by means of Digital Image Correlation (DIC) are described.

Finally, the methodology for comparing the numerical and experimental results is established, defining the criteria used to assess the level of agreement and to validate the proposed numerical model.

5.3.1 Physical Problem Description

The physical problem under analysis consists of the characterization of the mechanical deformations induced in a polymeric rifle chassis as a result of the loads imposed during firing. The rifle considered is a bolt-action type, equipped with a Mauser-type action mechanism and a barrel designed for the use of .308 Winchester / 7.62 mm ammunition, being intended for precision shooting (sniper) applications.

Figure 5.3 presents images that aid in the understanding of the physical problem under investigation. In (a), the components are arranged to illustrate their assembly as a complete set, through an exploded view. In (b), the manner in which the cartridge rests on the bolt, without the presence of the receiver, is shown, allowing a direct visualization of the contact surfaces involved in the transmission of the load from the cartridge base to the bolt body. In (c), the same configuration is presented, now including the receiver, highlighting the way in which the bolt is supported when the assembly is in the locked condition.

In (d), a sequence of images illustrates the assembly process of the recoil lug component onto the chassis. The Load transfer block is a metallic component responsible for receiving the load transmitted from the receiver and redistributing it to the chassis, promoting the transfer of the load over a larger contact area and reducing local stress concentrations. Finally, in (e), the interface between the receiver and the chassis is shown, highlighting the main region where the loads generated during firing are transferred to the chassis structure.

In summary, the load generated during firing is initially applied to the bolt through the cartridge base and is subsequently transferred to the receiver. The receiver, in turn, transmits the load to the recoil lug, which acts as an intermediate load redistribution element, promoting its dissipation over a larger area of the chassis.

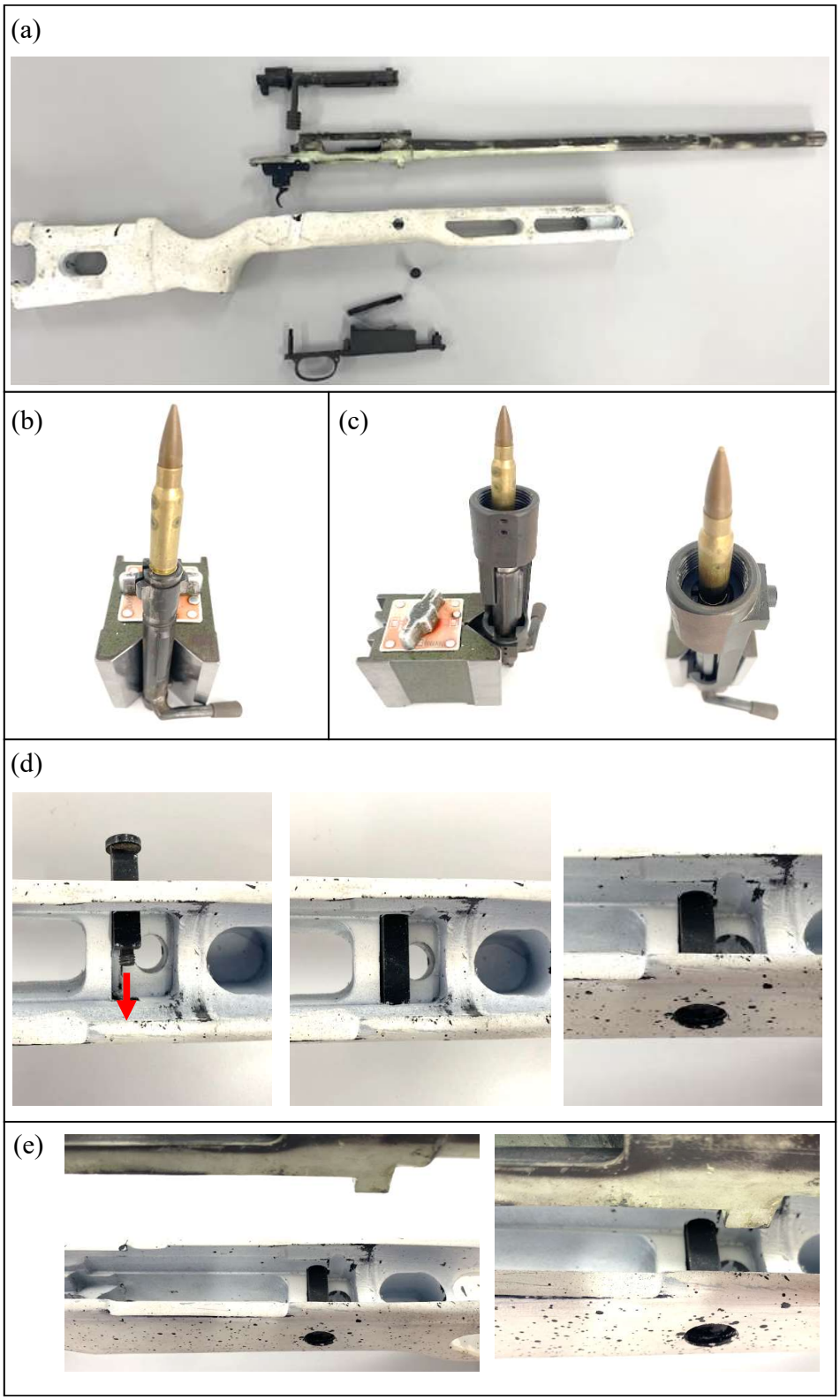

Figure 5.3 – (a) General configuration of the assembly, including the barrel, receiver, firing mechanism, bolt, chassis, and load transfer block. (b) Contact between the cartridge base and the bolt face, without the receiver, indicating the initial load application region. (c) Same configuration as in (b) with the inclusion of the receiver, highlighting the bolt support and the load transfer. (d) Assembly sequence of the load transfer block onto the chassis. (e) Interface between the receiver and the load transfer block, responsible for redistributing the loads to the chassis.

5.3.2 Experimental Methodology

To obtain the experimental results, the Digital Image Correlation (DIC) technique was employed. This method is widely used in the field of experimental mechanics and enables the full-field evaluation of displacement and strain fields of an object under loading. The method is based on the comparison of digital images of an object before and after deformation, through a computationally implemented algorithm.

For the measurement of the strains occurring in the chassis, the two-dimensional variant of the DIC technique (2D-DIC) was adopted. In this configuration, in-plane deformations can be determined provided that the analyzed surface is approximately perpendicular to the camera focal axis. To enable the application of the technique, the chassis was coated with a speckle pattern obtained by spraying black paint over a white base layer.

The 2D-DIC technique presents the important advantage of requiring only a single camera, which is particularly relevant in High-Speed DIC applications, given the high cost of high-speed cameras. In addition, the synchronization challenges inherent to 3D-DIC, which requires two cameras acquiring the same event, are eliminated. In high acquisition rate scenarios, even small temporal offsets between images may result in significant errors in the measurement of strain fields.

The firearm was rigidly mounted on a test stand, whose clamps fixed the front and rear lateral regions of the chassis. In this configuration, the trigger was actuated by means of an extension, promoting the percussion of the 7.62 mm ammunition, and the loads resulting from the deflagration were transmitted from the mechanism to the chassis.

The test stand used is equipped with a mechanism that fixes the firearm to a movable carriage, which translates along a rail and exhibits variable stiffness through a spring-based system, designed to simulate the gradual energy absorption by the shooter's shoulder. However, for the present analysis, the carriage was rigidly locked, so that the energy absorption occurred predominantly through the deformation of the chassis. In this way, the structure was subjected to a more severe loading condition, as illustrated in Fig. 5.4.

Figure 5.4 – Experimental setup, in which the firearm mounted on the test stand can be observed, along with the high-speed camera positioned perpendicular to the firearm axis and connected to a computer for storing the acquired images.

In high-speed cameras based on CMOS sensors, there is an intrinsic trade-off between the acquisition rate (frame rate) and the spatial resolution. As the frame rate is increased, the number of pixels effectively read per frame is reduced. This limitation arises from the fact that the data readout and transfer rates are physically constrained by the sensor architecture. Therefore, to achieve higher frame rates, it becomes necessary to reduce the amount of information acquired per frame, which directly affects the available spatial resolution.

The images were acquired using a Photron FASTCAM SA-Z Type 200K camera, recording the behavior of the stock during firing at 5,000 fps and 30,000 fps. In an exploratory manner, the recordings at 5,000 fps were initially used in order to obtain an overall view of the phenomenon under investigation. The analyzed surface was illuminated using natural sunlight, which provided sufficient brightness and contrast to ensure reliable image acquisition and correlation performance during the DIC measurements.

However, considering that the entire firing event occurs within a time interval on the order of 0.0015 s, the recordings at 30,000 fps were employed for the Digital Image

Correlation (DIC) analysis, in order to capture images with higher temporal resolution. To mitigate the reduction in spatial resolution associated with the increase in frame rate, the acquisition at 30,000 fps was performed with the region of interest (ROI) adjusted to the analysis field, thereby preserving the pixel density in the critical area, as shown in Fig. 5.5.

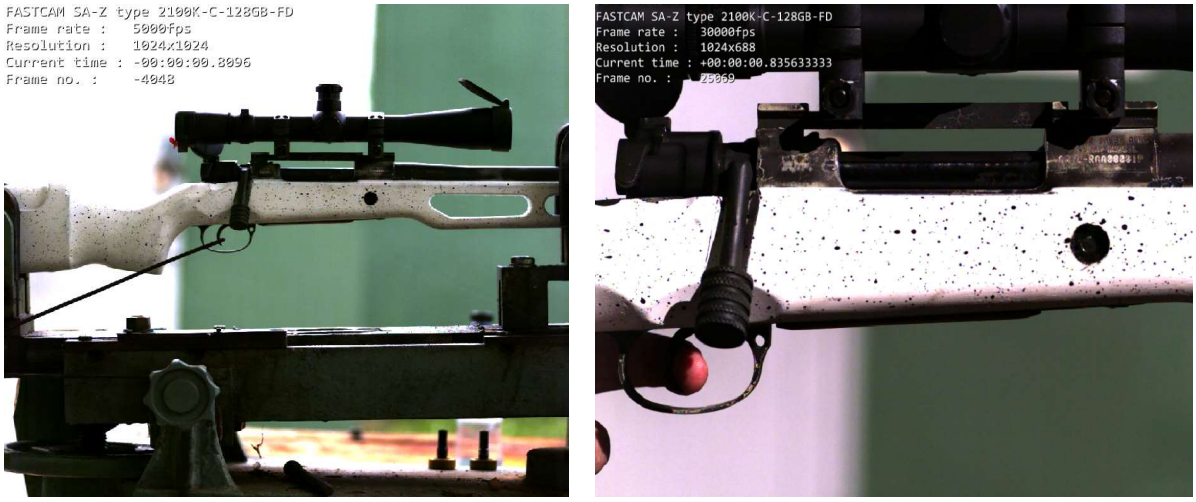

(a) (b)

Figure 5.5 – Frame from the high-speed recording performed at 5,000 fps, used for exploratory purposes (a). Frame from the recording performed at 30,000 fps, highlighting the analysis region (b).

Since the chassis is an ergonomic component, it presents numerous curvatures, leaving only a small region near the mechanism with a sufficiently flat surface to allow accurate analysis using 2D-DIC. The DIC analysis was performed using the VIC-2D software. For image processing, a subset size of 67 pixels was adopted, associated with a step size of 21 pixels.

The relatively large subset size proved to be necessary due to the speckle pattern employed, which was characterized by a more sparse distribution of marks. Under these conditions, it becomes essential to use a sufficiently large pixel area to ensure the presence of adequate textural information in each subset, enabling reliable tracking throughout the image sequence.

The evaluated quantities were the normal strains associated with the axes of the adopted coordinate system, namely ε_{xx} and ε_{yy}. The choice of analyzing strain fields, rather than displacement fields u and v, is justified by the presence of rigid body motion of the component during the analyzed event. Such motion could be incorrectly interpreted as deformation if displacements were used directly, whereas the computation of strains allows these effects to be filtered out and the actual mechanical response of the material to be isolated.

5.3.3 Numerical Methodology

Considering that the involved loads exhibit a dynamic nature and high application rates, an explicit finite element analysis (explicit FEA) was adopted, using the LS-DYNA software. The geometry of the Mauser-type mechanism was simplified so as to include only the components relevant to the phenomenon under investigation, namely the transmission of the load generated at the bolt, its propagation through the receiver and the load transfer block, and, finally, its transfer to the chassis, as illustrated in Fig. 5.6.

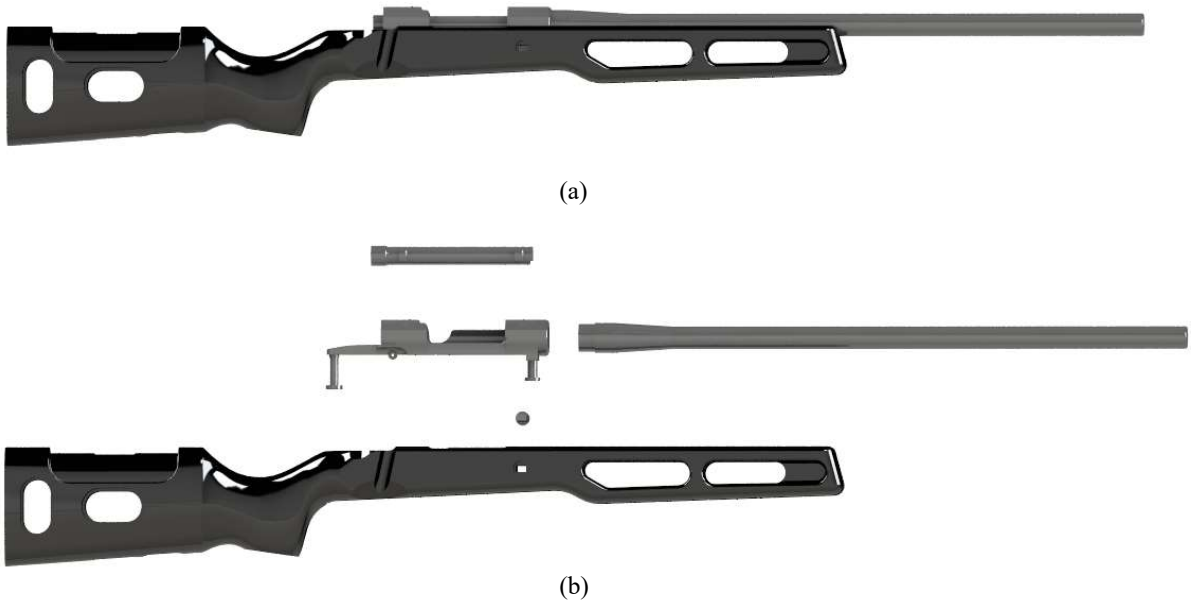

(a)

(b)

Figure 5.6 – CAD geometry of the Mauser-type mechanism assembled onto the chassis (a). Exploded view highlighting the assembly and the simplification of the components (b).

The interactions between the different components of the numerical model were represented using the AUTOMATIC_SINGLE_SURFACE contact algorithm, which is widely employed in crashworthiness analyses. This type of contact is particularly suitable for problems characterized by high loading rates and interactions among multiple bodies, features that resemble the conditions analyzed in the present work [119].

The numerical model was discretized using second-order tetrahedral solid elements (ELFORM 13), as illustrated in Fig. 5.7, totaling approximately 2.76×10^6 elements. With regard to the mesh, explicit methods typically require a homogeneous discretization, preferably based on hexahedral elements. Given the complexity of the CAD geometry, a tetrahedral mesh was adopted in order to preserve mesh homogeneity.

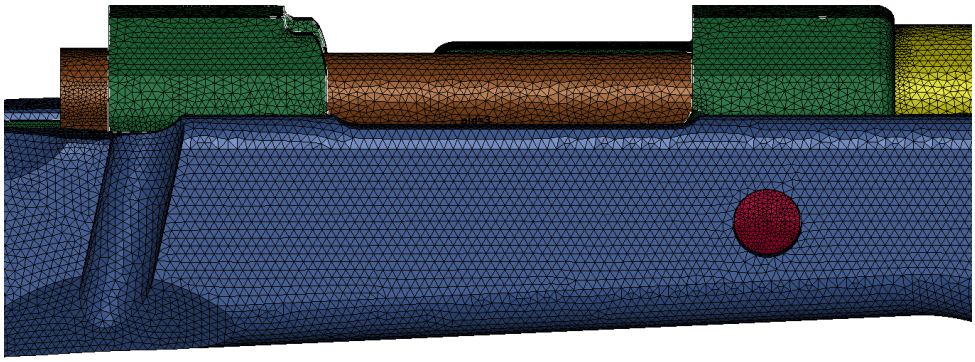

Figure 5.7 – Detailed mesh in the main analysis region, where will be compared with the experimental results.

With regard to the constitutive material models, since the main interest of the present work lies in the evaluation of the deformations of the polymeric chassis, the metallic components of the assembly were modeled as rigid bodies using the MAT_RIGID (020) model. For these components, typical properties of structural steel, such as density, elastic modulus, and Poisson's ratio, were assigned in order to properly represent inertial effects, since their deformations are negligible when compared to those of the chassis. For the polymeric chassis, the PLASTIC KINEMATIC (MAT_003) constitutive model was employed, using typical parameters of polyacetal (POM), so as to represent the elastoplastic behavior of the material under the considered loading regime.

As boundary conditions, translational and rotational constraints were applied along all axes at the same regions where the chassis is fixed to the test stand, as illustrated in Fig. 5.8, by means of the LS-DYNA command BOUNDARY_SPC_SET.

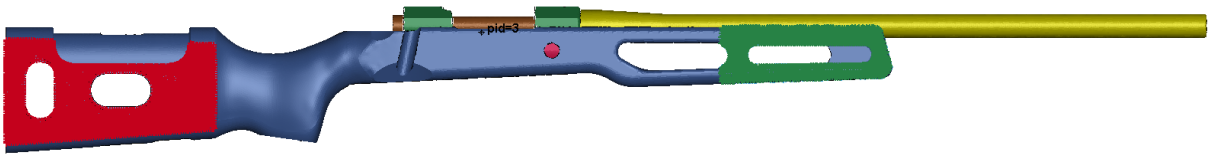

Figure 5.8 – Boundary conditions applied to the chassis, in a manner consistent with the physical problem, with kinematic constraints at the posterior (green) and anterior (red) regions.

As the applied loading, the pressure curve developed by the ammunition, shown in Fig. 5.9, was imposed on the contact region between the cartridge base and the bolt. The firing process occurs over a time interval on the order of 0.0015 s, with the peak mechanical loading being established between 0.0002 and 0.0005 s after percussion. Within this interval, maximum chamber pressures on the order of 330–350 MPa are developed.

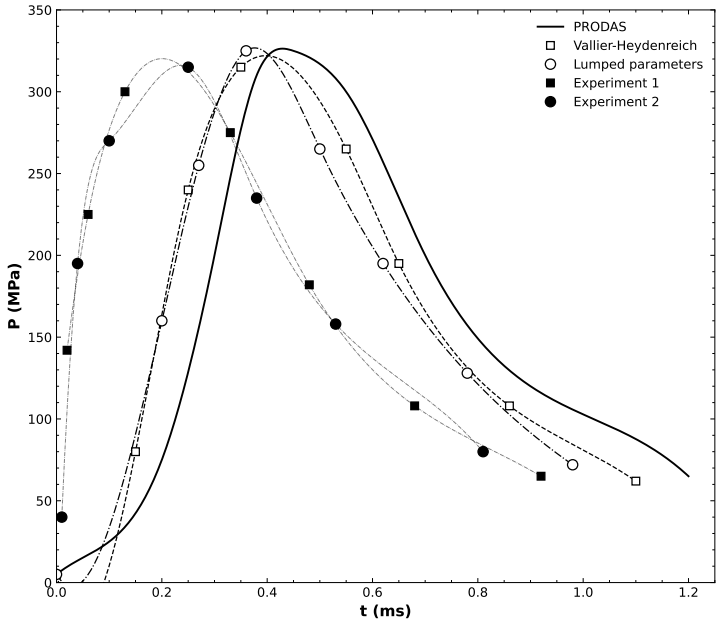

Figure 5.9 – Theoretical and experimental pressure curves developed in the chamber by the 7.62 mm NATO ammunition (adapted from [120]).

This approach constitutes the main simplifying assumption of the present work, since it allows the loading transmitted to the assembly during firing to be adequately represented. Such a simplification is justified because the objective is not to evaluate the loads acting on the barrel of the firearm. Therefore, the radial loads exerted by the cartridge case on the chamber wall, as well as the effects associated with the projectile motion along the barrel, were not considered. Although physically present, these contributions would imply a significant increase in the complexity of the numerical model, without a relevant impact on the structural response of interest.

Accordingly, the effect of the pressure acting in the axial direction was considered dominant, as it is responsible for transmitting the load toward the rear of the firearm. In Fig. 5.10, where the barrel and the bolt were omitted for visualization purposes, the region of application of the pressure curve can be clearly identified.

Figure 5.10 – Red arrow indicating the region of application of the ammunition pressure curve on the bolt face.

From the numerical results, the strain fields ε_{xx} and ε_{yy} of the chassis were extracted in order to compare them with the experimental results. In addition, after validation of the

simulation, the distribution of the von Mises equivalent stress in the chassis was evaluated, so as to identify the regions subjected to the highest mechanical loads induced by firing.

5.3.4 Methodology for Numerical-Experimental Comparison and Validation

The load generated during firing is predominantly transmitted from the receiver recoil lug to the component referred to as the load transfer block, which is inserted inside the chassis. The purpose of this component is to transfer the load from a reduced contact area associated with the lug to a larger contact area in the chassis, thereby promoting a more uniform stress distribution and reducing local load concentration, as illustrated in Fig. 5.3.

Due to this load transfer mechanism, the region of the chassis in direct contact with the load transfer block becomes one of the most highly loaded areas of the assembly. However, since this is an internal region of the stock, direct experimental validation is not feasible, as the deformations at this interface cannot be measured using the Digital Image Correlation (DIC) technique.

Therefore, the validation of the numerical model is conducted in an accessible region on the external surface of the chassis, located in the vicinity of the highly loaded internal interface. The underlying assumption is that, if satisfactory agreement is achieved between numerical and experimental results in this analysis region, the numerical model can be considered capable of adequately representing the global structural behavior of the component.

With this approach, the boundary conditions, the imposed loading history, and the constitutive model adopted for the chassis material are indirectly validated. Once this validation is established, the methodology can be extended to the analysis of similar problems, allowing for the evaluation of the von Mises equivalent stresses in the interface region and for the quantification of the loading level relative to the yield limit of the material.

This, in turn, enables the refinement of the structural design, either through geometric optimization of the component or through the selection of alternative materials, while maintaining the same constitutive framework, so as to reinforce the most highly loaded regions and reduce mass in less demanded areas. Figure 5.11 presents a flowchart representative of the methodology adopted in this work.

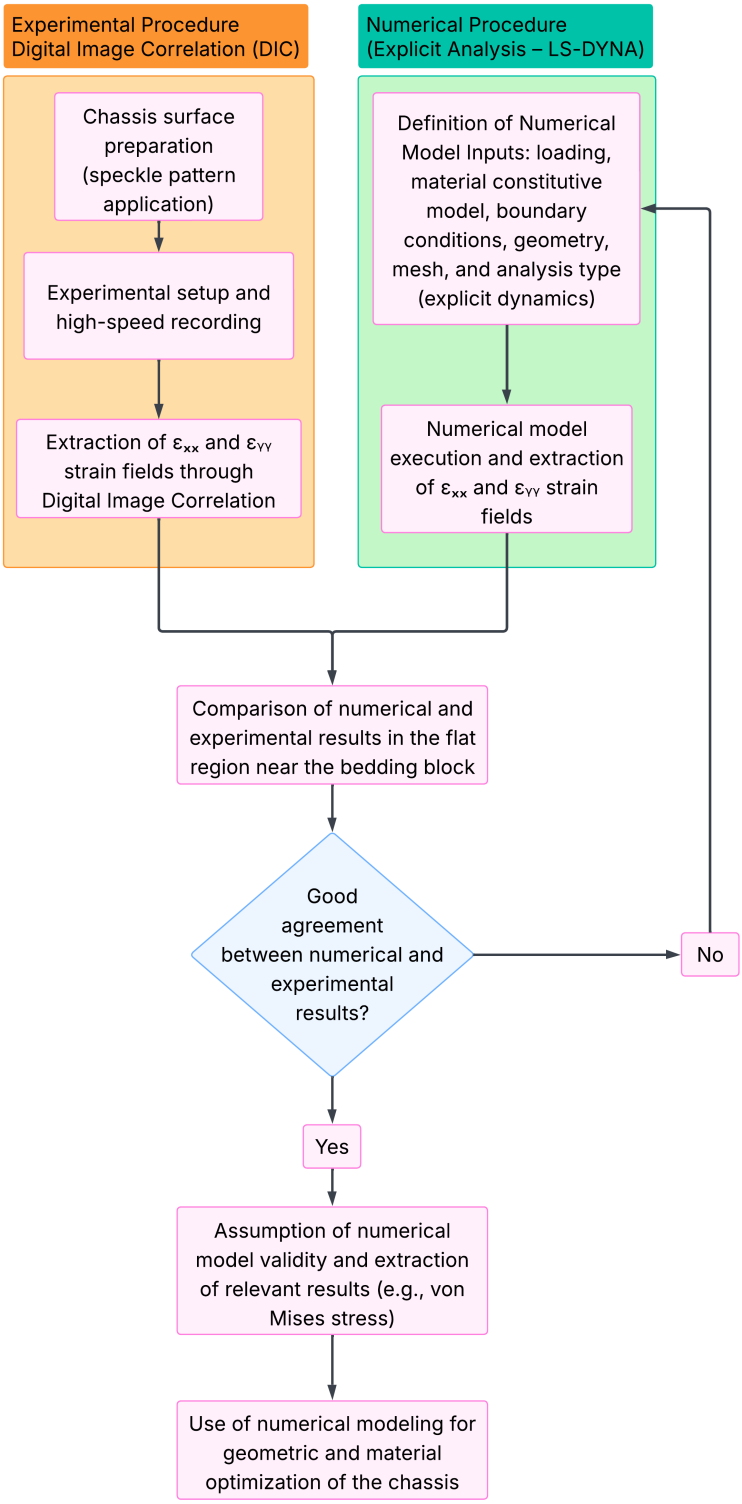

Figure 5.11 – Flowchart of the methodology employed for the validation of the numerical modeling by means of the Digital Image Correlation (DIC) technique.

5.4 Results and Discussion

5.4.1 Experimental Results

When performing the exploratory analysis at 5,000 frames per second on the flat surface under investigation, it was observed that the strain components ε_{xx} and ε_{yy} exhibited significant variations between consecutive frames. As a result, the images acquired at 30,000 frames per second were selected, in order to obtain a smoother and more consistent temporal evolution of the results.

In addition, it was verified that the analyzed surface does not deform in a homogeneous manner between successive frames, with regions subjected to tensile loading and others to compressive loading being observed at the same time instant, as can be seen in Figs. 5.12 and 5.13. Another finding during the exploratory analysis was that the extraction of pointwise strain values proved to be susceptible to local noise, manifested by strain values that are incompatible with the continuity of the field, mainly due to imperfections in the image correlation process.

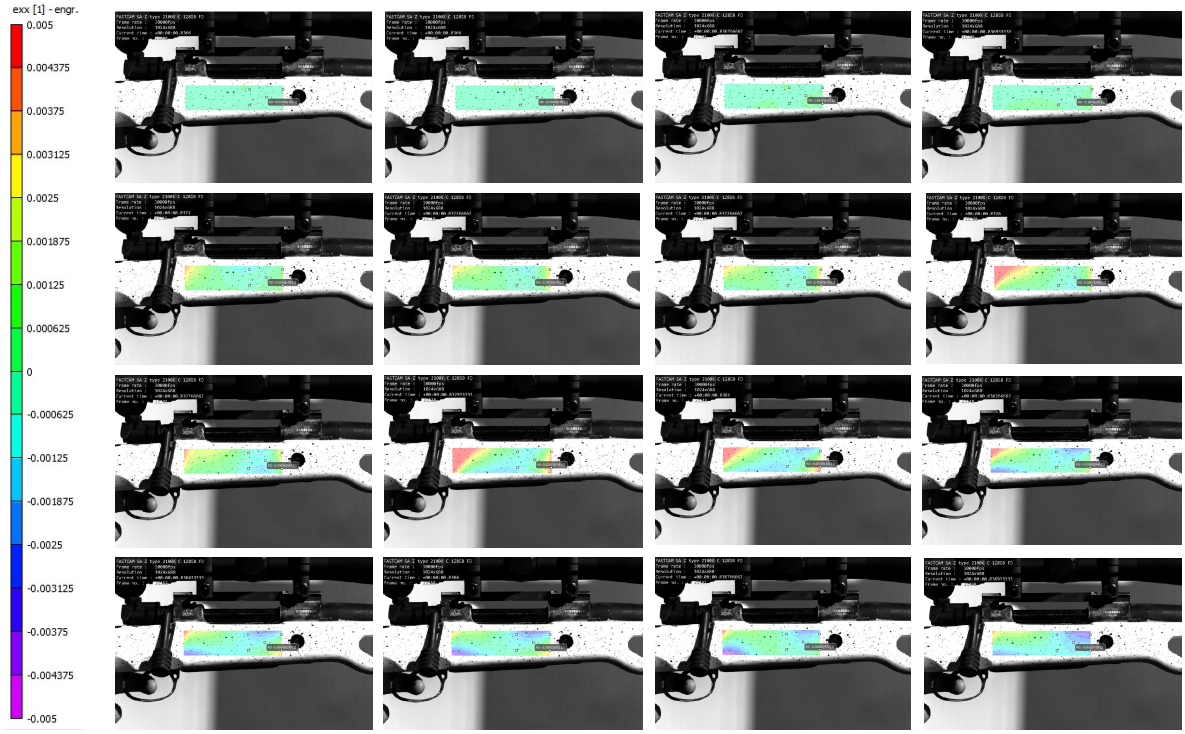

Figure 5.12 – Strain field ε_{xx} on the flat region obtained via DIC, illustrating the spatial variation of strain over the analyzed area.

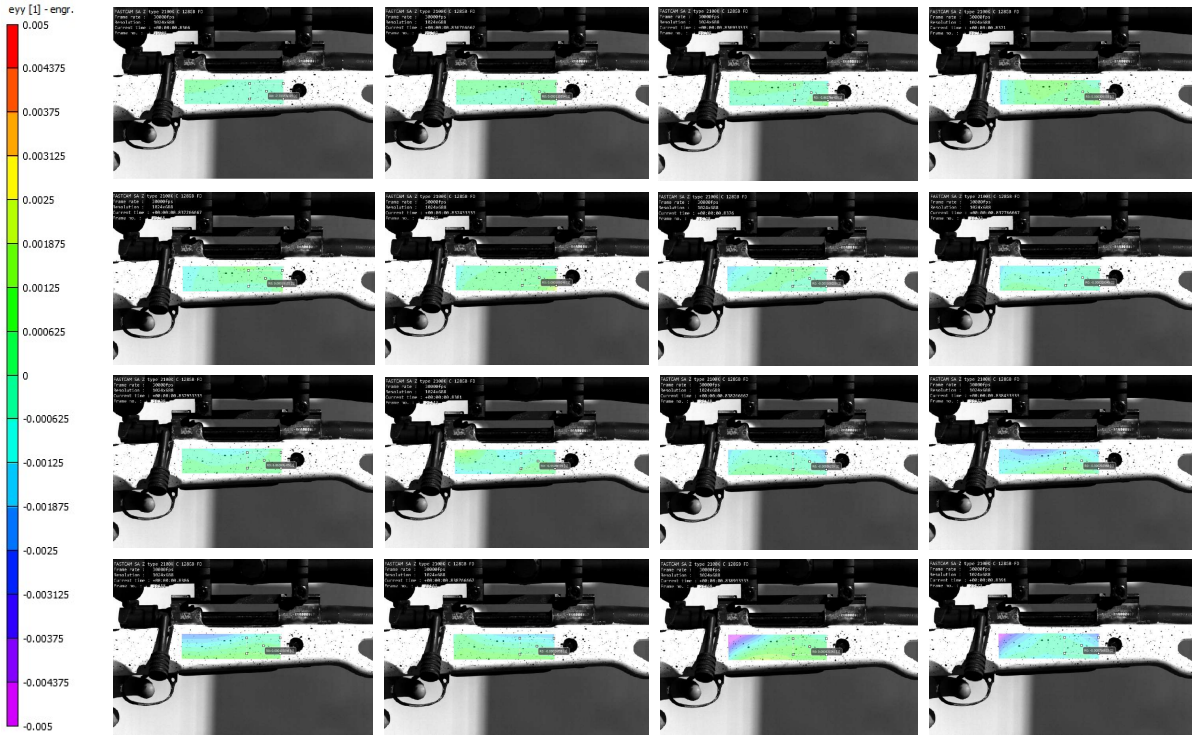

Figure 5.13 – Strain field ε_{yy} on the flat region obtained via DIC, illustrating the spatial variation of the strain over the analyzed area.

With the aim of minimizing this noise and obtaining more representative data, an analysis region was defined in the vicinity of the insertion point of the load transfer block, where the points exhibited similar strain levels over time. From this region, the average strains ε_{xx} and ε_{yy} were extracted, as illustrated in Fig. 5.14.

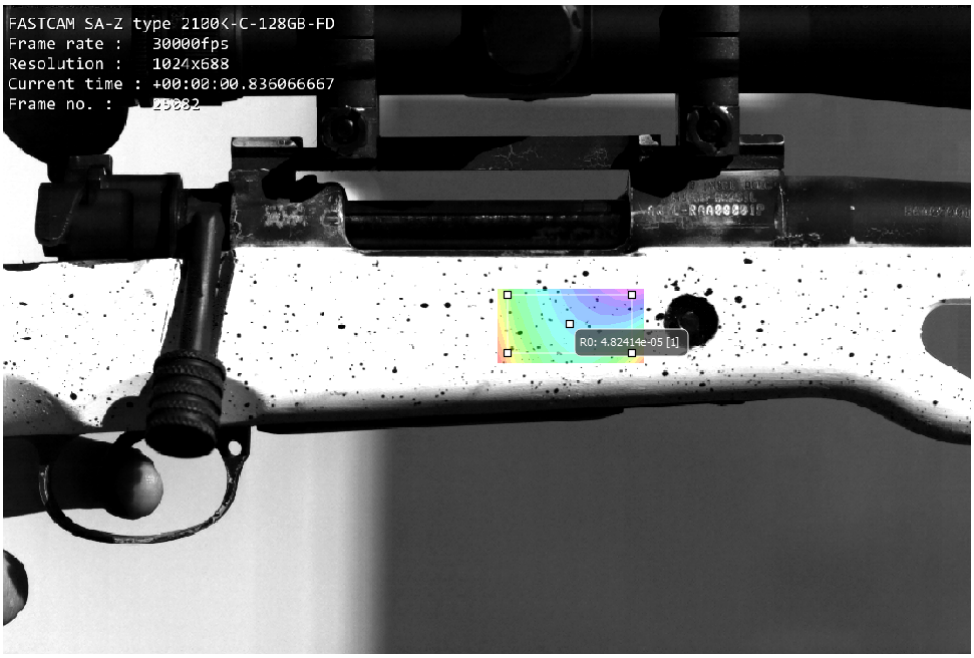

Figure 5.14 – Region from which the experimental results were extracted via DIC, corresponding to the average values of ε_{xx} and ε_{yy}.

The average strains ε_{xx} and ε_{yy} over the analysis region, obtained via DIC, are shown in Fig. 5.15.

(a)

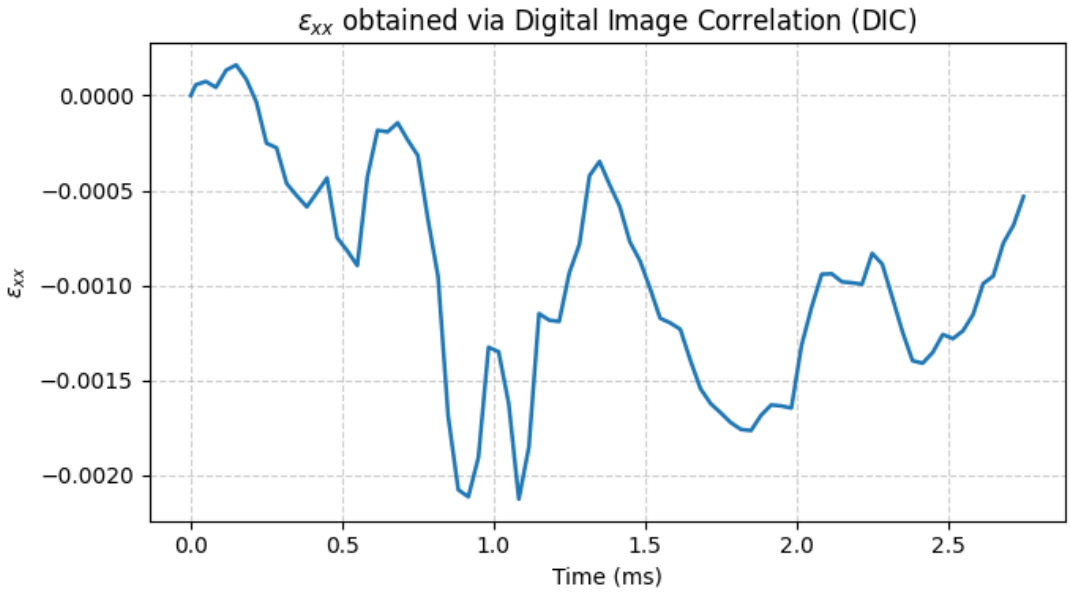

(b)

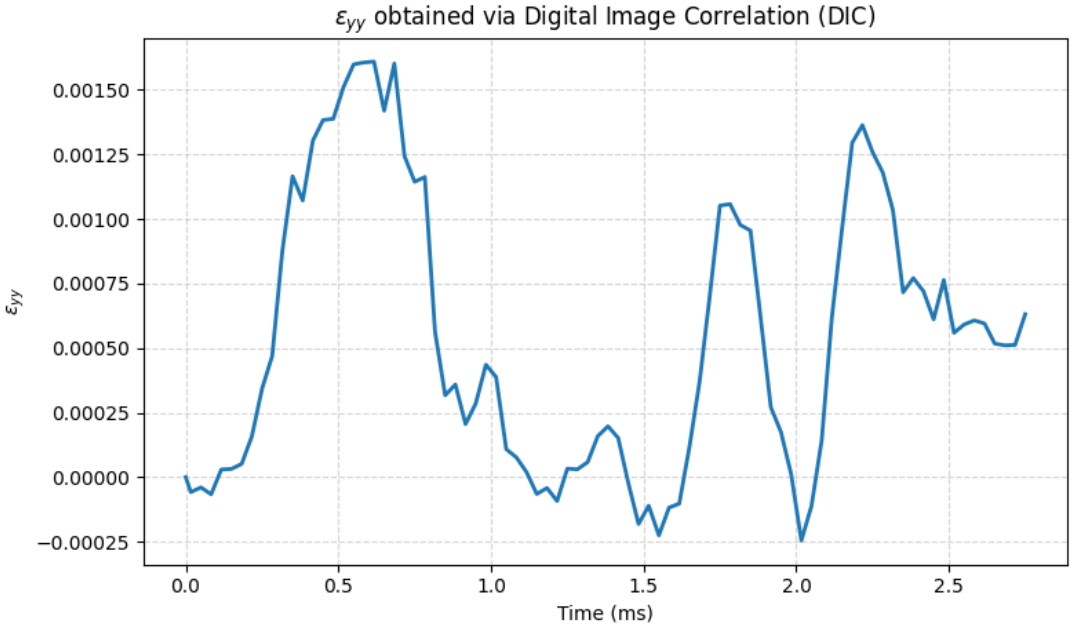

Figure 5.15 – Mean ε_{xx} (a) and mean ε_{yy} (b) over the analysis region, obtained via DIC, up to 0.0026 s after the onset of deformation.

5.4.2 Numerical Results

Unlike DIC, in which the analysis is restricted to the flat region where reliable results can be obtained, the numerical modeling allowed the extraction of the strain fields ε_{xx} and ε_{yy} over the entire extent of the chassis, as shown in Figs. 5.16 and 5.17.

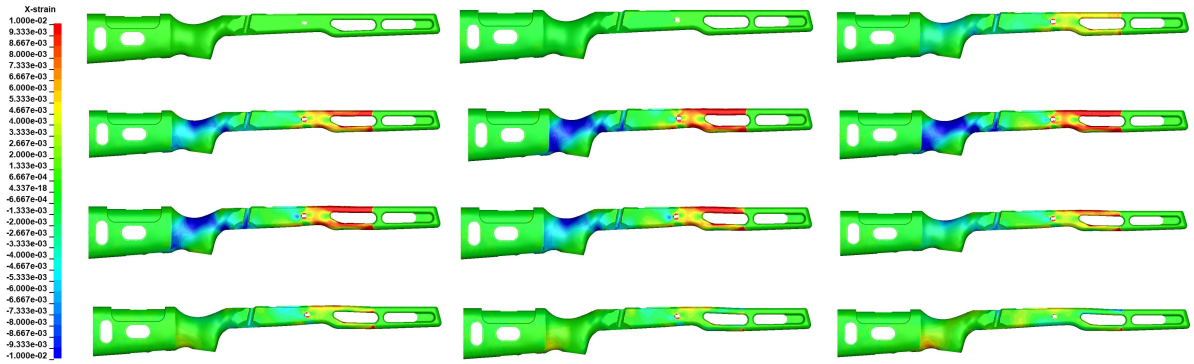

Figure 5.16 – Strain field ε_{xx} obtained via explicit FEA, showing the strain distribution over the entire chassis.

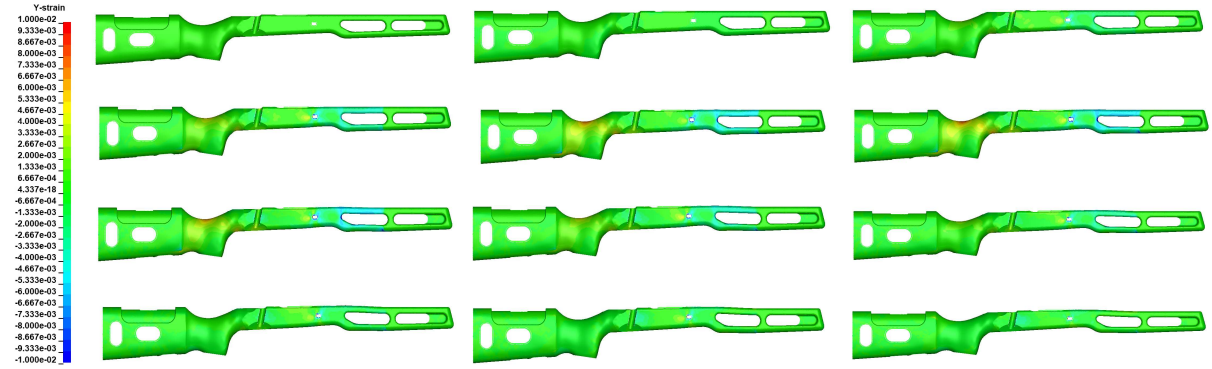

Figure 5.17 – Strain field ε_{yy} obtained via explicit FEA, showing the strain distribution over the entire chassis.

For the validation of the numerical model, the mesh elements corresponding to the DIC analysis area were selected in order to enable a direct comparison. The software provided the strain histories ε_{xx} and ε_{yy} over a time interval of 0.0026 s for each element. An average over all selected elements was computed at each simulation time step, so as to obtain the mean strain in the region, as illustrated in Fig. 5.18.

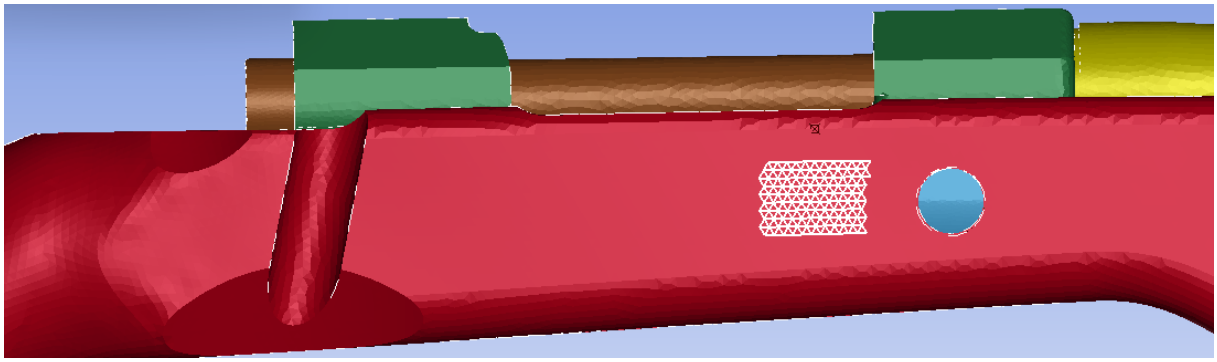

Figure 5.18 – Region from which the mesh elements highlighted were selected for the extraction of ε_{xx} and ε_{yy}.

The obtained results are presented in Fig. 5.19.

(a)

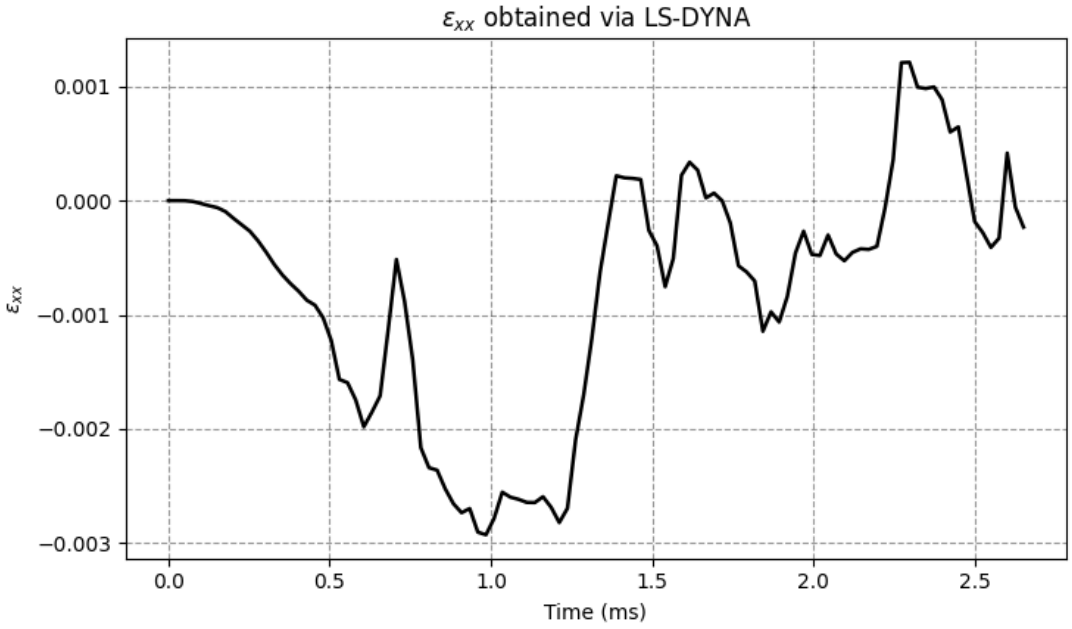

(b)

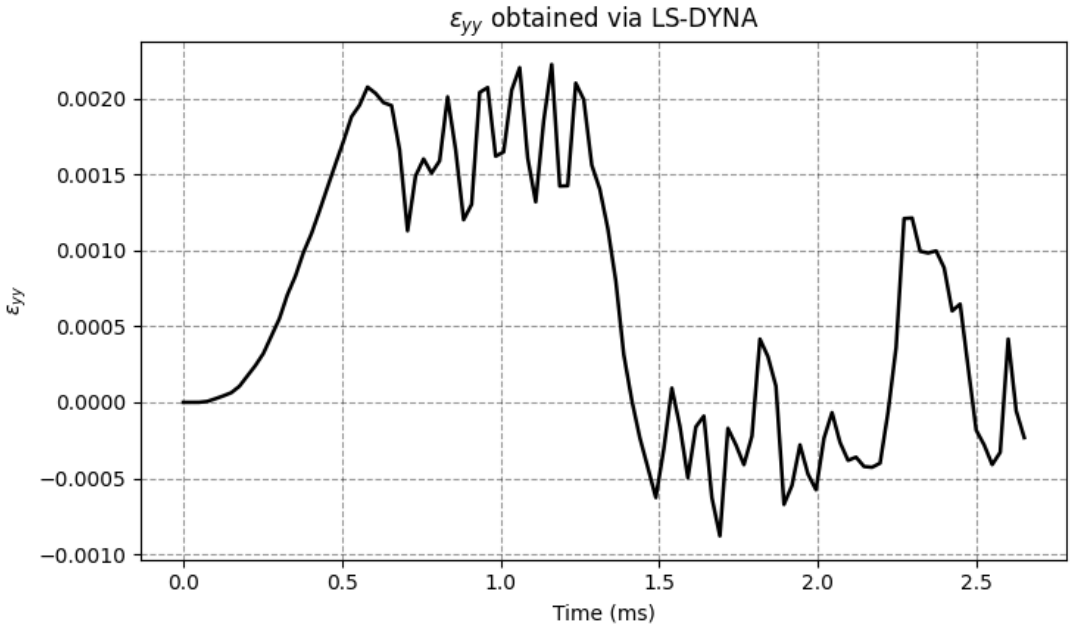

Figure 5.19 – Mean ε_{xx} (a) and mean ε_{yy} (b) obtained via explicit FEA over the analysis region, up to 0.0026 s after the onset of deformation.

5.4.3 Numerical-Experimental Comparison

In Figs. 5.20 and 5.21, the experimental and numerical results are juxtaposed, exhibiting good agreement in both strain magnitude and temporal evolution, particularly during the phase in which the structure is effectively loaded, up to approximately 0.0015 s.

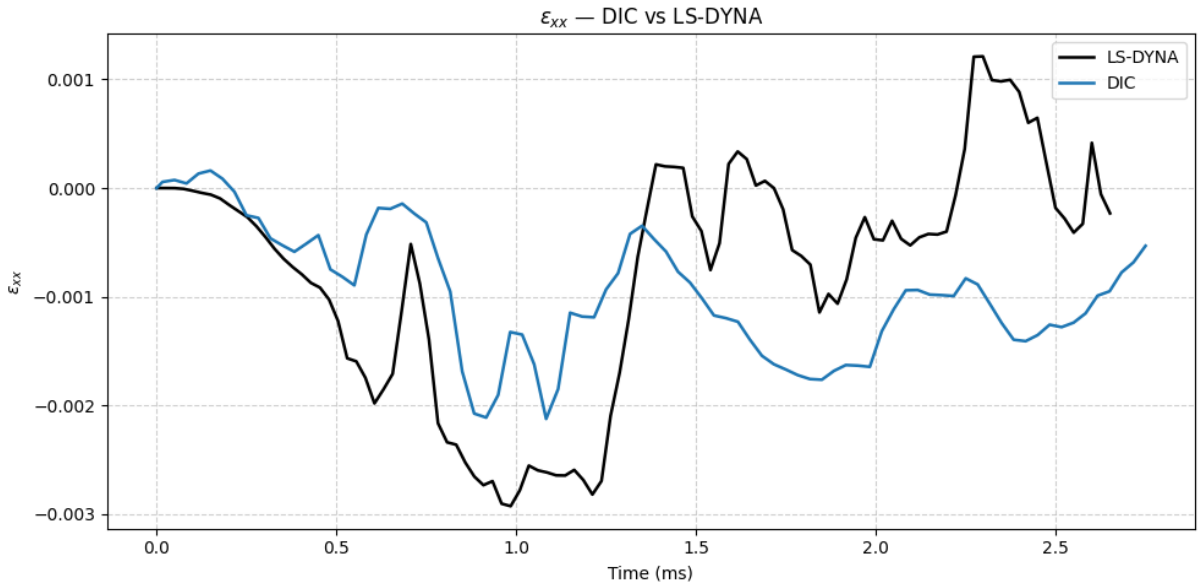

Figure 5.20 – Comparison of the mean ε_{xx} obtained experimentally (DIC) and numerically (FEA).

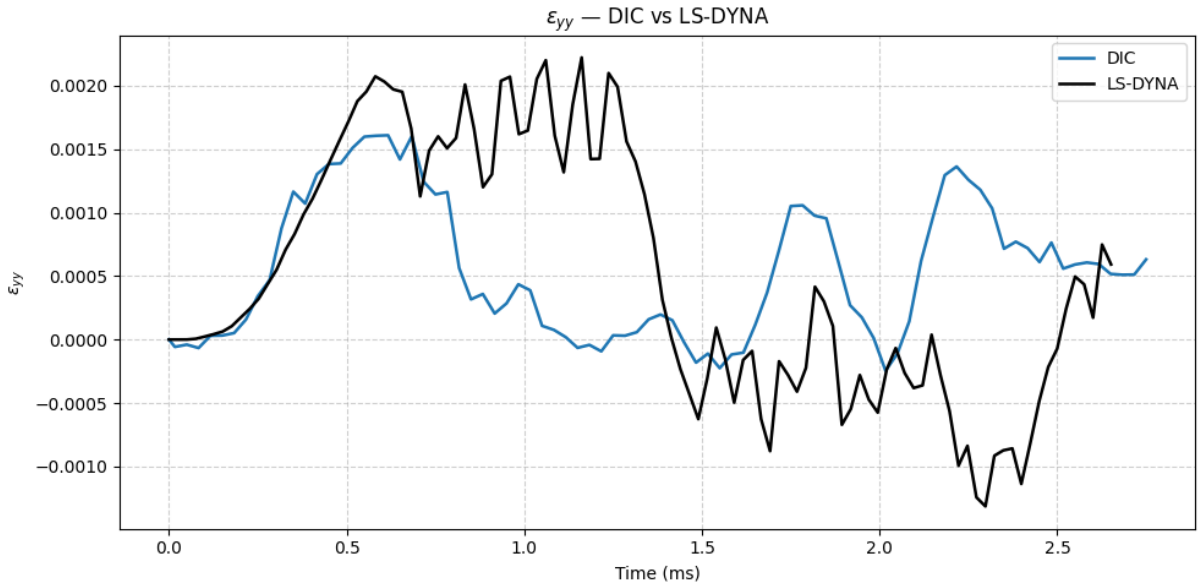

Figure 5.21 – Comparison of the mean ε_{yy} obtained experimentally (DIC) and numerically (FEA).

The analysis of the results was divided into two distinct phases. The first corresponds to the loading phase, in which the observed strains arise predominantly from the assumptions adopted in the simulation and are directly associated with the applied loading and the boundary conditions imposed on the model. The second phase, occurring after approximately 0.0015 s, is mainly associated with the propagation of mechanical waves within the structure.

With regard to the first phase, good agreement is observed between the experimental and numerical results, both in terms of magnitude and in the sequence of strain evolution.

For the ε_{xx} component, an initial compression of the analyzed area is observed, which is expected due to the fixation of the chassis and the application of a compressive-type load. For the ε_{yy} component, an initial tensile response of similar magnitude is observed.

In the second phase, although good agreement is still observed in terms of strain magnitude, the sequence of compression and tension differs between the experimental and numerical results. This indicates that the strains associated with post-loading relaxation do not exhibit the same level of agreement as observed in the initial phase.

The main hypothesis for the differences observed between the results in the loading and post-loading phases is related to the distinct nature of the dominant phenomena in each stage of the event. During the loading phase, the structural behavior is governed mainly by the impulsive action of the firing load and is therefore less sensitive to uncertainties associated with boundary conditions, the adopted constitutive material model, and the simplifications introduced in the loading description.

However, in the phase following firing, the effects associated with the actual system conditions become more pronounced. With regard to the boundary conditions, global displacements of the firearm assembly relative to the supporting structure were experimentally observed, indicating that the fixation stiffness assumed in the numerical model does not fully reproduce the behavior of the physical system.

In addition, the adopted constitutive model has a simplified nature and is not capable of fully representing the nonlinear effects associated with the elastoplastic behavior of the polymeric material, nor the effects related to high strain rates.

Finally, with respect to the loading, it is worth noting that, in the real phenomenon, there is a contribution associated with the projectile motion along the barrel, which directly influences the structural response of the system. However, this effect was suppressed in the adopted modeling strategy, implying a simplification of the applied loading and, consequently, affecting the fidelity of the numerical results when compared to the experimental data.

5.4.4 Design optimization based on numerical–experimental results

Given the good agreement of the results during the initial loading phase, in which the structure is effectively subjected to mechanical solicitation, the analysis of the maximum strains developed in the chassis over time was carried out, as shown in Fig. 5.22. It is observed that the highest strain levels are concentrated in the interface regions between the mechanism and the chassis, which is an expected behavior due to the load transfer occurring in these areas, as illustrated in Fig. 5.23.

Based on this analysis, opportunities for structural design improvement become evident, with the proposal of localized reinforcements in the most highly loaded regions and the introduction of geometric reliefs in less demanded areas. Such modifications can

be implemented in new design cycles while maintaining the adopted constitutive models, through the adjustment of geometric and structural parameters.

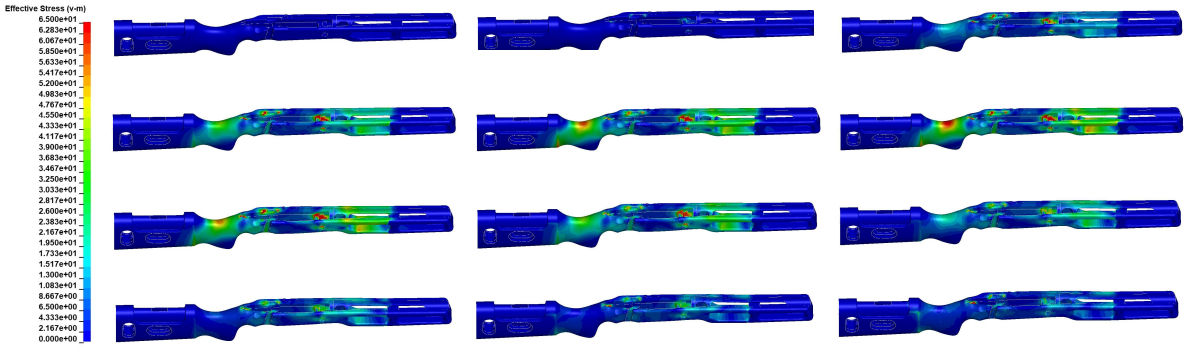

Figure 5.22 – Time evolution of the von Mises equivalent stress in the chassis.

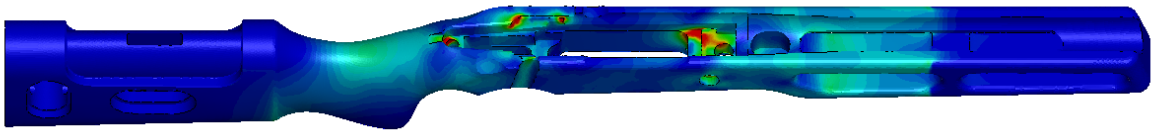

Figure 5.23 – Detail of the von Mises equivalent stress in the structure at the peak loading condition.

5.5 Final Remarks

The present work proposed a methodology for the numerical representation of the loading imposed on a rifle chassis resulting from the firing of 7.62 mm ammunition. For the validation of the numerical model, an experimental test was conducted in which the strain fields ε_{xx} and ε_{yy} were obtained using the Digital Image Correlation (DIC) technique, enabling a direct comparison with the results from the numerical simulation.

A good agreement was observed between the experimental and numerical results, especially within the time interval corresponding to the loading phase of the system, spanning from the firing instant to approximately 1.5 ms. This agreement indicates that the developed model is capable of adequately representing the mechanical behavior of the assembly during the analyzed dynamic event.

Based on the validated model, it was possible to extract relevant information for the structural optimization of the component, particularly the distribution of the von Mises equivalent stresses, allowing the identification of the most highly loaded regions during firing. These results provide a basis for design improvements, enabling mass reduction and geometric optimization without compromising structural integrity.

In this context, the potential use of composite materials is highlighted, as they allow for localized reinforcement in critical regions and material reduction in less demanded

zones, resulting in a more efficient strength-to-weight ratio and better compliance with the structural and functional requirements of the system.

6 CONCLUSIONS

This work described the mechanical behavior of a precision rifle chassis subjected to highly transient loading conditions induced by the firing of 7.62 mm ammunition through a numerical framework validated by Digital Image Correlation (DIC) measurements. The proposed approach successfully integrated high-speed experimental data with explicit finite element modeling.

In order to achieve this objective, a state-of-the-art review of Digital Image Correlation was conducted, with emphasis on high-speed implementations and their integration with finite element analysis for experimental–numerical validation. This review provided the theoretical foundation necessary to support the experimental and numerical procedures adopted in this research.

On the numerical side, an explicit finite element framework was developed to represent the short-duration dynamic loads and significant inertial effects associated with the firing process. The model was capable of describing the mechanical load transfer to the chassis and its structural response under high strain-rate conditions.

From the experimental standpoint, the application of DIC enabled the acquisition of full-field displacement and strain measurements under dynamic conditions during the firing event. These measurements constituted a reliable reference for the validation of the numerical model.

A validation strategy was therefore established, based on the direct comparison between experimental DIC fields and numerical predictions. This approach proved to be effective in assessing the adequacy of the modeling assumptions, boundary conditions, and load descriptions.

In a complementary manner, a strain-rate-dependent constitutive model was defined to describe the mechanical behavior of POM under high strain-rate conditions and constant temperature, aiming to enable a more accurate representation of the material response in dynamic simulations.

As a natural continuation of the present study, future work should focus on the direct implementation of the proposed rate-dependent constitutive model into fully coupled explicit finite element simulations of the firing event. This step will allow a systematic evaluation of whether the refined material formulation leads to improved agreement with experimental measurements when compared to the simplified constitutive models adopted herein. Such an investigation is expected to further enhance the predictive capability of the numerical framework and to consolidate its use as a design tool for composite rifle chassis.

BIBLIOGRAPHY

[1] BRASIL. Ministério do Exército. Estado-Maior do Exército. *IP 21-2: O caçador*. Estado-Maior do Exército. Brasília, 1998.

[2] T. B. S. Pessoa. *O tiro desportivo como direito individual fundamental e patrimônio cultural de relevante interesse social na Constituição Federal de 1988*. 2021. URL: <https://www.jusbrasil.com.br/artigos/o-tiro-desportivo-como-direito-individual-fundamental-e-patrimonio-cultural-de-relevante-interesse-social-na-constituicao-federal-de-1988/1200847180> (visited on 01/17/2026).

[3] National Archives and Records Administration. *The Constitution of the United States: A Transcription*. U.S. National Archives and Records Administration. URL: <https://www.archives.gov/founding-docs/constitution-transcript> (visited on 01/17/2026).

[4] Aaron Karp. *Estimating Global Civilian-Held Firearms Numbers*. Geneva: Small Arms Survey, 2018.

[5] McMillan Group. *McMillan Then and Now*. URL: <https://mcmillanusa.com/title/> (visited on 01/17/2026).

[6] Bing Pan. "Digital image correlation for surface deformation measurement: historical developments, recent advances and future goals". In: *Measurement Science and Technology* 29.8 (2018), p. 082001. DOI: <10.1088/1361-6501/aaa64b>.

[7] Tarig Hassan et al. "Digital Image Correlation with Dynamic Subset Selection". In: *Optics and Lasers in Engineering* 84 (2016), pp. 1–9. DOI: <10.1016/j.optlaseng.2016.03.017>.

[8] Phillip Reu and Timothy Miller. "The Application of High-Speed Digital Image Correlation". In: *Journal of Strain Analysis for Engineering Design* 43.8 (2008), pp. 673–688. DOI: <10.1243/03093247JSA404>.

[9] Bo Liu et al. "Digital image correlation in extreme conditions". In: *Thin-Walled Structures* 205 (2024), p. 112589. DOI: <10.1016/j.tws.2024.112589>. URL: <https://www.sciencedirect.com/science/article/pii/S0263823124010292>.

[10] Pascal Lava et al. "Validation of finite-element models using full-field experimental data: Levelling finite-element analysis data through a digital image correlation engine". In: *Strain* 56.4 (2020), pp. 1–17. DOI: <10.1111/str.12350>.

[11] Andrew E. Lovejoy et al. *Improving Structural Test and Analysis Correlation Using Digital Image Correlation Boundary Measurements*. Tech. rep. NASA/TM–20210022933. NASA Technical Memorandum. Hampton, VA: NASA Langley Research Center, 2021. DOI: <10.25923/y3yy-vb08>. URL: <https://ntrs.nasa.gov/citations/20210022933>.

[12] B. Turoń et al. "DIC in validation of boundary conditions of numerical model of reinforced concrete beams under torsion". In: *Archives of Civil Engineering* 64.4/II (2018), pp. 31–48. DOI: <10.2478/ace-2018-0061>.

[13] R. Fedele. "Extended identification of interface parameters and boundary conditions by inverse analysis". In: *Comptes Rendus Mécanique* 341.5 (2013), pp. 399–410. DOI: <10.1016/j.crme.2013.02.005>. URL: <https://doi.org/10.1016/j.crme.2013.02.005>.

[14] H.A. Bruck et al. "Digital Image Correlation Using Newton-Raphson Method of Partial Differential Correction". In: *Experimental Mechanics* 29.3 (1989), pp. 261–267. DOI: <10.1007/BF02321405>. URL: <https://doi.org/10.1007/BF02321405>.

[15] Bing Pan et al. "Two-dimensional digital image correlation for in-plane displacement and strain measurement: a review". In: *Measurement Science and Technology* 20.6 (2009), p. 062001. DOI: <10.1088/0957-0233/20/6/062001>. URL: <https://doi.org/10.1088/0957-0233/20/6/062001>.

[16] Van-Thuong Nguyen et al. "Mechanical Properties Identification of Sheet Metals by 2D-Digital Image Correlation Method". In: *Procedia Engineering*. Vol. 184. Elsevier, 2017, pp. 381–389. DOI: <10.1016/j.proeng.2017.04.108>.

[17] Jianlong Zhao, Yong Sang, and Fuhai Duan. "The State of the Art of Two-Dimensional Digital Image Correlation Computational Method". In: *Engineering Reports* 1 (2019), e12038. DOI: <10.1002/eng2.12038>. URL: <https://doi.org/10.1002/eng2.12038>.

[18] Yaroslav Blikharskyy et al. "Review of Development and Application of Digital Image Correlation Method for Study of Stress–Strain State of RC Structures". In: *Applied Sciences* 12.19 (2022), p. 10157. DOI: <10.3390/app121910157>. URL: <https://doi.org/10.3390/app121910157>.

[19] Pan Bing et al. "Performance of sub-pixel registration algorithms in Digital Image Correlation". In: *Measurement Science and Technology* 17.6 (2006), pp. 1615–1621. DOI: <10.1088/0957-0233/17/6/045>.

[20] Akshat Agha. "Effectiveness of 2D Digital Image Correlation in Capturing the Fracture Behavior of Sheet Metal Alloys". In: *SAE International Journal of Materials and Manufacturing* 16.2 (2023), pp. 1–16. DOI: <10.4271/05-16-02-0009>. URL: <https://doi.org/10.4271/05-16-02-0009>.

[21] H. W. Schreier, D. Garcia, and M. A. Sutton. "Advances in Light Microscope Stereo Vision". In: *Experimental Mechanics* 44.3 (2004), pp. 278–288. DOI: <10.1007/BF02427962>.

[22] M.A. Sutton et al. "Recent Progress in Digital Image Correlation: Background and Developments since the 2013 W M Murray Lecture". In: *Experimental Mechanics* 57.1 (2017), pp. 1–30. DOI: <10.1007/s11340-016-0233-3>. URL: <https://doi.org/10.1007/s11340-016-0233-3>.

[23] B.K. Bay et al. "Digital volume correlation: Three-dimensional strain mapping using X-ray tomographylava". In: *Experimental Mechanics* 39.3 (1999), pp. 217–226. DOI: <10.1007/BF02323555>. URL: <https://doi.org/10.1007/BF02323555>.

[24] Gerhard Venter and Melody Neaves. "SUN-DIC: A Python-based open-source software tool for Digital Image Correlation". In: *Advances in Engineering Software* 211 (2025). Preprint available at SSRN: 10.2139/ssrn.5333350, p. 104043. DOI: <10.1016/j.advengsoft.2025.104043>.

[25] G. Besnard, F. Hild, and S. Roux. ""Finite-Element" Displacement Fields Analysis from Digital Images: Application to Portevin–Le Châtelier Bands". In: *Experimental Mechanics* 46.6 (2006), pp. 789–803. DOI: <10.1007/s11340-006-9824-8>.

[26] J. Neggers et al. "Time-resolved integrated digital image correlation". In: *International Journal for Numerical Methods in Engineering* 103.3 (2015), pp. 157–182. DOI: <10.1002/nme.4882>.

[27] Rogério Lopes et al. "Coach crashworthiness and failure analysis during a frontal impact". In: *Engineering Failure Analysis* 151 (2023), pp. 107–118. DOI: <10.1016/j.engfailanal.2023.107118>. URL: <https://www.sciencedirect.com/science/article/pii/S1350630723003230>.

[28] Michael A. Sutton, Jean-José Orteu, and Hubert Schreier. *Image Correlation for Shape, Motion and Deformation Measurements: Basic Concepts, Theory and Applications*. New York, NY: Springer New York, 2009. ISBN: 978-0-387-78746-6. DOI: <10.1007/978-0-387-78747-3>.

[29] César A. Sciammarella. *Mecânica Experimental dos Sólidos*. Brochura, 460-476 páginas (varia conforme edição). LTC, 2017. ISBN: 9788521632665.

[30] V. Tiwari, M. A. Sutton, and S. R. McNeill. "Assessment of High Speed Imaging Systems for 2D and 3D Deformation Measurements: Methodology Development and Validation". In: *Experimental Mechanics* 47.5 (2007), pp. 561–579. DOI: <10.1007/s11340-006-9011-y>. URL: <https://doi.org/10.1007/s11340-006-9011-y>.

[31] Thorsten Siebert. "High-speed digital image correlation: error estimations and applications". In: *Optical Engineering* 46.5 (2007), p. 051004. DOI: <10.1117/1.2741217>. URL: <https://doi.org/10.1117/1.2741217>.

[32] Kamil Pazur, Paweł Bogusz, and Wiesław Krasoń. "Utilizing High-Speed 3D DIC for Displacement and Strain Measurement of Rotating Components". In: *Materials* 18.17 (2025), p. 3974. DOI: <10.3390/ma18173974>. URL: <https://www.mdpi.com/1996-1944/18/17/3974>.

[33] Phillip Jannotti, Nicholas Lorenzo, and Chris Meredith. "Application of High-Speed Digital Image Correlation to Taylor Impact Testing". In: *Dynamic Behavior of Materials, Volume 1: Proceedings of the 2019 Annual Conference on Experimental and Applied Mechanics*. Ed. by L. E. Lamberson. Conference Proceedings of the Society for Experimental Mechanics Series. Springer International Publishing, 2020, pp. 189–195. ISBN: 978-3-030-30020-3. DOI: <10.1007/978-3-030-30021-0_33>.

[34] Q. Fang, Z. Li, and H. Zhao. "On the behaviour characterization of metallic cellular materials under impact loading". In: *Applied Mechanics Reviews* 63.3 (2010), p. 030803. DOI: <10.1115/1.4000852>.

[35] Madhu S. Kirugulige, Hareesh V. Tippur, and Thomas S. Denney. "Measurement of transient deformations using digital image correlation method and high-speed photography: Application to dynamic fracture". In: *Applied Optics* 46.22 (2007), pp. 5083–5096. DOI: <10.1364/AO.46.005083>.

[36] Qianbing Zhang and Jian Zhao. "Determination of mechanical properties and full-field strain measurements of rock material under dynamic loads". In: *International Journal of Rock Mechanics and Mining Sciences* 60 (2013), pp. 423–439. DOI: <10.1016/j.ijrmms.2013.01.005>.

[37] Chao Wang et al. "Correction of start-up time difference-induced measurement errors of a high-speed binocular stereovision system". In: *Optics and Lasers in Engineering* 126 (2020), p. 105861. DOI: <10.1016/j.optlaseng.2019.105861>.

[38] José Sáez-Landete et al. "New Validation Metric for Solid Mechanical Models". In: *SSRN Electronic Journal* (2024). Available at SSRN: <https://ssrn.com/abstract=4698577>. DOI: <10.2139/ssrn.4698577>.

[39] K. Spranghers et al. "Numerical simulation and experimental validation of the dynamic response of aluminum plates under free air explosions". In: *International Journal of Impact Engineering* 54 (2013), pp. 83–95. DOI: <10.1016/j.ijimpeng.2012.11.011>.

[40] Jude M. Oka et al. "Nuclear material container drop testing using finite element analysis with verification using digital image correlation". In: *Journal of Nuclear Materials* 454 (2014), pp. 82–89. DOI: <10.1016/j.jnucmat.2014.07.012>.

[41] Róbert Huňady et al. "Stiffness Estimation and Equivalence of Boundary Conditions in FEM Models". In: *Applied Sciences* 11.4 (2021), p. 1482. ISSN: 2076-3417. DOI: <10.3390/app11041482>. URL: <https://www.mdpi.com/2076-3417/11/4/1482>.

[42] S. Avril et al. "Overview of Identification Methods of Mechanical Parameters Based on Full-field Measurements". In: *Experimental Mechanics* 48.4 (2008), pp. 381–402. DOI: <10.1007/s11340-008-9148-y>.

[43] Bin Chen et al. "Finite Element Model Updating for Material Model Calibration: A Review and Guide to Practice". In: *Archives of Computational Methods in Engineering* 32.4 (2025), pp. 2035–2112. DOI: <10.1007/s11831-024-10200-9>.

[44] F. Pierron and M. Grédiac. "Towards Material Testing 2.0: A review of test design for identification of constitutive parameters from full-field measurements". In: *Strain* 57.4 (2021), pp. 217–241. DOI: <10.1111/str.12370>. URL: <https://onlinelibrary.wiley.com/doi/abs/10.1111/str.12370>.

[45] N Hedayati, R Madoliat, and R Hashemi. "Strain measurement and determining coefficient of plastic anisotropy using digital image correlation (DIC)". In: *Mechanics & Industry* 18.3 (2017), p. 311.

[46] Akira Kato. "Measurement of strain distribution in metals for tensile test using digital image correlation method and consideration of stress-strain relation". In: *Mechanical Engineering Journal* 3.6 (2016), pp. 16–00141.

[47] Claudio D Schwindt et al. "Forming limit curve determination of a DP-780 steel sheet". In: *Procedia Materials Science* 8 (2015), pp. 978–985.

[48] Paweł Bogusz. "Digital Image Correlation Analysis of Strain Fields in Fibre-Reinforced Polymer–Matrix Composite under±45° Off-Axis Tensile Testing". In: *Polymers* 15.13 (2023), p. 2846.

[49] Mohammad Kashfuddoja, RGR Prasath, and M Ramji. "Study on experimental characterization of carbon fiber reinforced polymer panel using digital image correlation: A sensitivity analysis". In: *Optics and Lasers in Engineering* 62 (2014), pp. 17–30.

[50] Claudia Louise von Boyneburgk et al. "Mechanical characterization and simulation of wood textile composites (WTC) supported by digital image correlation (DIC)". In: *Composites Part C: Open Access* 11 (2023), p. 100370.

[51] Feng Chen et al. "Exploring digital image correlation technique for the analysis of the tensile properties of all-cellulose composites". In: *Cellulose* 28.7 (2021), pp. 4165–4178.

[52] HB Zeng and P Bailly. "Experimental characterization of dynamic behaviour of gelatin-based material using DIC". In: *Polymer Testing* 63 (2017), pp. 298–306.

[53] Simon Jonsson and Jörgen Kajberg. "Evaluation of Crashworthiness Using High-Speed Imaging, 3D Digital Image Correlation, and Finite Element Analysis". In: *Metals* 13.11 (2023), p. 1834.

[54] Nathaniel W Gardner et al. "Digital image correlation data processing and analysis techniques to enhance test data assessment and improve structural simulations". In: *2018 AIAA/ASCE/AHS/ASC Structures, Structural Dynamics, and Materials Conference*. 2018, p. 1698.

[55] Justin Littell. "Large field digital image correlation used for full-scale aircraft crash testing: methods and results". In: *International Digital Imaging Correlation Society: Proceedings of the First Annual Conference, 2016*. Springer. 2017, pp. 235–239.

[56] Rims Janeliukstis and Xiao Chen. "Review of digital image correlation application to large-scale composite structure testing". In: *Composite Structures* 271 (2021), p. 114143.

[57] Davide Mastrodicasa et al. "3D-DIC full field experimental modal analysis of a demo airplane by using low-speed cameras and a reconstruction approach". In: *Mechanical Systems and Signal Processing* 227 (2025), p. 112387.

[58] Peyman Poozesh et al. "Multicamera measurement system to evaluate the dynamic response of utility-scale wind turbine blades". In: *Wind Energy* 23.7 (2020), pp. 1619–1639.

[59] Daniel R Guildenbecher et al. "3D optical diagnostics for explosively driven deformation and fragmentation". In: *International Journal of Impact Engineering* 162 (2022), p. 104142.

[60] Daniel Reagan, Alessandro Sabato, and Christopher Niezrecki. "Feasibility of using digital image correlation for unmanned aerial vehicle structural health monitoring of bridges". In: *Structural Health Monitoring* 17.5 (2018), pp. 1056–1072.

[61] Mohammed Abbas Mousa et al. "Application of digital image correlation in structural health monitoring of bridge infrastructures: A review". In: *Infrastructures* 6.12 (2021), p. 176.

[62] Jan Winkler and Chris Hendy. "Improved structural health monitoring of London's docklands light railway bridges using digital image correlation". In: *Structural Engineering International* 27.3 (2017), pp. 435–440.

[63] Marco Civera and Cecilia Surace. "Non-destructive techniques for the condition and structural health monitoring of wind turbines: A literature review of the last 20 years". In: *Sensors* 22.4 (2022), p. 1627.

[64] Rong Wu et al. "Health monitoring of wind turbine blades in operation using three-dimensional digital image correlation". In: *Mechanical Systems and Signal Processing* 130 (2019), pp. 470–483.

[65] Xiao Chen et al. "Fatigue testing of a 14.3 m composite blade embedded with artificial defects–damage growth and structural health monitoring". In: *Composites Part A: Applied Science and Manufacturing* 140 (2021), p. 106189.

[66] Mohammad Kashfuddoja and M Ramji. "Whole-field strain analysis and damage assessment of adhesively bonded patch repair of CFRP laminates using 3D-DIC and FEA". In: *Composites Part B: Engineering* 53 (2013), pp. 46–61.

[67] F Laurin et al. "Determination of the properties of composite materials thanks to digital image correlation measurements". In: *Procedia IUTAM* 4 (2012), pp. 106–115.

[68] Aatif Jamshed et al. "A novel enhanced digital image correlation framework for structural health monitoring of aircraft". In: *Measurement* (2025), p. 119264.

[69] F Yusof and PJ Withers. "Real-time acquisition of fatigue crack images for monitoring crack-tip stress intensity variations within fatigue cycles". In: *The Journal of Strain Analysis for Engineering Design* 44.2 (2009), pp. 149–158.

[70] Eric Breitbarth et al. "Evolution of dislocation patterns inside the plastic zone introduced by fatigue in an aged aluminium alloy AA2024-T3". In: *Materials Science and Engineering: A* 718 (2018), pp. 345–349.

[71] Calvin M Stewart and Eduardo Garcia. "Fatigue crack growth of a hot mix asphalt using digital image correlation". In: *International journal of fatigue* 120 (2019), pp. 254–266.

[72] Andreas Blug et al. "Application of high-performance DIC for a comprehensive evaluation of biaxial fatigue crack growth experiments". In: *Strain* 59.6 (2023), e12455.

[73] De Qiang Wang et al. "Crack tip strain evolution and crack closure during overload of a growing fatigue crack". In: *Frattura ed Integrità Strutturale* 11.41 (2017), pp. 143–148.

[74] Marcin Malesa et al. "Non-destructive testing of industrial structures with the use of multi-camera Digital Image Correlation method". In: *Engineering Failure Analysis* 69 (2016), pp. 122–134.

[75] Ashim Khadka et al. "Strain monitoring of wind turbines using a semi-autonomous drone". In: *Wind Engineering* 46.1 (2022), pp. 296–307.

[76] F Seguel and V Meruane. "Damage assessment in a sandwich panel based on full-field vibration measurements". In: *Journal of Sound and Vibration* 417 (2018), pp. 1–18.

[77] Guangyong Sun et al. "Vibration-based damage identification in composite plates using 3D-DIC and wavelet analysis". In: *Mechanical Systems and Signal Processing* 173 (2022), p. 108890.

[78] Dixie M Hisley, James C Gurganus, and Andrew W Drysdale. "Experimental methodology using digital image correlation to assess ballistic helmet blunt trauma". In: (2011).

[79] Shen Zhouyu et al. "Research on transient response of pistol bullet impact on bulletproof helmet based on multiscale method". In: *Journal of Reinforced Plastics and Composites* (2024), p. 07316844251331998.

[80] Huicheng Wang et al. "Dynamic response of ballistic plate based on mirror image 3D-DIC technique". In: *Mechanics of Time-Dependent Materials* 29.3 (2025), pp. 1–19.

[81] YK Wen et al. "Analysis of dynamic back face deformation of a body armor impact by a rifle bullet using 3D-DIC". In: *Journal of Physics: Conference Series*. Vol. 1507. 3. IOP Publishing. 2020, p. 032051.

[82] D Iqbal and V Tiwari. "Investigations on the influence of projectile shape on the transient and post impact response of thin sheet structures". In: *Thin-Walled Structures* 145 (2019), p. 106402.

[83] YH Cheng et al. "Ballistic resistance of high-strength armor steel against ogive-nosed projectile impact". In: *Thin-Walled Structures* 183 (2023), p. 110350.

[84] Shujian Yao et al. "Experimental and numerical investigation on the dynamic response of steel chamber under internal blast". In: *Engineering Structures* 168 (2018), pp. 877–888.

[85] Clive R. Siviour and Jennifer L. Jordan. "High Strain Rate Mechanics of Polymers: A Review". In: *Journal of Dynamic Behavior of Materials* 2.1 (2016), pp. 15–32. DOI: <10.1007/s40870-016-0052-8>.

[86] Mark Jonathan Lidgett. "Multi-Scale Modelling of Polymer Composite Materials at High Rates of Strain". PhD Thesis. University of Nottingham, Aug. 2012.

[87] P. Reithofer et al. "Material Models for Thermoplastics in LS-DYNA® from Deformation to Failure". In: *15th International LS-DYNA Users Conference*. Composites track. United States: LSTC, June 2018.

[88] Stefan Kolling et al. "SAMP-1: A Semi-Analytical Model for the Simulation of Polymers". In: *LS-DYNA Anwenderforum*. Conference paper on constitutive modeling of polymers using SAMP-1. Bamberg, Germany: DYNAmore GmbH, 2005.

[89] X. Xiao. "Dynamic tensile testing of plastic materials". In: *Polymer Testing* 27 (2008), pp. 164–178. DOI: <10.1016/j.polymertesting.2007.09.010>. URL: <https://doi.org/10.1016/j.polymertesting.2007.09.010>.

[90] Shengbo Ling, Zhen Wu, and Jie Mei. "Comparison and review of classical and machine learning-based constitutive models for polymers used in aeronautical thermoplastic composites". In: *Reviews on Advanced Materials Science* 62 (2023), p. 20230107. DOI: <10.1515/rams-2023-0107>. URL: <https://doi.org/10.1515/rams-2023-0107>.

[91] C. J. G. Plummer, Ph. Béguelin, and H.-H. Kausch. "The Temperature and Strain-Rate Dependence of Mechanical Properties in Polyoxymethylene". In: *Polymer Engineering & Science* 35.16 (1995), pp. 1300–1312. DOI: <10.1002/pen.760351606>.

[92] Reema H. Alasfar et al. "A Review on the Modeling of the Elastic Modulus and Yield Stress of Polymers and Polymer Nanocomposites: Effect of Temperature, Loading Rate and Porosity". In: *Polymers* 14.3 (2022), p. 360. DOI: <10.3390/polym14030360>.

[93] H. Zhu, H. Ou, and A. Popov. "A new phenomenological constitutive model for thermoplastics". In: *Mechanics of Materials* 157 (2021), p. 103817. DOI: <10.1016/j.mechmat.2021.103817>. URL: <https://doi.org/10.1016/j.mechmat.2021.103817>.

[94] ANSYS, Inc. *ANSYS LS-DYNA® Theory Manual R16*. R16@e545952c7 (03/21/25), disponível em <https://lsdyna.ansys.com/wp-content/uploads/2025/04/LS-DYNA_Manual_Theory_R16.pdf>. ANSYS, Inc. Canonsburg, PA, USA, 2025.

[95] Henri P. Gavin. *Numerical Integration in Structural Dynamics*. Course Notes. Duke University, 2020.

[96] Hamid Naghibi Beidokhti et al. "A comparison between dynamic implicit and explicit finite element simulations of the native knee joint". In: *Medical Engineering & Physics* 38.10 (2016), pp. 1123–1130. DOI: <10.1016/j.medengphy.2016.06.001>.

[97] Alexandre Luis Marangoni and Ernesto Massaroppi Júnior. "Cowper-Symonds parameters estimation for ABS material using design of experiments with finite element simulation". In: *Polímeros: Ciência e Tecnologia* 27.3 (2017), pp. 220–224. DOI: <10.1590/0104-1428.04016>. URL: <https://doi.org/10.1590/0104-1428.04016>.

[98] Yuxiang Zhang et al. "A Novel Phenomenological Constitutive Model for Semi-Crystalline Polymers Across a Wide Strain-Rate Range". In: *Polymers* 17.6 (2025), p. 762. DOI: <10.3390/polym17060762>. URL: <https://www.mdpi.com/2073-4360/17/6/762>.

[99] Kebin Zhang et al. "Compressive Properties and Constitutive Model of Semicrystalline Polyethylene". In: *Polymers* 13.17 (2021), p. 2895. DOI: <10.3390/polym13172895>.

[100] William D. Callister and David G. Rethwisch. *Materials Science and Engineering: An Introduction*. 9th ed. Hoboken, NJ, USA: John Wiley & Sons, 2014.

[101] S. F. Edwards and T. Vilgis. "The Effect of Entanglements in Rubber Elasticity". In: *Polymer* 27.4 (1986), pp. 483–492.

[102] R. N. Haward and G. Thackray. "The Use of a Mathematical Model to Describe Isothermal Stress–Strain Curves in Glassy Thermoplastics". In: *Proceedings of the Royal Society of London. Series A, Mathematical and Physical Sciences* 302.1471 (1968), pp. 453–472.

[103] Mary C. Boyce, David M. Parks, and Ali S. Argon. "Large inelastic deformation of glassy polymers. Part I: Rate dependent constitutive model". In: *Mechanics of Materials* 7.1 (1988), pp. 15–33.

[104] G. R. Johnson and W. H. Cook. "A Constitutive Model and Data for Metals Subjected to Large Strains, High Strain Rates and High Temperatures". In: *Engineering Fracture Mechanics* 21 (1983), pp. 541–548.

[105] D. Garcia-Gonzalez et al. "Mechanical Impact Behavior of Polyether-Ether-Ketone (PEEK)". In: *Composite Structures* 124 (2015), pp. 88–99.

[106] P. Perzyna. "Fundamental Problems in Viscoplasticity". In: *Advances in Applied Mechanics*. Ed. by C.-S. Yih. Vol. 9. New York, NY, USA: Academic Press, 1966, pp. 243–377. DOI: <10.1016/S0065-2156(08)70009-7>.

[107] Andrej Škrlec et al. "Estimating the Cowper–Symonds Parameters for High-Strength Steel Using DIC Combined with Integral Measures of Deviation". In: *Metals* 14.9 (2024), p. 992. DOI: <10.3390/met14090992>. URL: <https://www.mdpi.com/2075-4701/14/9/992>.

[108] Sven Robert Raisch and Bernhard Möginger. "High rate tensile tests – Measuring equipment and evaluation". In: *Polymer Testing* 29.3 (2010), pp. 265–272. DOI: <10.1016/j.polymertesting.2009.11.010>.

[109] Norman Jones. *Structural Impact*. 2nd ed. Cambridge, UK: Cambridge University Press, 2012. ISBN: 978-1-107-01096-3. DOI: <10.1017/CBO9780511820625>.

[110] Plastore.it. *Delrin® 100 NC010 – POM Homopolymer Property Data Sheet*. 2018. URL: <https://plastore.it/cgi2018/file818/19_pom%5C%20delrin%5C%20100.pdf> (visited on 01/13/2026).

[111] Michael F. Ashby. *Materials Selection in Mechanical Design*. 4th ed. Oxford: Butterworth-Heinemann, 2011.

[112] Q. B. Zhang and J. Zhao. "Determination of mechanical properties and full-field strain measurements of rock material under dynamic loads". In: *International Journal of Rock Mechanics and Mining Sciences* 60 (2014), pp. 423–439. DOI: <10.1016/j.ijrmms.2013.11.004>.

[113] *Guide for Verification and Validation in Computational Solid Mechanics*. New York: American Society of Mechanical Engineers, 2016.

[114] M.A. Sutton, J.J. Orteu, and H. Schreier. *Image Correlation for Shape, Motion and Deformation Measurements*. Springer, 2009.

[115] H. Schreier, J.J. Orteu, and M.A. Sutton. "Digital image correlation for the characterization of large deformation and strain". In: *Experimental Mechanics* 49.1 (2009), pp. 1–14.

[116] Fabrice Pierron and Michel Grédiac. "Towards Material Testing 2.0: A review of test design for identification of constitutive parameters from full-field measurements". In: *Strain* 57.4 (2021), e12370. DOI: <10.1111/str.12370>. URL: <https://doi.org/10.1111/str.12370>.

[117] Jude M. Oka et al. "Nuclear material container drop testing using finite element analysis with verification using Digital Image Correlation". In: *Nuclear Engineering and Design* 421 (2024), p. 113057. DOI: <10.1016/j.nucengdes.2024.113057>.

[118] Rogério Lopes et al. "Coach crashworthiness and failure analysis during a frontal impact". In: *International Journal of Crashworthiness* 19.4 (2014), pp. 394–405. DOI: <10.1080/13588265.2014.912312>.

[119] Suri Bala. *Contact Modeling in LS-DYNA*. Tech. rep. Technical Report. Parts 1–4. Livermore Software Technology Corporation, 2001.

[120] P. O. Cronemberger et al. "Theoretical and Experimental Study of the Interior Ballistics of a Rifle 7.62". In: *Engenharia Térmica (Thermal Engineering)* 13.2 (Dec. 2014), pp. 20–27.